Challenging the hypothesis of rapid true polar wander in the Neoproterozoic: A multi-disciplinary study of the complex paleomagnetic record from Yangjiaping, South China

Justin A. D. Tonti-Filippini

München 2023

Challenging the hypothesis of rapid true polar wander in the Neoproterozoic: A multi-disciplinary study of the complex paleomagnetic record from Yangjiaping, South China

Dissertation zur Erlangung des Doktorgrades
an der Fakultät für Geowissenschaften
der Ludwig-Maximilians-Universität München

Vorgelegt von
Justin A. D. Tonti-Filippini

München, 30.03.2023

Erstgutachter: Prof. Dr. Stuart Gilder
Zweitgutachter: Prof. Urs Schaltegger

Tag der mündlichen Prüfung: 23.05.2023

Summary

This thesis investigates complex paleomagnetic directions in Neoproterozoic rocks, 820 – 800 million years old (Ma). The paleomagnetic record during this time exhibits large and rapid directional swings, which previous work has used to support large (55 to 90°) rotations of Earth's lithosphere and mantle with respect to the spin axis, known as rapid true polar wander. Dramatic changes in the global environment are observed simultaneously. This thesis tests whether such extraordinary variations reflect the true magnetic fidelity or if another explanation is more plausible. Three chapters in this thesis are based on samples collected from the Laoshanya Formation in Yangjiaping (Hunan province, China).

The first chapter details a novel technique that unmixes paleomagnetic data based on inverse modelling and vector analyses. Stepwise thermal demagnetisation of 1188 specimens isolates three magnetisation components whose directional changes are not temporally progressive with the stratigraphy but conflated throughout the 85 metre section. Two of the components unblock over similar temperature ranges (600 – 680 °C) which prohibits their accurate resolution with conventional paleomagnetic line-fitting techniques. Using this new method, I show that rapid directional changes in the Laoshanya Formation are better explained by variable mixing (overlapping spectra) of the magnetisation components, rather than geomagnetic field variability or plate motion.

The results of the paleomagnetic study are detailed in the second chapter, which includes high-precision U-Pb geochronology that brackets the age of the Laoshanya Formation between 809 and 804 Ma. It is shown that the three magnetisation components reside in distinct generations of hematite. A primary (dual-polarity) magnetisation was locked-in during deposition, while a secondary, single-polarity, component was acquired in the late Ordovician (ca. 440 Ma) during a low-grade tectono-thermal event (< 260°C). A third component is interpreted to be an overprint commonly found in South China that was locked-in during the Cretaceous normal superchron. Regional comparisons suggest that the Ordovician component may be widespread, complicating paleomagnetic records in pre-Ordovician strata. These findings suggest that the sudden directional changes observed in Neoproterozoic rocks from South China are artefacts of remagnetisation. The primary magnetisation places South China at high latitudes from 809 to 804 Ma.

The third chapter presents a geochemical and petrophysical examination of the Laoshanya Formation to elucidate mechanisms responsible for the acquisition of the secondary magnetisations. Rocks carrying the primary magnetisation are enriched in coarse quartz and feldspar grains, and relatively impoverished in major and trace elements. Rocks remagnetised in the Ordovician are richer in phyllosilicates (particularly muscovite) and alkali concentrations, while the rocks dominated by the Cretaceous overprint component have higher concentrations of iron, rare-earth elements and heavy metals. There are only weak correlations with permeability and porosity, suggesting that remagnetisation was controlled by thermal alteration of existing clay minerals and not enrichment by external fluids. Our findings can help identify secondary from original magnetisations elsewhere and call for careful consideration of magnetisations spanning different lithologies, particularly those with interbedded mudstones and sandstones.

Contents

Acknowledgements

This work was enabled by a large number of people to whom I am greatly indebted. I'd like to thank:

- First of all, Stuart Gilder, for his wisdom, good spirit and guidance over the past four years. I am extremely lucky to have him as a mentor.
- Boris Robert, for enabling this project and believing in me from the beginning, and for tolerating my outlandish hypotheses and lengthy discussions.
- My other collaborators, Élodie Muller, Fabian Dellefant, André Paul, Michael Wack, Jun Meng, Xixi Zhao, Urs Schaltegger, Daniel Weller and Vincent Busigny, for their hard work and insightful contributions.
- All of those who assisted me in various laboratories, especially Leon Kaub, Günter Hesberg, Petter Silkoset, Claudia Trepmann, Uwe Kirscher, Erwin Appel, Michael Volk and Aurélia Crinière.
- All the staff and my colleagues at LMU Munich, the University of Geneva and UNIS Svalbard, who helped me pursue my research in good faith, especially Ira Venus-Sircar, Florian Lhuillier, Maria Ovtcharova and Maria Jensen.
- Trond Torsvik and the team at CEED, for generously hosting me after my masters degree and granting me invaluable time to find a doctoral position.
- My family in Australia, Mum, Claire, Lucianne, John, Bundy, James, Harry and Lily, for their love and encouragement, and for all the Tim Tams.
- Sandra Hahn, for all the real and virtual coffee.
- Alex and Sarah, for the fancy lockdown dinners, film nights and funk records.
- Humphrey the husky, for taking me outside and into nature, whatever the weather.
- The entire Onarheim family, for adopting a stray Australian trapped on the other side of the world and making him feel like one of their own. I am especially grateful to Ingvild and Lars, and Annemor and Leif, for their continued support, countless meals and bottles of wine, and for providing the space and time (and hardware) necessary for me to complete this work.
- Most of all, Margrethe, for her unconditional endorsement and endurance of my moods, and for following me around the world. I will be eternally grateful.

I knock at the stone's front door.
"It's only me, let me come in.
I don't seek refuge for eternity.
I'm not unhappy.
I'm not homeless.
My world is worth returning to.
I'll enter and exit empty-handed.
And my proof I was there
will be only words,
which no one will believe."

Wislawa Szymborska
(from *Conversation with a Stone*)

Introduction

The paleomagnetic record for South China in the Neoproterozoic (1000 – 720 Ma) shows large and rapid directional changes, which have been suggested to reflect significant upheavals in Earth's tectonic and climatic systems around the same time. Resolving the discordant directions found in South China is extremely important for our understanding of Earth's evolution, geodynamics, and drivers of climate change on geological timescales. This problem must be resolved with paleomagnetic data, as they provide our only opportunity to accurately reconstruct Earth's surface and substructure in deep time. Here I briefly introduce several principles relevant to the following chapters, which contain a detailed and multi-disciplinary investigation of the discordant directions.

Paleomagnetism of sedimentary rocks

Earth has a magnetic field which can be approximated by a large dipole centred at its core (Fig. 1a). The field is generated by convecting and conducting metallic fluid in Earth's outer core, and is aligned approximately with the geographic (i.e. rotational) poles over geological timescales – the geocentric axial dipole (GAD) hypothesis. A GAD field produces a predictable pattern of directional variations over Earth's surface, which vary from steep 'down' at the north (geographic) pole to steep 'up' at the south pole, with a horizontal field at the equator. Detailed observations of this field have been made since the 16th century, as sailors used the field for ocean navigation. To reconstruct the field prior to direct observations, we turn to archives in the geologic record, as some rocks can preserve a record of the field over hundreds of millions of years.

When sediment is deposited on Earth's surface, e.g. on the seafloor, magnetic grains in the sediment statistically align their moments with the ambient (geomagnetic) field via torque during deposition (Fig. 1b). These magnetic minerals will form a detrital remanent magnetisation (DRM) which is locked-in during diagenesis (i.e. conversion to rock) and retain a memory of the field direction from the time of deposition. Oriented samples from sedimentary rocks can then be used to recover the direction of past geomagnetic field, and infer the paleolatitude of the location where the rocks were formed, as the vertical direction (i.e. inclination) of the field varies reliably with distance from the equator.

To recover ancient directions from sedimentary rocks, paleomagnetists typically collect multiple samples from a given sedimentary unit (or 'site') and subject the samples to stepwise demagnetisation, using heat (thermal demagnetisation) and/or alternating magnetic

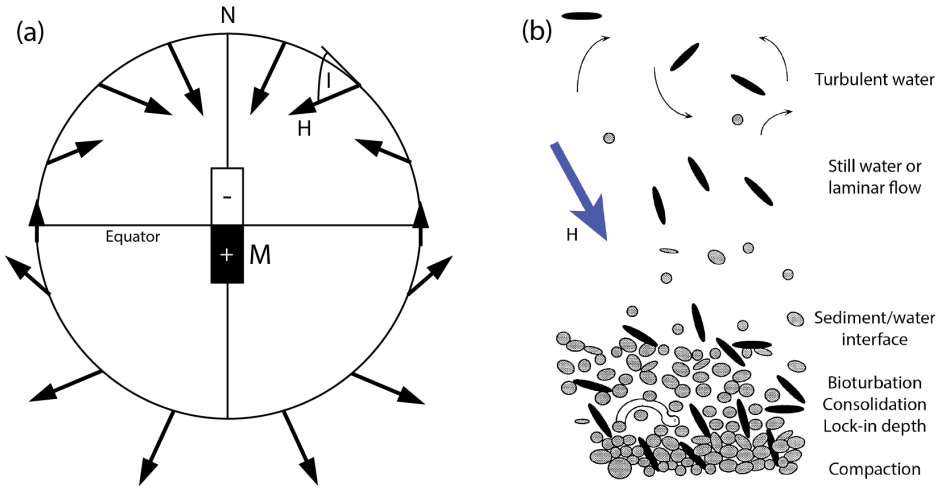

Figure 1: (a) Geocentric axial dipole model, modified from Butler (1992). The magnetic dipole M is aligned with geographic poles (N = north). H is the local magnetic field. I is the magnetic inclination (from horizontal). (b) Schematic view of the alignment of magnetic grains (black) in a water column with the ambient field (H), after Tauxe (1993).

fields (AF demagnetisation). After each demagnetisation step, samples are measured for their remanent magnetisation, which yields a set of remanence vectors (Fig. 2). The magnitudes of the vectors decrease as a sample's magnetisation is progressively unblocked (due to increasing temperatures or AF strength), according to Néel (1949) theory. A best-fitting line through resultant vectors trending to the origin (e.g. steps 3-6 in Fig. 2d) is used to determine the direction of a sample's characteristic remanent magnetisation (ChRM), a process known as principal component analysis (PCA).

The mean ChRM direction for a site can be converted to an apparent pole or virtual geographic pole (VGP) through the law of cosines, and used to infer the location of the paleomagnetic pole relative to a fixed tectonic plate (Figs. 3a and b). This 'paleopole' should be consistent across rocks formed at the same time in the same location. Through the assumption of a GAD field, a paleopole can be translated to the present north or south geographic pole and used to reconstruct the paleolatitude of a site (or tectonic plate).

Apparent and true polar wander

As tectonic plates can move or rotate about Earth's surface (Fig. 3c), paleomagnetic measurements from sequences of rocks, spanning at least several millions of years, will observe 'apparent polar wander', as the paleopole appears to move relative to a fixed tectonic plate (Fig. 3e). In reality, apparent polar wander is an effect of continental drift, or motion of the tectonic plate on which the rocks formed (Fig. 3d). A sequence of paleopoles (VGPs) can be displayed on an apparent polar wander path (APWP), which can be used to visualise a plate's relative motion over time (Fig. 3e).

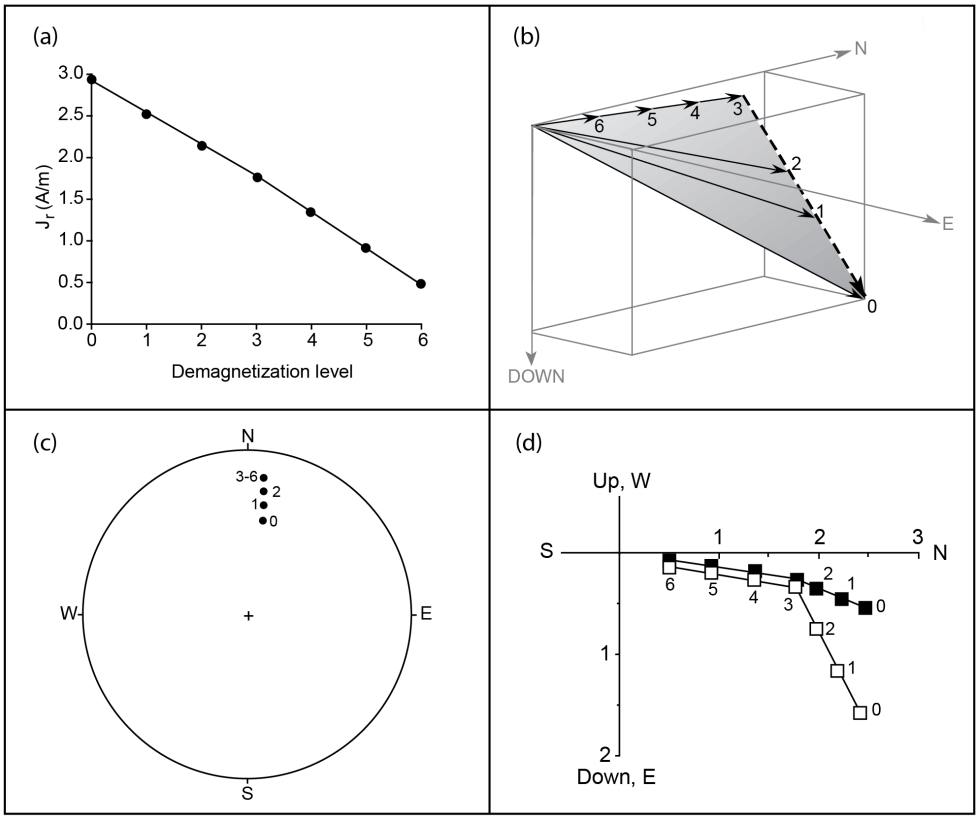

Figure 2: Stepwise demagnetisation vectors, modified from Butler (1992). A sample's remanent magnetisation (J_r) is progressively destroyed during demagnetisation steps 0-6 (a), resulting in a sequence of 3D vectors (b). The vectors can be displayed on a stereonet (c), or a Zijderveld (1967) diagram (d) which projects the vectors onto two orthogonal planes and enables visual fitting of linear components. In this case, the characteristic remanent magnetisation (ChRM) direction would be obtained by fitting a straight line through points 3-6. (A secondary magnetisation component could also be obtained with a line through steps 0-3.)

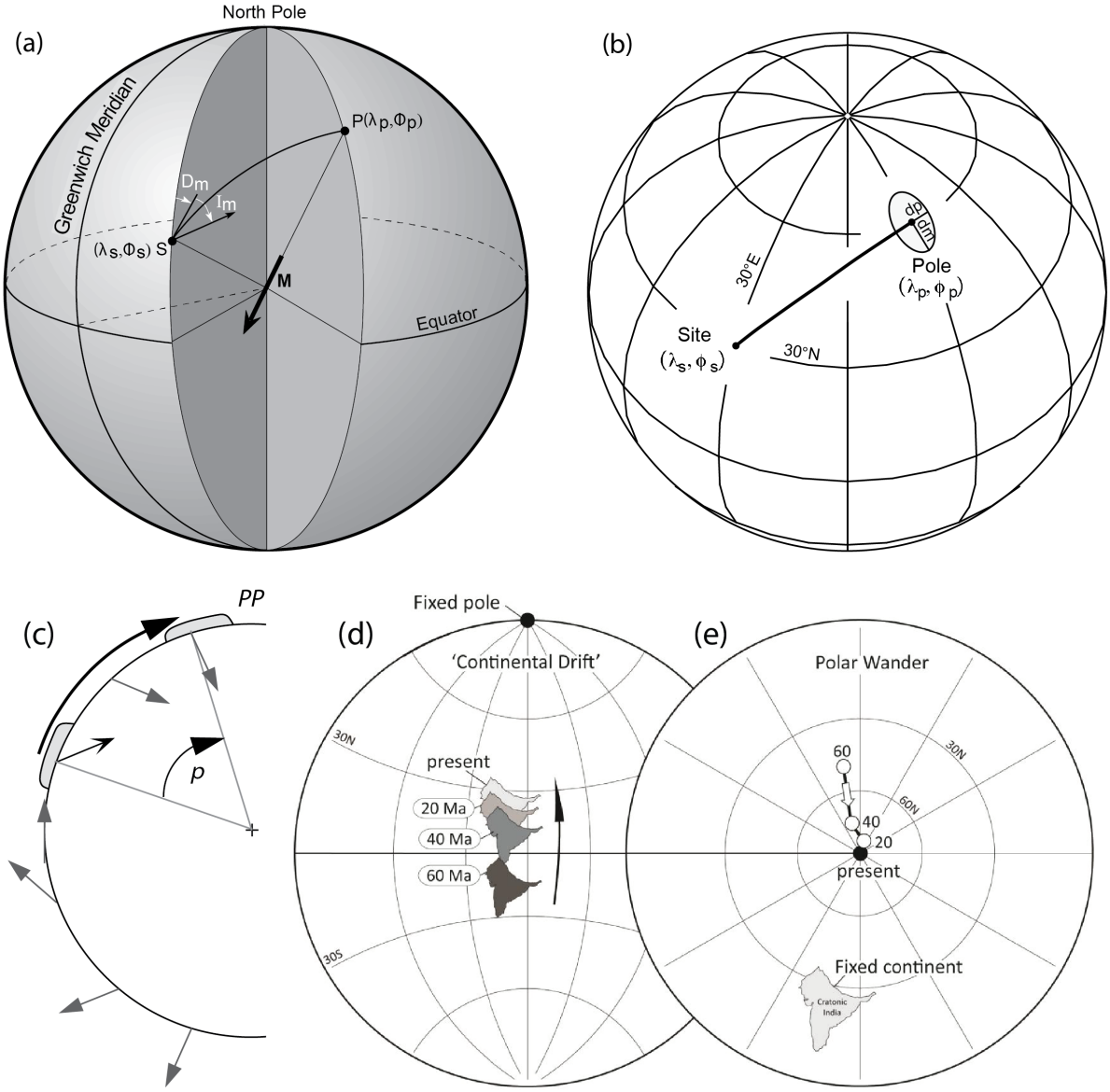

Figure 3: (a) Translation of site (S) mean declination and inclination (Dm and Im) to paleopole (P). M is the ancient dipole moment. Site and pole coordinates are given by latitude (ϕ) and longitude (λ). (b) Pole derived from site mean direction with 95% confidence ellipse represented by dp/dm. (c) Changes to expected paleomagnetic field directions during northward tectonic plate motion (p), where PP = paleopole. Figures modified from Butler (1992). Examples of (d) continental drift, relative to a fixed pole, and (e) apparent polar wander, relative to a fixed plate, for the Indian craton for the 0 – 60 Ma, modified from Torsvik et al. (2012).

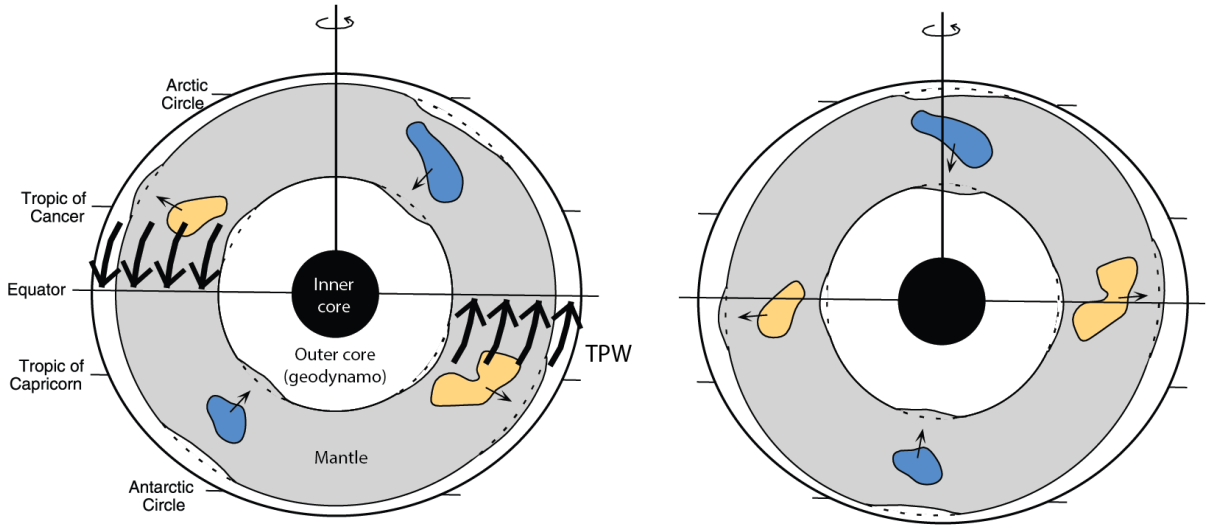

Figure 4: Simplified true polar wander (TPW) after Evans (2002). Blue shapes indicate cold, dense material (e.g. subducted slabs). Orange shapes indicate hot, buoyant material (e.g. mantle plumes).

While tectonic plates can move independently, the entire tectonic system (i.e. Earth's crust and mantle) is also mobile with respect to the core (and spin axis). Net rotation of the tectonic system is referred to as 'true polar wander' (TPW) and occurs due to gradual changes in Earth's moment of inertia and conservation of angular momentum (Fig. 4). Mantle convection and the subduction of tectonic plates causes heterogeneous mass distributions which are effectively balanced out by TPW, as Earth tries to align its maximum moment of inertia with the rotational axis. Apparent polar wander is therefore the combined effect of individual plate motion and TPW.

Plate motion and TPW both occur at similar rates, ca. 1 ° per million years (Myr), so they cannot be separated by observations at a single location. However, correlation of APWPs from multiple tectonic plates can be used to estimate TPW motions, as TPW will be common to all continents. A globally correlated APWP for 0 – 320 Ma (Torsvik et al., 2012) allows for precise estimates of TPW rates and paleogeographic reconstructions back to the time of Pangaea, the most recent supercontinent, when the majority of Earth's continents were clustered together. But the geological record becomes more sparse further back in time, particularly beyond the age of the oldest seafloor, ca. 280 Ma, so reconstructing TPW and plate motion becomes increasingly difficult with age.

Extending APWPs into the Precambrian

Primary paleomagnetic records older than the amalgamation of Pangaea are sporadic, complicating the compilation of continuous and global APWPs beyond 320 Ma. The problem

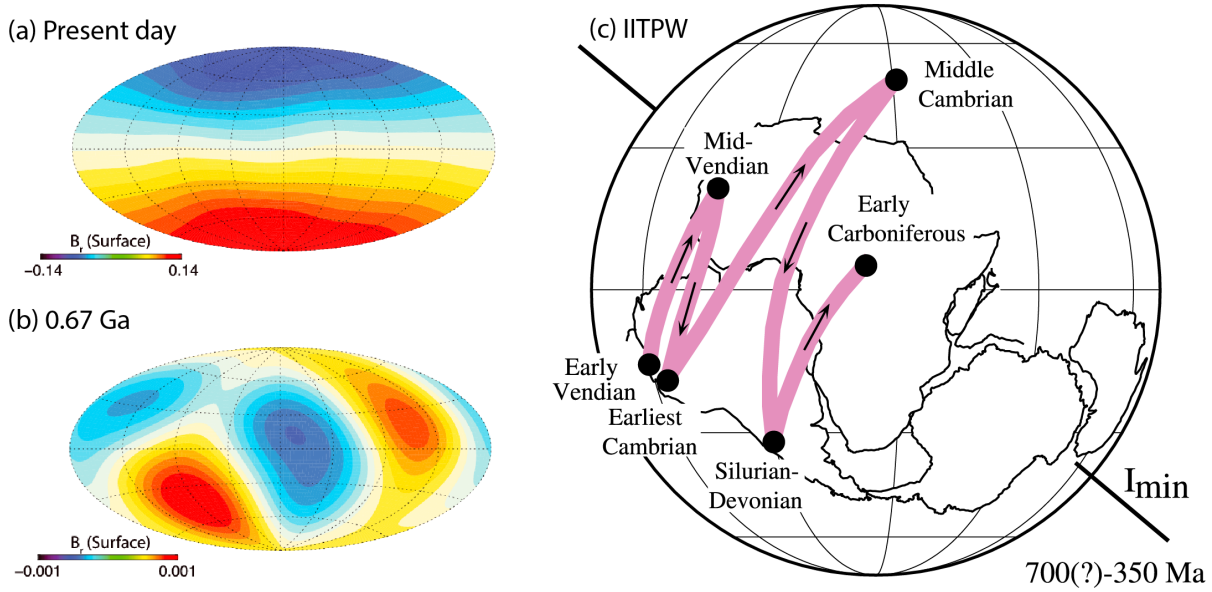

Figure 5: Examples of (a) present day (dipolar) field geometry and (b) expected weak (non-dipolar) field geometry prior to inner-core nucleation at 670 Ma, modified from Driscoll (2016). (c) Apparent polar wander due to oscillatory TPW (or IITPW) for the Vendian (Cryogenian/Ediacaran) to Carboniferous, as illustrated by Evans (2002), which occurs about a common, long-lived, minimum-inertial axis (I_{min}).

is especially challenging for the Precambrian (> 541 Ma), when Earth's history becomes even more enigmatic. The youngest era of the Precambrian, the Neoproterozoic (1000 – 541 Ma), appears to have been a particularly tumultuous time in Earth's history. The Neoproterozoic is currently divided into the Tonian (1000 – 720 Ma), Cryogenian (720 – 635 Ma) and Ediacaran (635 – 541 Ma) periods (Cohen et al., 2022). The Tonian saw the end of long-lived environmental stagnation prior to ca. 800 Ma (Mukherjee et al., 2018), perhaps due to the break-up of an older supercontinent (known as Rodinia), as well as several dramatic global environmental changes. The geological record of the Cryogenian contains evidence for massive global glaciations, i.e. the Snowball Earth hypothesis (Kirschvink, 1992), while the Ediacaran contains the earliest evidence of widespread multi-cellular life, the Ediacaran biota (Morris, 1985), and culminated in the Cambrian explosion and an increase in atmospheric oxygen to present-day levels ca. 542 Ma (Marshall, 2006).

The paleomagnetic record for the Neoproterozoic is also complex, and appears to show sudden directional changes and TPW rates much higher, i.e. up to 4 – 8 °/Myr (Fu et al., 2022), than rates estimated for past 320 Ma, < 1 °/Myr, or < 2 °/Myr between 320 and 540 Ma (Torsvik et al., 2012). Significant changes in mantle dynamics have been postulated to explain enhanced TPW in the Neoproterozoic (Fu et al., 2022). It's also possible that the geomagnetic field behaved differently in the Neoproterozoic, e.g. exhibiting a dominant non-dipolar component (Abrajevitch and Van der Voo, 2010), hyper-reversal frequency and/or ultra-low field intensity, perhaps due to nucleation of Earth's inner core (Fig. 5a).

Inertial interchange true polar wander (IITPW) events have also been proposed to explain rapid changes in paleodirections during the Cambrian (Kirschvink et al., 1997) and Neoproterozoic (Maloof et al., 2006). IITPW events describe large oscillating TPW motions (Fig. 5c), which are to be expected if Earth is dominated by mobile subduction zones, as hypothesized for supercontinent cycles in the Precambrian (Evans et al., 2016). Inertial interchange can occur if Earth's maximum (I_{max}) and intermediate (I_{int}) moments of inertia change places, causing rapid rotations up to 90° away from the spin axis around the minimum moment of inertia (I_{min}).

Secondary magnetisations

Further complicating Precambrian paleomagnetic records is the occurrence of secondary magnetisations, as primary depositional signals can be obscured by diagenetic and metamorphic overprinting. The effects of diagenesis are always important to consider in understanding the magnetic properties of sedimentary rocks (Roberts, 2015). With increasing age, a rock is more likely to have experienced tectonic stress and deformation at some point in its past. Chemical remagnetisation is a significant issue in paleomagnetism, and is intertwined with our understanding of the physical connections between tectonic events, magmatism, fluid flow and mineralisation. Temporal and physical proximity of chemical remagnetisations to orogenic activity is frequently observed and has led some to believe that orogenically-driven fluids play an important role in the formation of secondary magnetisations (Oliver, 1986). But chemical remanent magnetisations (CRMs) have been found in rocks with very low permeabilities and without evidence for fluid alteration , which require an alternative explanation (e.g. Katz et al., 1998).

In particular, the nature and timing of remanence acquisition in hematite-bearing sedimentary rocks (known as 'red beds') is a topic that has been debated since the dawn of paleomagnetism, and there is still no consensus on whether magnetisations in these rocks are primary or secondary (Kodama, 2012). This may be, in part, due to the vagueness of the term 'red bed', which can refer to a range of sedimentary rocks formed under vastly different conditions. Central to the red bed controversy is whether crystalline or specular hematite can precipitate or form authigenically (i.e. a CRM) at low-temperatures and a substantial time (i.e. millions of years) after deposition. Hematite in a sedimentary rock can crystallise through numerous pathways (see Cornell and Schwertmann, 2003) and will acquire a secondary magnetisation when particles grow into a size range that is paleomagnetically stable. The 'worst case scenario' for a sedimentary rock is when this process occurs over an extended period well after its formation (Kodama, 2012).

To determine the lock-in timing of magnetisation components, paleomagnetists commonly employ field tests, including conglomerate, fold and baked contact tests (Fig. 6). Randomly oriented magnetisations in conglomerate clasts indicate that the magnetisation of the parent beds has been stable since formation of the conglomerate. Convergence of paleomagnetic directions from different limbs of a fold, after correcting for tilt, indicates that the magnetisation is older than the folding event and therefore more likely to be primary.

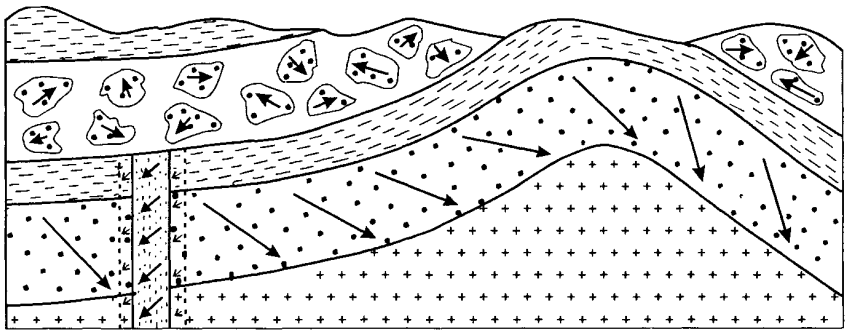

Figure 6: Schematic for conglomerate, fold, and baked contact tests for paleomagnetism, from Merrill and McElhinny (1983).

Directions in a baked zone around an intrusion that are consistent with the directions within the intrusion, but different to the surrounding country rock, indicate that the magnetisation of the intrusion has been stable since its formation. However, false positives can occur: for example, if a secondary magnetisation has formed a long time after deposition, but before folding, it will still pass a fold test despite not being primary.

There can also be interplay between primary and secondary magnetisation components during demagnetisation, which complicates the determination of directions when applying best-fitting line procedures. Magnetisation components can be defined by their unblocking spectra during demagnetisation, and multiple components will form distinguishable linear segments on a Zijderveld diagram if their unblocking spectra are distinct (Figs. 7a-b). However, unblocking spectra of multiple components can overlap significantly and produce a Zijderveld diagram that appears to decay to the origin, but gives a spurious direction that deviates from the 'true' directions of both end-members (Figs. 7c-d).

South China in the Neoproterozoic

The largest rapid TPW (or IITPW) motions observed on Earth since 1 Ba have been proposed to explain discordant paleodirections ca. 820 – 800 Ma, initially observed in sedimentary rocks from Svalbard (Maloof et al., 2006). Similarly large and rapid changes in paleodirections have been observed in South China and linked to the same IITPW events, which may have rotated Earth's lithosphere 55 – 90° (with respect to the spin axis) over 5 – 10 Myr (Fig. 8a). These events have been invoked to explain global environmental changes around the same time, known as the Bitter Springs Stage, as evidenced by severe fluctuations in the global carbon isotope record (Fig. 8b). Alternative explanations for the discordant directions include perturbations of the geomagnetic field, such as deviation from a predominantly dipolar field and/or a hyper-reversing field. Undiagnosed remagnetisations could also play a role, as many paleodirectional studies of South China in the Neoproterozoic were derived from hematite-bearing sandstones (red beds), which have

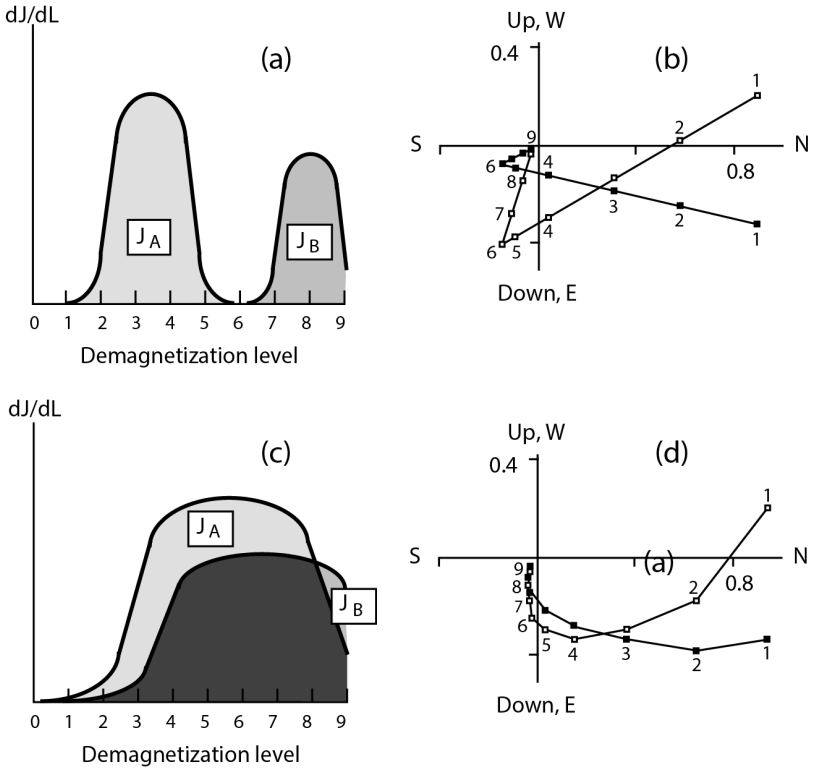

Figure 7: Unblocking spectra and resultant Zijderveld diagrams for hypothetical components J_A and J_B with no overlap (a-b) and significant overlap (c-d). Significant overlap between the unblocking spectra of primary and secondary components can complicate best-fitting line procedures and produce spurious paleomagnetic directions. Modified from Butler (1992).

complicated magnetisation histories.

To test these hypotheses, 1057 oriented samples were collected over 85 metres of Laoshanya Formation red beds in Yangjiaping (northwest Hunan, South China), which were previously dated to 809 ± 16 Ma (Yin et al., 2003). The samples were subjected to a range of paleomagnetic, rock magnetic, geochemical, mineralogical and petrophysical experiments. The intention was to determine if the magnetisations in the Laoshanya Formation are primary in nature and, if so, whether the directional changes are progressive in time, as would be expected for coherent TPW or plate motion. Failing either of these two criteria would require an alternative explanation, e.g. selective remagnetisation of the rocks or a non-dipolar/non-GAD field in the Neoproterozoic. Additional samples of interbedded tuffs within the section were also collected for geochronological experiments (U-Pb dating of zircons), to precisely constrain the age of the Laoshanya Formation and allow for direct comparison with contemporary formations.

Overview and contributions

Chapter 1 describes a novel technique which was developed to isolate primary and secondary magnetisation components. The method utilises vector calculus and inverse modelling to unmix stepwise demagnetisation data, and can be used to quantify absolute contributions of components with overlapping or superimposed unblocking spectra. I developed the idea for the method in conversation with Stuart Gilder (SG), as it appeared that the demagnetisation results from the Yangjiaping samples were a conflation of two or three superimposed signals, and not a true record of the paleomagnetic field. I developed the methodology and wrote the MATLAB scripts to unmix the (three-component) data from Yangjiaping. SG provided additional (two-component) data from an earlier study which helped to strengthen our methodology. I wrote the manuscript with significant input from SG. The paper was published by Geophysical Journal International in December 2022. Chapter 1 contains the authors' original version (prior to journal formatting and copy-editing).

Chapter 2 presents the paleomagnetic, rock magnetic, mineralogical and geochronology data obtained from Yangjiaping, as well as a detailed assessment of implications for the paleogeography of South China, the geomagnetic field and the rapid true polar wander hypothesis in the Neoproterozoic. I carried out paleomagnetic sampling in 2019 with SG, Boris Robert (BR), Élodie Muller (EM), Michael Wack and Xixi Zhao. I performed most of the paleomagnetic and rock magnetic experiments in Munich, with supervision from SG, as well as further experiments at paleomagnetic laboratories in Oslo and Tübingen. I also carried out scanning electron microscopy with Fabian Dellefant (FD) in Munich, and additional observations were made by EM in Paris. In 2021, samples of suspected tuffs in Yangjiaping were collected by Jun Meng. In 2022, I travelled to Geneva and performed U-Pb dating of the tuff samples with André Paul, under the supervision of Urs Schaltegger. I wrote the manuscript with significant input from BR and SG, and in consultation with the other collaborators. Chapter 2 has been submitted and undergone a first round of peer

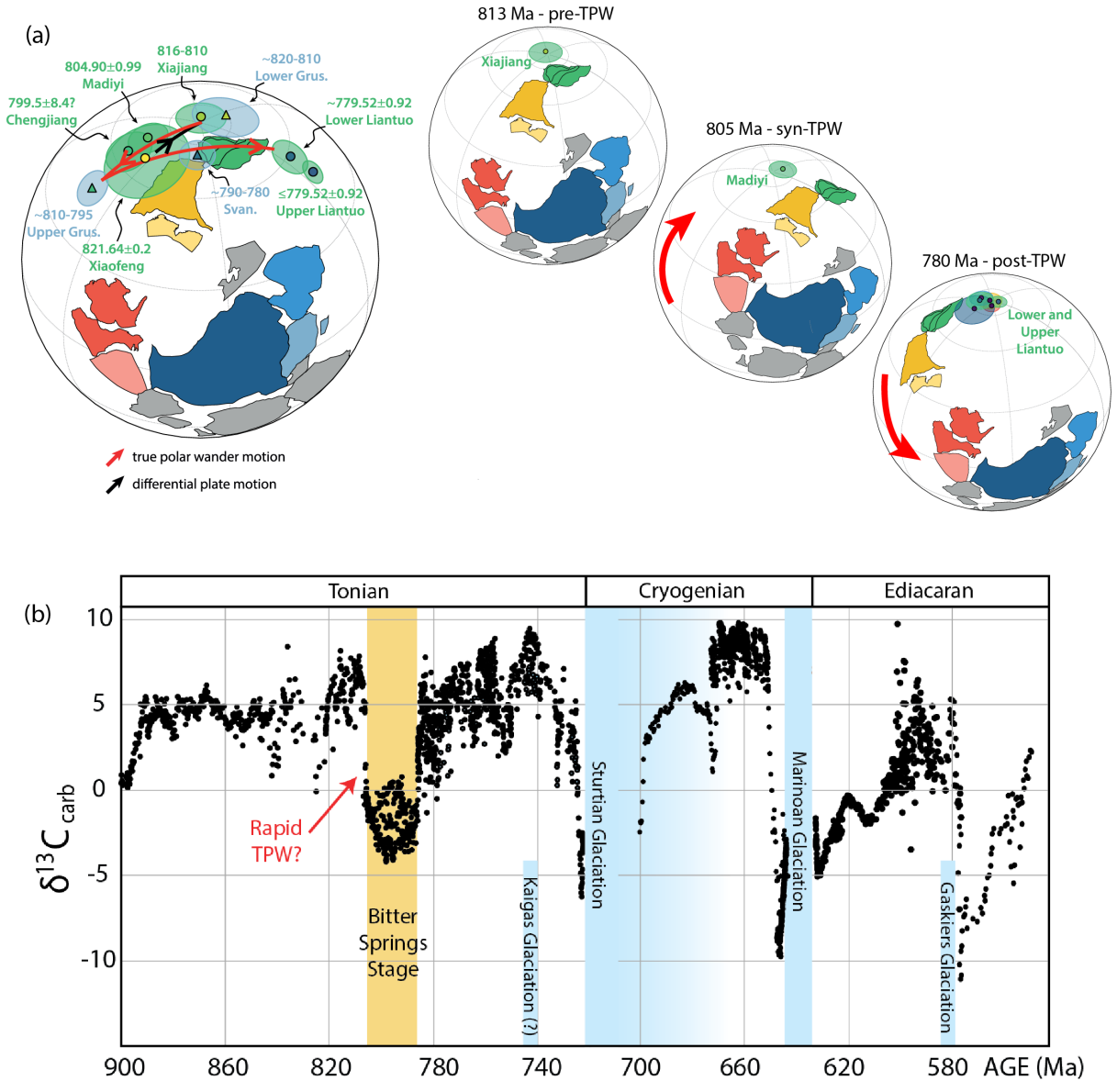

Figure 8: (a) Rapid TPW event postulated for 820 - 780 Ma, with paleogeographic reconstructions, modified from Park et al. (2021). Blue circles are paleomagnetic data from Svalbard (Maloof et al., 2006), green circles are various data from South China. (b) Composite global carbon isotope record for the Neoproterozoic, with major glaciations, modified from Swanson-Hysell et al. (2012).

review, and is now in a second round following revisions with the Journal of Geophysical Research: Solid Earth.

Chapter 3 diagnoses likely mechanisms for the formation of secondary magnetisations in Yangjiaping. To do this, I used the vector unmixing method from Chapter 1 to quantify component contributions in each specimen, and test for correlations between individual component magnitudes and various geochemical, petrophysical and mineralogical quantities (e.g. element concentrations, rock density, permeability and porosity). I carried out reflected and transmitted light microscopy with FD in Munich. EM performed geochemical and isotopic analyses in Paris, with input from Vincent Busigny. Daniel Weller performed the petrophysical experiments in Munich. I performed the vector unmixing analyses, and wrote the manuscript in consultation with the other collaborators. Chapter 3 is in preparation for submission to Geochemistry, Geophysics, Geosystems.

Chapter 1

Vector unmixing of multicomponent palaeomagnetic data

Abstract

Palaeomagnetic investigations often encounter multiple magnetisation components, where secondary processes have obscured, partially overprinted or completely replaced the original (primary) remanent magnetisation. Identification and separation of primary and secondary magnetisations are generally carried out with principal component analysis of stepwise demagnetisation data. However, rocks may contain multiple generations of magnetic minerals with overlapping unblocking ranges that complicate the discrimination of components when applying best-fit line procedures. Developing a method to differentiate and quantify contributions of overlapping magnetic components using directional data is therefore highly desirable. This chapter presents a method to unmix stepwise demagnetisation data using an inverse modelling approach. We show that the method is capable of accurately resolving two or three magnetic components with overlapping or superimposed unblocking spectra as well as quantifying absolute component contributions. The method depends on accurate identification and selection of end-member components prior to analysis; in doing so, the method can help palaeomagnetists understand how magnetisation components combine to explain their data. We show that the dilution of one component by more than ca. 25% from another component can result in linear demagnetisation curves that decay to the origin on orthogonal plots, but whose best-fit direction can significantly deviate from both end-members. The efficacy of the method is demonstrated through examples of demagnetisation data from hematite and/or magnetite-bearing sandstones from China. This method can be broadly applied to all multicomponent magnetisation problems in palaeomagnetism.

Reference

This chapter has been published as an article by Geophysical Journal International.

Tonti-Filippini, J. A., and Gilder, S. A. (2023). Vector unmixing of multicomponent palaeomagnetic data. Geophysical Journal International, 233(3), 1632-1654.

Contributions

JT and SG jointly conceived the idea for this study. JT devised the MATLAB programs and wrote the manuscript with input from SG.

1.1 Background

Detailed observations of Earth's magnetic field date back to the 16th century, as sailors required precise field observations to navigate the oceans (Jonkers et al., 2003). To reconstruct the magnetic field prior to direct observations, palaeomagnetists rely on archives preserved in the geologic record. Retrieval of the palaeomagnetic signal from rocks is often complicated by the presence of multiple magnetisation components, where an original (primary) magnetisation has been partially or completely overprinted by secondary processes. For example, sedimentary rocks can suffer reworking by tectonic stress, chemical/thermal alteration and/or fluid flow, all of which can influence the original magnetic signature (e.g., Elmore et al., 2012). Determining whether the magnetisation components are primary or secondary is an important aspect of any palaeomagnetic study. Secondary components can also yield important information about the history of the rock and timing of tectonic events. However, despite more than 60 years of study, many mechanisms for remagnetisation are 'still obscure or incompletely known' (Van der Voo and Torsvik, 2012).

The remagnetisation dilemma is exemplified by the red bed controversy, which has long plagued the field of palaeomagnetism (Kodama, 2012). The controversy surrounds the origin of the remanent magnetisation carried by hematite in sedimentary rocks. Hematite is often categorised as pigmentary or specular. Pigmentary hematite, responsible for the distinct blood-red colour, is typically formed by alteration of iron-rich minerals and often carries a secondary magnetisation in grains of sub-micron size, while specular grains are typically larger, ca. 10 - 300 μm (Sierra-Rojas and Molina-Garza, 2018). The presence of pigmentary hematite can usually be isolated by detailed thermal demagnetisation as it generally unblocks at temperatures lower than specular hematite, with a broad unblocking spectrum (Collinson, 1974). Specular hematite typically unblocks in a much narrower range between 600 – 690 °C (Özdemir and Dunlop, 2002, 2005). The timing of, and mechanisms for, the formation of magnetisation in specular hematite (primary or secondary) lie at the heart of the red bed controversy.

The case for primary magnetisation in specular hematite relies on the ability of detrital hematite grains to align with Earth's field during deposition via torque, forming a detrital remanent magnetisation (DRM) which is locked into the rock during diagenesis. The case for secondary magnetisation necessitates the precipitation of specular hematite during or sometime after diagenesis resulting in a chemical remanent magnetisation (CRM). The majority view according to Robert Butler's textbook on palaeomagnetism (Butler, 1992) is that red beds probably carry a CRM formed during early diagenesis; the minority view is that specular hematite in some red beds could carry a DRM and that DRM generally occurs in more mature, clastic/coarse-grained rocks.

There is strong evidence for both the DRM and CRM mechanisms, and it seems as though specular hematite can carry either or both (see Kodama, 2012, and references therein). Kodama (2012) argued that there should be a swing towards the minority (DRM) view a la Butler; however, Kodama (2012) recognised that the age of red bed remanence needs to be considered on a case-by-case basis. Meng et al. (2022) demonstrated that Cretaceous red beds in South China were partially or wholly chemically overprinted with

secondary hematite growth occurring within 2 Myr of the age of sedimentation; for tectonic purposes, 2 Myr uncertainty is generally less than the precision on the age of fossil-poor continental sediments.

Identifying and quantifying the relative contributions of DRM and CRM components in hematite-bearing sediments is notoriously difficult. Separation of components by thermal demagnetisation alone can be nearly impossible, as the components tend to demagnetise over similar unblocking ranges; alternating field (AF) demagnetisation is impracticable as hematite can have a maximum coercivity >10 T (Rochette et al., 2005). Distinguishing different populations of hematite grains is difficult with conventional microscopy or scanning electron microscopy (SEM), as hematite grains are often sub-micron in size and occur in several different habits (Walker et al., 1981).

Kirschvink (1980) developed a method to separate magnetic components using principal component analysis (PCA) through the visualisation of Zijderveld diagrams (Zijderveld, 1967). Magnetic components in rocks are typically determined by analysis of stepwise demagnetisation data, and a rock-magnetic component can be defined by its relative contribution to the decay of remanence over a certain temperature range (during thermal demagnetisation) or field range (during AF demagnetisation). Assuming the ambient magnetic field was stable during formation of the component, demagnetisation of a rock-magnetic component will yield a straight line on a Zijderveld diagram and can be used to define a palaeomagnetic component with a specific direction, based on the resultant vector orientations of individual steps. A palaeomagnetic component has geophysical meaning when the remanence was locked-in parallel to Earth's field and, when seen in this way, should be consistent across a suite of rocks deposited in the same field conditions. However, unblocking spectra from multiple components (formed at different times) can overlap and complicate determination of palaeomagnetic directions, so palaeomagnetists commonly employ field tests to determine the lock-in timing of magnetic components, e.g. fold and reversal tests (Van der Voo, 1990). Kirschvink (1980) detailed three scenarios in which PCA can resolve palaeomagnetic components:

1. Progressive removal of well-defined individual components, which results in a series of co-linear directions (i.e., straight lines on a Zijderveld diagram);

2. Simultaneous removal of two *discrete* magnetic components in differing ratios, which results in a series of coplanar points (i.e., a great circle or two-dimensional curved line on a Zijderveld diagram);

3. Simultaneous, progressive removal of more than two discrete magnetic components, which results in a three-dimensional curve (i.e., a spiralling Zijderveld diagram).

The first three cases were well illustrated by Hoffman and Day (1978), where determination of a palaeomagnetic component relies on the existence of a 'window' in the unblocking spectrum in which only one component is demagnetised (Dunlop, 1979). However, it is possible that the unblocking spectra of two or more components overlap completely and may escape detection with PCA if both components are removed simultaneously (Van der Voo, 1990). Therefore there is a fourth case that cannot be resolved by PCA alone:

4. Simultaneous removal of two or more *non-discrete* magnetic components, with superimposed demagnetisation spectra, which results in a linear component on a Zijderveld diagram.

In all four cases, the components are assumed to be temporally distinct, i.e. they represent generations of particles formed or magnetised under different magnetic field conditions so that discrete field directions were recorded. There could be another situation (v) where the ambient field varies during formation of a rock-magnetic component, but this could not be analysed without knowing it *a priori* and is beyond the scope of this study.

If specular hematite in a sedimentary rock carries both CRM and DRM components that formed at different times, then conventional PCA could be incapable of discriminating them, so other methods to mathematically unmix the components are desirable. Dinarès-Turell and McClelland (1991) warned that a complete overlap of two components can produce a spurious single component with a linear decay path during thermal demagnetisation, although the components could be isolated by alternating field (AF) demagnetisation if they are carried by grains with different coercivity spectra. However, such techniques are not always applicable or successful, especially when considering magnetisations carried by hematite. Halim et al. (1996) identified superimposed remanent magnetisations in Cretaceous red beds which could not be separated with AF experiments but, by generating synthetic demagnetisation data, showed that an apparent intermediate component could be an artefact of combined high and low temperature components with completely overlapping unblocking spectra.

We are unaware of any generalised method to resolve superimposed magnetic components that produce linear demagnetisation decay paths. Halls (1978) demonstrated that two superimposed magnetisation components could be separated in Precambrian rocks using convergent remagnetisation circles. However, the great circle method can only isolate a secondary (younger) component when there is sufficient directional dispersion with respect to the initial (older) component to produce convergent remagnetisation paths. Halls (1978) also recognised that remagnetisation circles are relatively insensitive when two magnetisation components overlap to the extent that neither end-member is resolvable.

In this paper, we present a method to mathematically separate two to three non-discrete or superimposed magnetic components and apply this method to thermal demagnetisation data from hematite-bearing sandstones from China. Although we apply this method to natural remanence magnetisations carried predominantly by hematite, this method can be broadly applied to multicomponent magnetisation problems with any magnetic remanence carrier (e.g., magnetite). Our method is able to systematically quantify absolute and relative contributions of end-member components from stepwise demagnetisation data.

1.2 Synthetic examples

This section gives examples of mixing two or three synthetic demagnetisation curves, as well as the unmixing of combined results using variable vector addition/subtraction and inverse modelling.

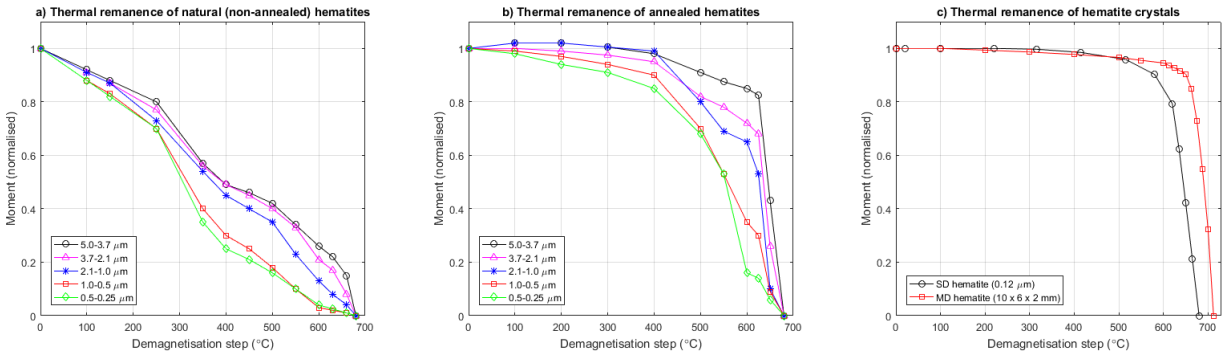

Figure 1.1: Remanence unblocking curves for aggregates of (a) non-annealed and (b) annealed natural hematites (Dekkers and Linssen, 1989) and (c) SD and MD hematite crystals (Özdemir and Dunlop, 2002, 2005).

1.2.1 Input remanence curves

Hematite displays a wide range of unblocking behaviour during thermal demagnetisation that depends on domain state, grain size, degree of crystallinity and the presence of inclusions or lattice substitutions (Özdemir and Dunlop, 2014), so choosing a characteristic reference curve is subjective. Dekkers and Linssen (1989) published thermal remanence curves for artificial samples containing different size fractions of fine-grained natural hematite powders/aggregates before and after annealing (Figs. 1.1a and b). Collinson (1974) separated pigmentary and specular hematite grains and showed that pigmentary hematite unblocks over a broad temperature range with a regular decrease in moment from low temperature until 600 °C, which was the highest temperature achieved in those experiments (and only unblocked to $20 - 40\%$ of the initial remanence). Özdemir and Dunlop (2002, 2005) measured thermal remanence curves for single-domain (SD) and multi-domain (MD) hematite crystals and found that both unblocked in a narrow range at high temperatures (Fig. 1.1c), although the larger MD hematite grain unblocked at slightly higher temperatures than the < 1 micron SD hematite grains (Fig. 1.1c).

In the following examples we use unblocking spectra from Dekkers and Linssen (1989) to demonstrate the problem of determining directions from completely overlapping magnetic components. We interpolated the data to the demagnetisation steps used in the latter case study (Section 1.3.2), and assigned them directions to represent palaeomagnetic components. We then combine the components in varying proportions as if they represent primary and secondary components.

1.2.2 Combining two synthetic components (simple)

We used the annealed remanence curve for the largest grain size fraction, 3.7 - 5.0 μm, in Fig. 1.1(b) as representative of a rock-magnetic component with primary hematite, and applied antipodal directions for palaeomagnetic components A and B with declination $D_a = 13°$ and inclination $I_a = 77°$ (Fig. 1.2a) and $D_b = 193°$ and $I_b = -77°$ (Fig. 1.2b). We used the non-annealed curve of the same size fraction in Fig. 1.1(a) to represent an overprint

Table 1.1: Example directions used for input components A – D (Figs. 1.2a-d) and the results of PCA for mixed Zijderveld diagrams (Figs. 1.2e-h). The best-fit PCA directions (declination and inclination) were based on lines forced to the origin containing six demagnetisation steps between 670 – 680 °C; MAD values do not exceed 0.1°. The best-fit components lie on great circle paths between the respective input components. θ_{dev} is the angular distance between the primary direction (A or B) and the mixed direction calculated from the best fit procedure. The components were combined in equal proportions.

Component	Dec. (°)	Inc. (°)	θ_{dev} (°)	Fig.
Input A (primary)	13	77	-	1.2(a)
Input B (primary)	193	-77	-	1.2(b)
Input C (overprint)	138	-46	-	1.2(c)
Input D (overprint)	6	4	-	1.2(d)
Output A+C	100	64	28.3	1.2(e)
Output B+C	159	-69	12.4	1.2(f)
Output A+D	8	54	23.1	1.2(g)
Output B+D	1	-72	30.8	1.2(h)
Output A+C+D	37	47	31.5	1.5(a)
Output B+C+D	83	-79	19.7	1.5(b)

and applied directions $D_c = 138°$ and $I_c = -46°$ (Fig. 1.2c) and $D_d = 6°$ and $I_d = 4°$ (Fig. 1.2d) for palaeomagnetic components C and D. The directions applied for components A – D are the same as those used in the Yangjiaping case study described in Section 1.3.2 (components C1 – C3). Figs. 1.2(e-h) show the various results of combining a primary magnetisation (A or B) with an overprint (C or D) in equal proportions to highlight the problem with performing PCA when there are two components with completely overlapping unblocking spectra.

The output Zijderveld diagrams (Figs. 1.2e-h) decay linearly to the origin above 670°C, thereby leading to false or misleading characteristic remanent magnetisation (ChRM) directions with PCA. ChRM directions lie on a great circle between the two input directions (PCA results in Table 1.1). In Fig. 1.2(e), the resultant Zijderveld diagram produces a linear path to the origin between 670 – 680 °C, with a direction of $D = 100°$ and $I = 64°$, which most users would consider as a ChRM even though it deviates from the true (component A) direction by 28.3° (angular distance). As the input directions in this case are quite different (Table 1.1), the effect of component C on component A is noticeable on a Zijderveld diagram. The effect is more subtle if the two components have similar orientations, as shown in Fig. 1.2(f) where components B and C both have reversed polarities. In this case, the ChRM of component B is deviated by 12.4°. When the input components both have normal polarities but significantly different inclinations, component A deviates by 23.1° (Fig. 1.2g). Combining components B and D yields an offset of 30.8° from the intended primary direction (Fig. 1.2h). These examples highlight the potential pitfalls of

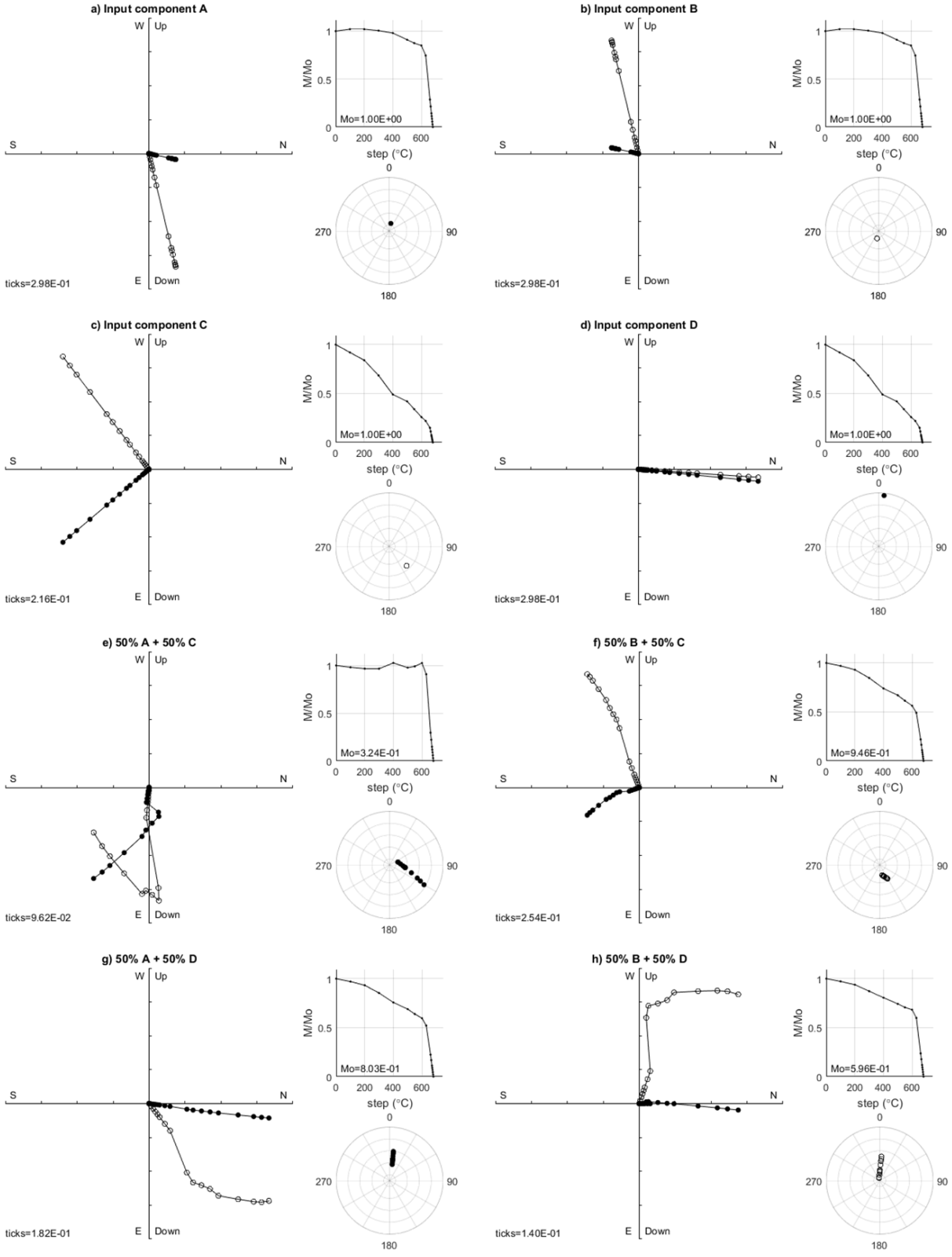

Figure 1.2: (Caption next page.)

Figure 1.2: (Previous page.) Examples of combining two synthetic magnetisation components. (a-d) Zijderveld diagrams, remanence plots and stereonets for input components A-D. (e-h) Output of mixing/combining components A+C, B+C, A+D and B+D with equal proportions (1:1). The Zijderveld diagrams display linear decay paths between 670 - 680 °C which could be falsely interpreted as ChRM directions with PCA (see directions in Table 1.1). In these and all subsequent Zijderveld diagrams, filled circles represent the horizontal plane (declination) while open circles indicate the vertical plane (inclination). In the stereonet plots, filled circles represent downward pointing (normal) directions while open circles represent upward pointing (reversed) directions.

Table 1.2: PCA results for synthetic Zijderveld diagrams and remanence curves for mixing two input components, A and C in the proportions indicated (Fig. 1.3). The output PCA directions lie on a great circle between the respective input components; n, temperature interval and MAD are the same as in Table 1.1. θ_A and θ_C are the respective angular distances from the output PCA direction to the A and C directions.

Component	Dec. (°)	Inc. (°)	θ_A (°)	θ_C (°)	Fig.
100% A + 0% C	13	77	0	142.2	1.3(a)
80% A + 20% C	37	78	5.3	137.0	1.3(b)
60% A + 40% C	80	73	16.8	125.5	1.3(c)
40% A + 60% C	114	42	51.7	90.6	1.3(d)
20% A + 80% C	130	-22	117.4	24.9	1.3(e)
0% A + 100% C	138	-46	142.2	0	1.3(f)

performing PCA when the unblocking spectra of multiple components are superimposed.

1.2.3 Combining two synthetic components (variable)

In this example, we take the same input components A and C as above and mix them in varying proportions. Figs. 1.3(a-f) shows how the Zijderveld diagrams change from 100% component A to 100% component C in 20% increments. During the progression, the Zijderveld diagrams maintain linear decay paths to the origin between 670 – 680 °C and yield best-fit directions that lie along a great circle between the two end-member directions (Fig. 1.3h and Table 1.2).

1.2.4 Unmixing two synthetic components

Considering the results in Fig. 1.3, it may be desirable to unmix a Zijderveld diagram suspected of carrying two superimposed magnetisation components. To do this we apply simple inverse modelling where a range of possible model permutations (i.e. different

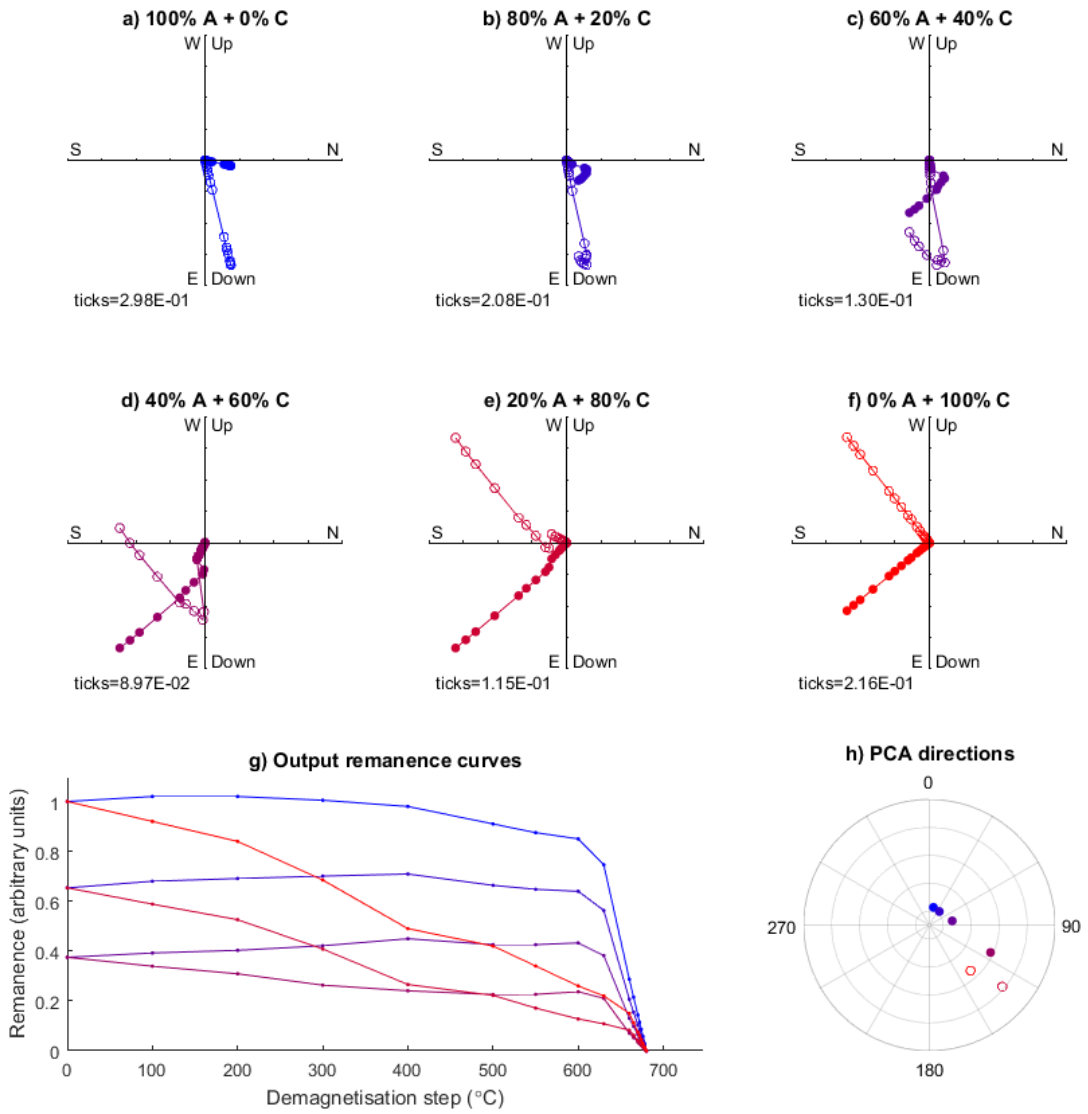

Figure 1.3: Examples of resultant Zijderveld diagrams (a-f) and remanence curves (g) for mixing two input components, A and C (Figs. 1.2a and c) with variable contributions (0 − 100%) of each component. Throughout the progression, the Zijderveld diagrams maintain linear decay paths between 670 - 680 °C which could be falsely interpreted as ChRM directions using conventional PCA. The output PCA directions (h) lie on a great circle between the two input components (Table 1.2).

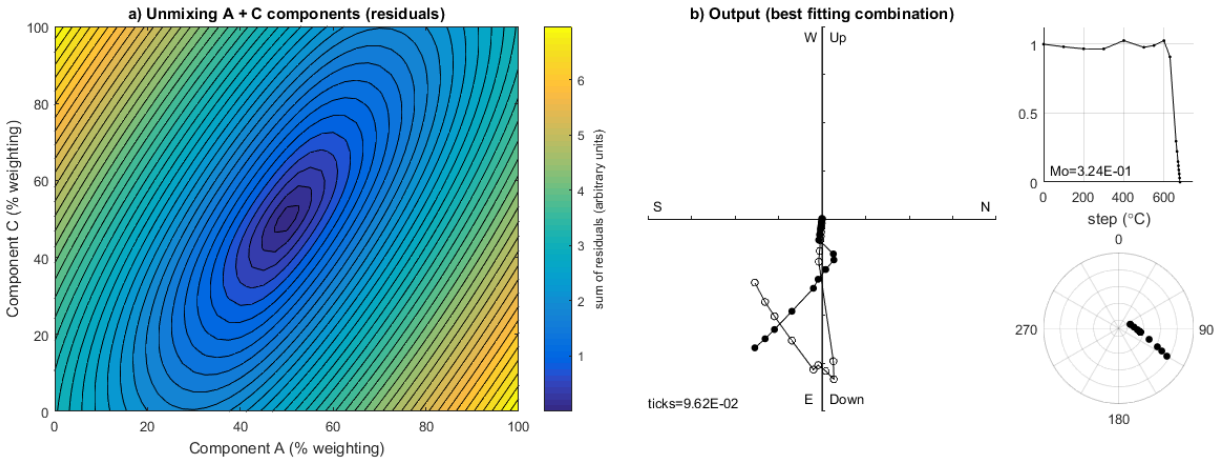

Figure 1.4: (a) Contour plot of residual sums for the unmixing of combined components A and C (remanence curve in Fig. 1.2e). (b) Best fitting combination of components A and C. The inverse modelling perfectly resolves the two end-members with 100% *GOF and gives a best fitting solution with* 50% *weighting for each component.*

weightings of the individual components) are calculated and compared to the original Zijderveld diagram. The relative contribution of each component is output from the best-fitting model. The modelling requires three remanence decay curves (with moment vectors for each demagnetisation step) as inputs, one for the mixed ensemble and one for each of the two suspected end-member components. To illustrate this example we use artificial data from known inputs, i.e. the mixed result from Fig. 1.2(e) (50% component A and 50% component C), and the two end-member components A (Fig. 1.2a) and C (Fig. 1.2c).

With a matrix resolution of 40 x 40, 1600 mixing models are calculated and compared to the mixed input data (Fig. 1.4a). Each mixing model is a unique combination of the two end-member components, like those in Figs. 1.3(a-f). For every model (i.e. each point in the matrix), the sum of the residuals (e) is calculated as the total Euclidean distance between the input data ($\vec{d}$) and model ($\vec{m}$) vectors in Cartesian coordinates across all demagnetisation steps (s):

$$e = \sum_{s=1}^{n} \sqrt{(d_{x,s} - m_{x,s})^2 + (d_{y,s} - m_{y,s})^2 + (d_{z,s} - m_{z,s})^2} \tag{1.1}$$

With this approach, the vector differences are integrated along the entire demagnetisation spectrum and each demagnetisation step contributes equally to the selection of the best-fitting model (Fig. 1.4b). Naturally, the vectors farthest from the origin of the Zijderveld plot will have the greatest influence on the residual sum and therefore the eventual selection of the best-fitting model (as is also the case with PCA). The goodness of fit (GOF) is expressed as the complement of the residual sum (e) divided by the total length of the input data vectors ($\vec{d}$) across all demagnetisation steps (s):

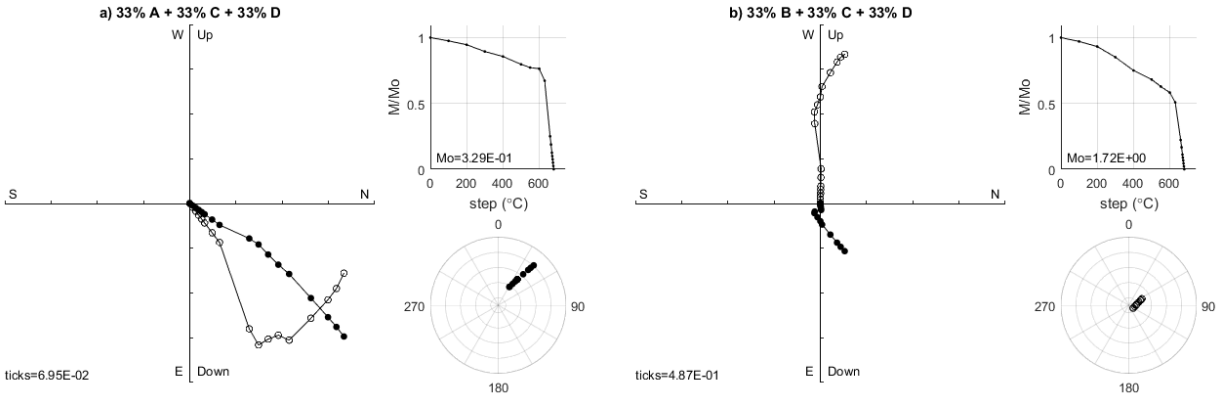

Figure 1.5: Examples of mixing three components with equal weighting (1:1:1) (a) components A, C and D (Figs. 1.2a, c and d), and (b) components B, C and D (Figs. 1.2b, c and d). The Zijderveld diagrams maintain linear paths to the origin between 670 - 680 °C. PCA results are shown in Table 1.1.

$$goodness\ of\ fit\ (GOF) = 1 - \frac{e}{\sum_{s=1}^{n} \left|\vec{d}_s\right|} \tag{1.2}$$

where 0 = no fit and 1 = perfect fit. Other methods of scoring the model fits are possible, e.g. with angular deviation or cosine similarity, but we prefer this method as it considers the fit of the vectors in both magnitude and direction.

The result of unmixing Fig. 1.2(e) is shown by the 2D contour plot in Fig. 1.4(a). In this simple case, the inverse modelling was able to fully resolve the two end-member components A and C with 100% GOF; e.g., the solution gives 50% weighting for each component (Fig. 1.4b). It can be observed that the solution space is better constrained by component A, which has higher remanence magnitudes across more of the demagnetisation spectrum than component B.

1.2.5 Combining three synthetic components

This example treats three magnetisation components by combining A, C and D (Figs. 1.2a, c and d) and B, C and D (Figs. 1.2b, c and d) using equal weighting (33.33%) for each component (Figs. 1.5a and b). The Zijderveld diagrams still exhibit linear decay paths between 670 – 680 °C (six demagnetisation steps, MAD $< 0.2°$) (Table 1.1). The best-fit line direction of combined components A+C+D (Fig. 1.5a) is deviated 31.5° with respect to input component A, while that for components B+C+D (Fig. 1.5b) is deviated 19.7° with respect to component B.

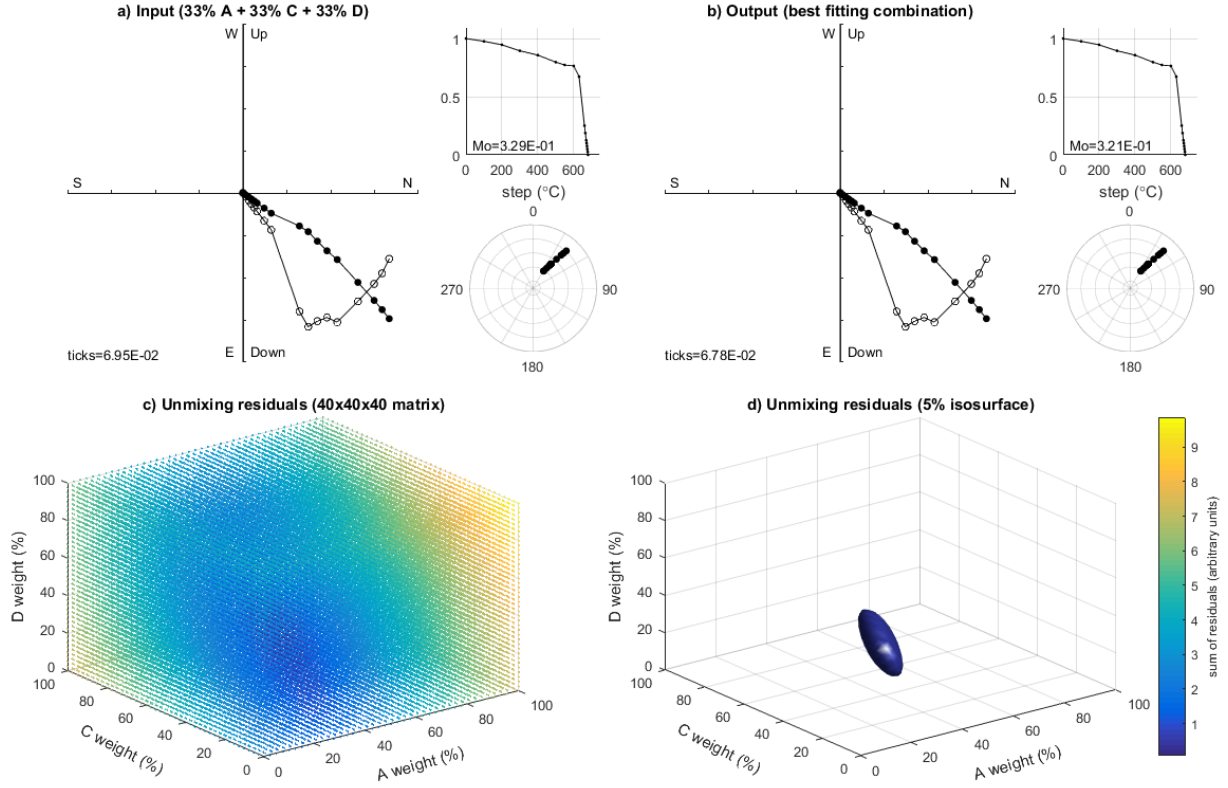

Figure 1.6: (a) The three-component unmixing result of the combined curve from Fig. 1.5(a) which accurately resolves and quantifies the contributions of the input end-member components A, C and D (Figs. 1.2a, c and d). The best-fitting model (b) has a near-perfect goodness of fit of 97.50%, which is only limited by the resolution of the model matrix (c-d), which estimates equal contributions of 32.5% *for each component.*

1.2.6 Unmixing three synthetic components

Now we take the artificial remanence curve from Fig. 1.5(a) and attempt to resolve the three end-member components A, C and D (Figs. 1.2a, c and d). We apply the same method as above albeit the inverse modelling is more computationally expensive going from two components to three. A residual sum matrix with a resolution of 40 x 40 x 40 computes 64,000 individual models, which is sufficient for palaeomagnetic applications. Computation time for one specimen takes less than 30 seconds using a laptop with a 2.38 GHz processor and 8 GB of RAM. Fig. 1.6 displays the unmixing result of Fig. 1.5(a) into the three end-member components A, C and D. The best-fitting model resolves 97.5% of the mixed input (GOF) and finds an equal weighting for all end-member components of 32.5%, compared to the actual value of 33.3%. The latter could be achieved if one increased the size of the matrix at the expense of increased computational time.

1.3 Application to hematite-bearing sandstones

In the previous section we demonstrated that the vector unmixing method functions well for synthetic data. In this section we demonstrate the method with real data from two palaeomagnetic studies of hematite-bearing sandstones from China (Gilder and Courtillot, 1997; Tonti-Filippini et al., 2021).

1.3.1 Case study 1: Qinling (North China)

Gilder and Courtillot (1997) reported palaeomagnetic data from Middle Jurassic to Cretaceous rocks in and around the Qinling suture between the North and South China plates. Thermal demagnetisation of the Middle Jurassic red beds revealed two magnetisation components: a north-northeast and down component (geographic coordinates) at temperatures < 550°C and a north and down or south and up component (stratigraphic coordinates) above 550°C until complete unblocking around 680°C. The low temperature component failed the fold test while the high temperature component passed the fold and reversal tests, indicating the high temperature component was a primary remanence carried by hematite. The low temperature component possesses only normal polarity directions with an overall mean in geographic coordinates (Dg = 16.9°, Ig = 59.2°, α_{95} = 2.7°, k = 157.7) that is distinct from the recent (1995, D = -4.0°, I = 47.2°) or geocentric axial dipole directions (D = 0°, I = 51°). The overall mean is indistinguishable at 95% confidence limits (McElhinny, 1964) from nearby Cretaceous strata whose tilt-corrected (stratigraphic) magnetisations are solely of normal polarity, pass the fold test and are carried by magnetite and/or hematite (Ds = 18.0°, Is = 50.6°, α_{95} = 4.2°, k = 131.5). We can therefore assume that the overprint direction in the Middle Jurassic strata was locked in after folding by secondary hematite growth during the Cretaceous normal superchron. Under this assumption we attempted to unmix the Cretaceous overprint from the primary Middle Jurassic component.

Unmixing Middle Jurassic and Cretaceous data (simple)

We compiled a Cretaceous end-member component from the tilt-corrected demagnetisation data of 16 specimens from Cretaceous red bed sites C526 and C529 by computing the medians of the individual moment vectors (Fig. 1.7a). Specimen masses were not measured, so we used volume-normalised moments (A/m) for all calculations assuming all specimens had perfect cylindrical shapes with volumes of 11 cm^3. The lower left Zijderveld diagram (Fig. 1.7b) represents the median of the 16 specimens across all demagnetisation steps. PCA of the median curve determined on the 662 to 698 °C interval yields Ds = 17.5°, Is = 53.3°, MAD = 6.9° , very similar to the group mean direction of Ds = 18.0° and Is = 50.6° obtained by Gilder and Courtillot (1997). The < 400°C steps appear to contain a (probably present-day) viscous overprint; for modelling purposes we applied the best-fit PCA direction to all steps while respecting the total moment decay, yielding the idealised Zijderveld diagram on the lower right (Fig. 1.7c) – this produced better results than using

the raw median curve.

In the same manner, we calculated the median Zijderveld plots for two Middle Jurassic sites: C508 with normal polarity and C509 with reversed polarity (Supplemental [Suppl.] Figs. A.1a and b). We then unmixed the Cretaceous component (Fig. 1.7c) from the Middle Jurassic data in geographic (in situ) coordinates. The results are shown in Figs. 1.8(c and d), where 20% and 25% of the Cretaceous component were subtracted from sites C508 and C509, respectively, as found through trial and error. Assuming that only a single component should remain after subtraction of the Cretaceous component, one would expect to see a tight clustering of directions on a stereonet, precisely as observed in Figs. 1.8(c and d). These results suggest that the primary magnetisations in the Middle Jurassic red beds from sites C508 and C509 were partially overprinted by $20 - 25\%$ of the Cretaceous component.

Optimising and/or automating the component subtraction process, rather than applying brute trial and error (as in Fig. 1.8), can be achieved by assuming: (1) the subtraction of the secondary component should result in a single (primary) component (i.e. a tight clustering of remanence directions on a stereonet) and (2) the moment decay plot after subtraction should be invariant with respect to temperature (i.e. flat) in the low temperature part of the unblocking spectrum (e.g., between the first step and ca. 600°C) and then decay sharply at higher temperatures up until the Curie temperature, diagnostic of crystalline hematite (Figs. 1.1b and c). Achievement of these two conditions in Figs. 1.8(c and d) suggests that we are treating scenario (iv) described in Section 1.1.

Figs. 1.9(a and b) show examples of varying the relative contribution ($0 - 100\%$) of the median Cretaceous overprint, on the Middle Jurassic data (sites C508 and C509). For each weighting, the Fisher (1953) precision parameter κ was calculated on the individual directions across the entire demagnetisation range (all temperature steps). For site C508, the highest κ occurs at 17.5% removal of the Cretaceous overprint (Fig. 1.9a). For the reversed polarity site C509, κ was ineffective in determining an optimal solution as the Cretaceous component lies close to the antipode of the Jurassic direction. To find the optimal solution for site C509, the flatness of the thermal unblocking curve was estimated by calculating the standard deviation of the magnetisation intensities between 0°C and 600°C (in this case, the first eight demagnetisation steps), for brevity called σ_{flat}. The σ_{flat}-minimising algorithm gives an solution of 21.5% for site C509 (Fig. 1.9b).

Variable subtraction of Cretaceous component from Middle Jurassic specimens

In the previous example we calculated the effect of the Cretaceous overprint on the site mean data from two Middle Jurassic sites. It may also be desirable to see how the Cretaceous overprint varies between specimens. We performed the same analyses following Fig. 1.9 for each specimen in site C508 (Table 1.3) after variable subtraction of the Cretaceous component from the specimen demagnetisation data, using the κ-maximising algorithm (as in Fig. 1.9a). Subtracting the idealised Cretaceous (TC) curve in Fig. 1.7(c) produced the highest values for κ across the C508 specimens, so this was used to produce the resultant end-member profile in Suppl. Fig. A.2(b).

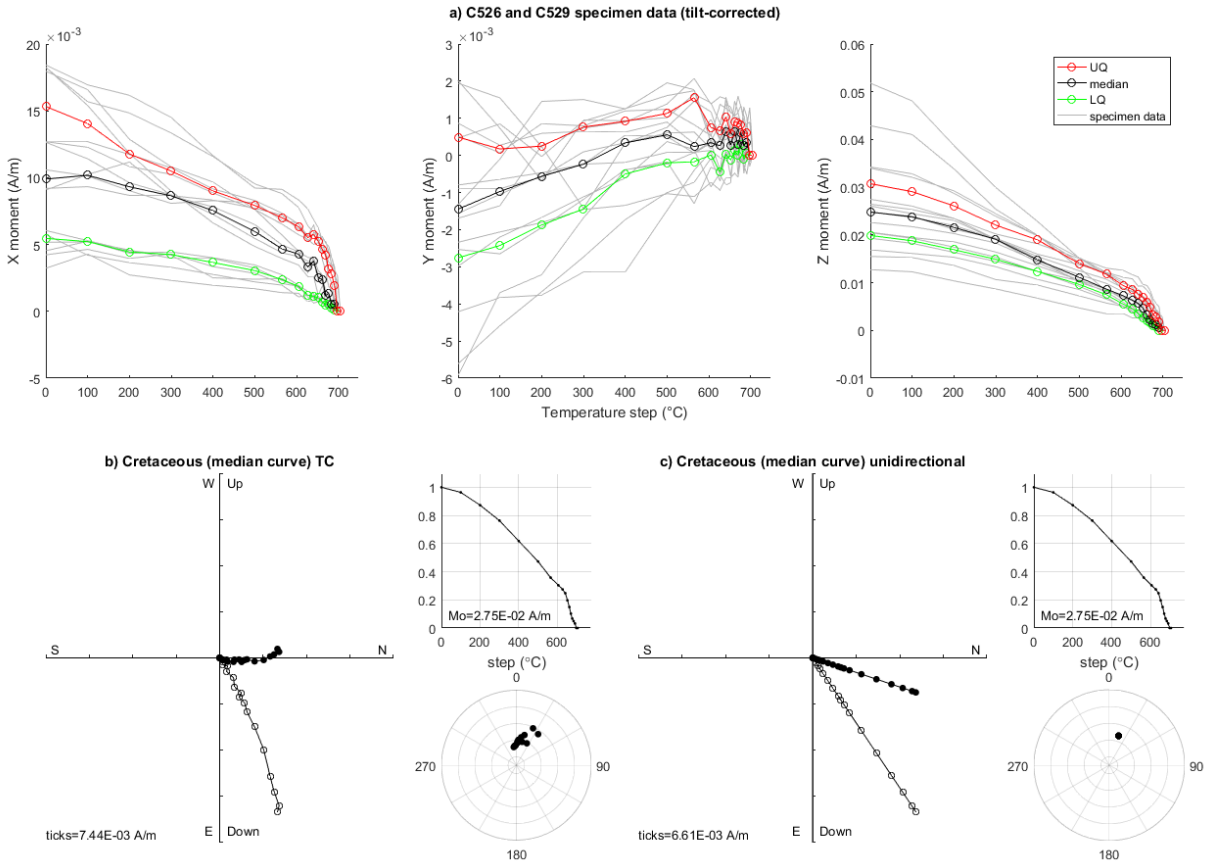

Figure 1.7: (a) Cretaceous red bed demagnetisation data of 16 representative specimens in stratigraphic (TC, tilt-corrected) coordinates from sites C526 and C529 in Gilder and Courtillot (1997). The median moment vectors across all demagnetisation steps for all specimens were calculated with lower (25%) and upper (75%) quartiles (LQ and UQ). (b) Zijderveld diagram respecting the moment vectors across all demagnetisation steps. (c) Zijderveld diagram with idealised curve to which a single direction (declination and inclination determined by PCA) was applied to all steps.

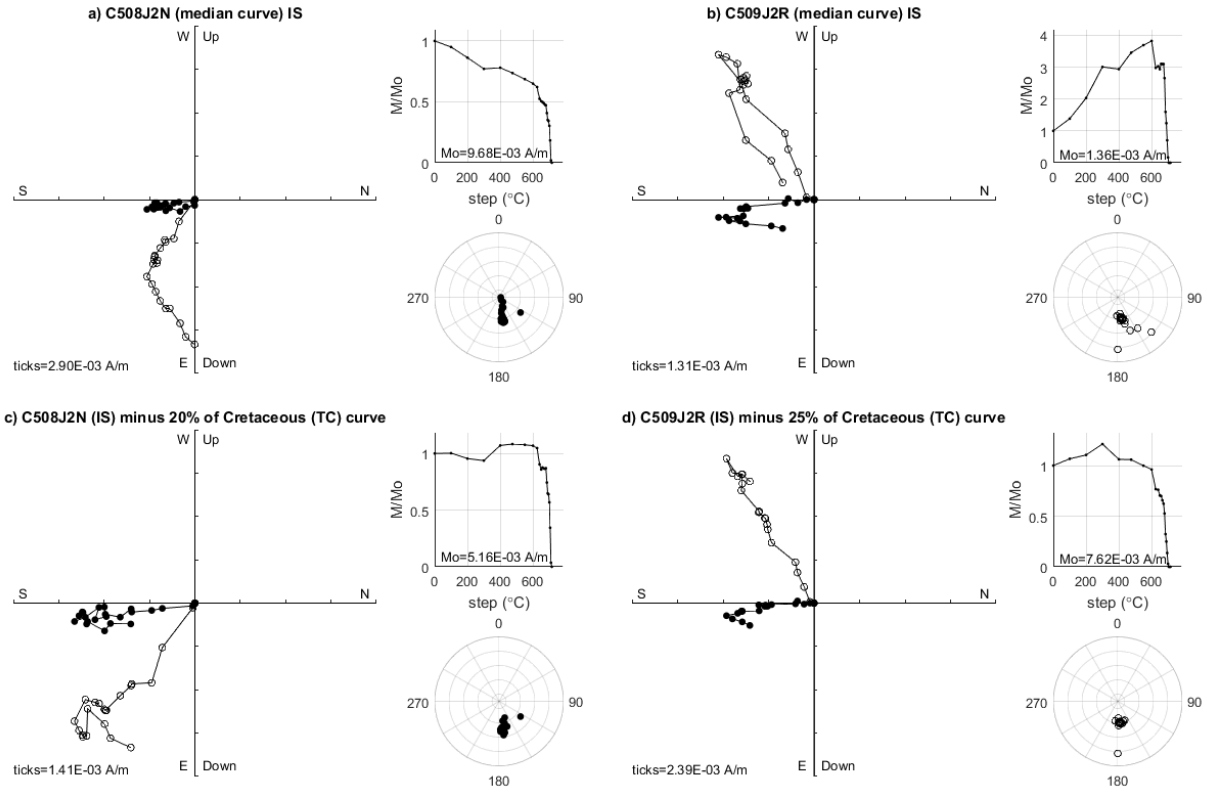

Figure 1.8: Median curves for the Middle Jurassic data (Suppl. Figs. A.1a and b) in geographic coordinates (IS, in situ) for (a) site C508 (normal polarity, N = 9) and (b) site C509 (reversed polarity, N = 7) (Gilder and Courtillot, 1997). (c and d) Resultant Zijderveld diagrams for sites C508 and C509 after subtracting 20% *and* 25% *of the Cretaceous overprint (Fig. 1.7c), respectively, as obtained through trial and error.*

Table 1.3: PCA results of the best solutions for variable subtraction of the Cretaceous component from specimens of the Middle Jurassic sites C508 and C509 (Gilder and Courtillot, 1997). The subtraction which produced the highest κ (dimensionless) was selected as the optimal solution for each C508 specimen, and the lowest σ_{flat} (expressed in 10^{-4} A/m) for each C509 specimen. The weighting of the subtraction is given as a percentage of the median NRM component derived from sites C526 and C529 (Fig. 1.7c). Declination and inclination (in situ coordinates) were calculated using PCA across all demagnetisation steps after subtraction of the Cretaceous component.

Site	Specimen	Subtraction (%)	κ or σ_{flat}	Dec (°)	Inc (°)
C508	5061	18.5	81	181.3	52.0
C508	5062	21.0	183	170.6	58.6
C508	5063	18.5	238	175.5	54.6
C508	5064	5.0	1097	165.0	52.8
C508	5065	7.0	730	173.3	54.6
C508	5066	15.0	393	188.1	61.1
C508	5067	14.5	559	163.7	65.8
C508	5068	16.0	185	201.7	55.5
C508	5069	19.5	175	197.0	44.6
C509	5071	11.5	6.8	180.0	-67.3
C509	5072	11.5	2.9	158.8	-68.7
C509	5073	18.5	4.5	175.9	-57.8
C509	5074	25.5	4.0	185.6	-69.5
C509	5075	26.5	4.1	185.5	-51.5
C509	5076	21.0	5.2	173.2	-55.5
C509	5077	41.0	5.5	206.1	-56.5

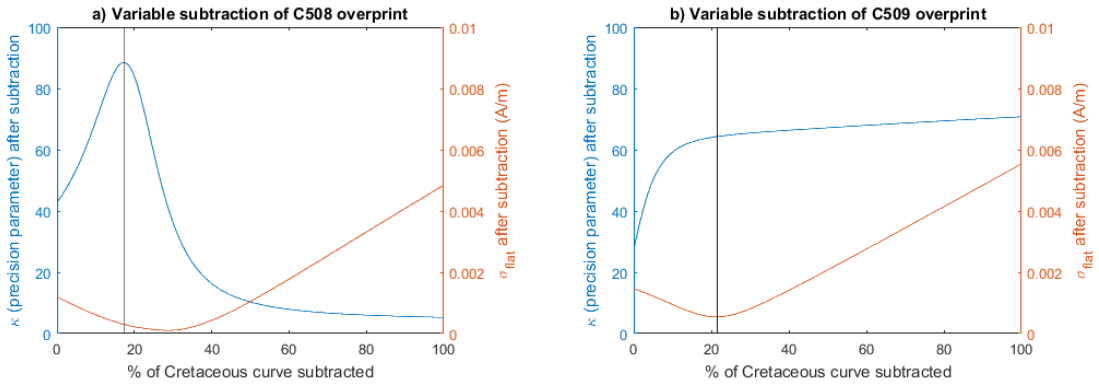

Figure 1.9: Variable subtraction of the Cretaceous overprint component (Fig. 1.7c) from Middle Jurassic sites (a) C508 and (b) C509. Black lines indicate the optimal solutions. In (a), the highest κ was used to determine a best-fitting solution with a contribution of 17.5%. In (b), κ could not be used, as the secondary (Cretaceous) component being subtracted lies close to the antipode of the primary (Middle Jurassic) component. In this case we used the σ_{flat}-minimising algorithm, which calculates the flatness of the remanence curve across the first eight demagnetisation steps (0 – 600 °C), to find a best-fitting solution of 21.5%; the κ-maximising algorithm did not yield a robust solution.

Inverse modelling of Jurassic specimens

As shown in Fig. 1.9(a), the solutions of the σ_{flat}-minimising and κ-maximising algorithms may not agree, so the user must decide which is the optimal solution. An alternative method utilises the median thermo-remanence curve determined for site C508 (after subtracting the Cretaceous component) to model the specimen results from site C509. In this example, we modelled the demagnetisation curve (in situ coordinates) for specimen 5072 (Fig. 1.10). We applied a smoothing function to the remanence curve obtained in Suppl. Fig. A.2(b) and applied the site mean in situ direction obtained with PCA for site C509, Dg = 178.8° and Ig = −65.3°, to define the idealised end-member curve in Suppl. Fig. A.2(c) – this is referred to as component 1 in Fig. 1.10, while component 2 is the Cretaceous end-member component previously derived in Fig. 1.7(c).

Each run in Fig. 1.10 generated 1600 forward models (40 x 40 matrix) following the same method as in Fig. 1.4. The solution resulting in the smallest residual sum was taken to be the optimal solution of each run. Statistics for each parameter in Fig. 1.10 were calculated by systematic exploration of the model space, i.e. the inverse modelling was rerun 144 times with unique pairs of the individual end member profiles (Figs. 1.7a and A.2a) instead of the median end member profiles (in this case, n = 16 * 9). The dispersion of each parameter in Fig. 1.10 is given by an interquartile range (IQR), i.e. the lower (25%) and upper (75%) quartiles (LQ and UQ). The best-fit weighting in Fig 1.10 is relative to the median NRM of the component's selected end-members. Proportional contributions to the total NRM are estimated by multiplying each component weighting by the corresponding median NRM and dividing by the sum of all components. Figs. 1.10(b and c) illustrate the

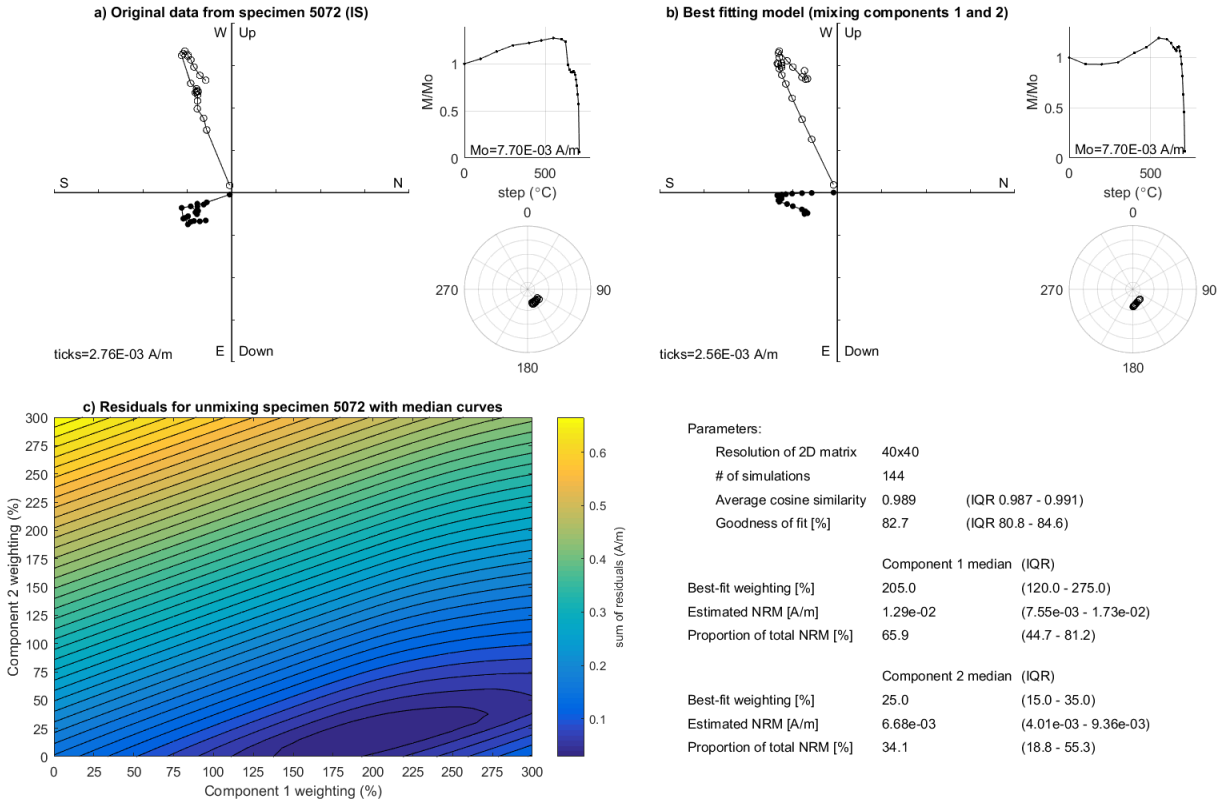

Figure 1.10: Result of inverse modelling for specimen 5072 (a) from Middle Jurassic site C509 (Gilder and Courtillot, 1997). Input component 1 has the previously derived shape of the end-member profile for site C508, with the PCA directions from site C509 applied (Suppl. Fig. A.2c). Input component 2 is the Cretaceous end-member component previously derived from sites C526 and C529 (Fig. 1.7c). The optimal solution (b) is the median result with the smallest residual vector sum (c). In this case, the modelling achieved a median GOF of 82.7% and ACS of 0.989.

best-fit result of the inverse modelling for the median components. In this example, the inverse modelling yielded a median GOF of 82.7% and weighting of 25% for component 2, which compares well to the result of 21.5% obtained by the σ_{flat}-minimising algorithm in Fig. 1.9(b).

The average cosine similarity (ACS) in Fig. 1.10 is a measure of the angular differences between the input specimen demagnetisation vectors ($\vec{d}$) and the output best-fitting model vectors ($\vec{m}$), similar to the R parameter of Fisher (1953). Cosine similarity ignores the vector magnitudes and is bound between 1 (exactly the same) and -1 (exactly the opposite). ACS is calculated by taking the mean of the cosine similarity across all demagnetisation steps (s):

$$average\ cosine\ similarity\ (ACS) = \frac{1}{n}\sum_{s=1}^{n}\frac{\vec{d}_s \cdot \vec{m}_s}{|\vec{d}_s||\vec{m}_s|} \tag{1.3}$$

ACS depends on the quality or noisiness of the demagnetisation data and the number of steps used, as well as the angular fit of the determined solution. Based on the results of our inverse modelling in Section 1.3.2, we propose a 'satisfactory' ACS threshold of > 0.7, > 0.8 for 'good', and > 0.9 for 'excellent'. The example in Fig. 1.10 yields an excellent ACS of 0.989.

1.3.2 Case study 2: Yangjiaping (South China)

In the previous section we showed that the vector unmixing method functions well for a case with two superimposed components. Now we test the method on a case with three superimposed components using data from Precambrian hematite-bearing sandstones collected in South China (Tonti-Filippini et al., 2021). PCA of thermal demagnetisation data revealed three distinct clusters of magnetic directions that appear to reside in different generations of hematite. The relative contributions from each component appear to vary among the 1188 specimens collected throughout the 85 m thick section. We assume that we are treating a conflation of temporally distinct palaeomagnetic signals, i.e. scenario (iv), rather than continuous mineral growth over time. Our intention was to quantify the respective contributions of the three magnetisation components in each specimen. In this case we were able to mass-normalise the data as opposed to the previous case which relied on volume-normalisation. Mass-normalisation is preferred due to its higher accuracy and hence better for inter-sample comparison.

Compiling end-member components for Yangjiaping

We selected representative specimens to compile the median curves in Fig. 1.11. Raw specimen data are shown in Suppl. Figs. A.3(a-d). Components 1 and 2 unblock in a narrow range, between 660 to 680°C, and display very similar thermal remanence behaviour despite preserving distinctly different palaeomagnetic directions. Component 1 (C1) contains dual polarity directions ($Ds_1 = 12.6°$ or 192.6°, $Is_1 = 77.1°$ or $-77.1°$, $\alpha_{95} = 7.5°$,

$n = 81$) (Figs. 1.11a and c), referred to as $C1_N$ and $C1_R$, while component 2 (C2) (Fig. 1.11e) has a single polarity direction ($Ds_2 = 138.1°$, $Is_2 = -46°$, $\alpha_{95} = 6.8°$, $n = 100$). Component 3 (C3) (Fig. 1.11g) unblocks between $100 - 660$°C and points north and down in geographic coordinates ($Dg_3 = 24.5°$, $Ig_3 = 55.9°$, $\alpha_{95} = 0.8°$, $n = 1002$), a direction which lies within 95% confidence limits of the Cretaceous component described in Section 1.3.1 (ca. 500 km to the northeast). C1 passes a reversal test and is interpreted to be primary. C2 is suspected to be a remagnetisation (CRM) formed sometime between the lock-in of C1 and C3. We ignored a viscous overprint that unblocked below 100°C in most specimens.

The end-member profile for C3 (Fig. 1.11g) was compiled by selecting representative specimens that contain solely this component (one single direction across the entire demagnetisation spectrum). Specimens bearing C1 and C2 always appear in combination with C3; therefore, to compile C1 and C2 end-members, we first subtracted C3 (median curve in Fig. 1.11g) to calculate the optimal solutions using the κ-maximising algorithm (Suppl. Fig. A.4). The NRM intensities of $C1_N$ and $C1_R$ agree to within 1% after subtracting the Cretaceous overprint (Figs. 1.11b and d), while C2 is 12% higher (Fig. 1.11f). C2 also has a more convex decay curve than C1, which supports our hypothesis that the two components have different formation mechanisms (i.e. CRM versus DRM).

As demonstrated in the preceding examples, specimens with superimposed components like C1 and C2 would be impossible to separate via PCA, as they unblock over the same temperature spectrum (Suppl. Fig. A.5). Component C3 unblocks below 660°C and across a much broader temperature range (Fig. 1.11g), so it should be resolvable with PCA. This is confirmed in Fig. 1.11(h) which combines the end-member components $C1_R$, C2 and C3 with respective weightings of 50%, 25% and 25%. Clearly there are at least two components present in the Zijderveld diagram and the directions trace a curved path on the stereonet. The component that does not decay to the origin gives a PCA direction of D = 13.0° and I = -0.4° (MAD = 10.9°, range = 0 – 500°C), similar to C3 in tilt corrected coordinates. Above 660°C the Zijderveld diagram decays linearly towards the origin with a ChRM direction of D = 145.6° and I = -69.4° (MAD = 3.9°, range = 660 – 680°C), an angular distance of 15.1° from the $C1_R$ direction.

Unmixing thermal remanence data from Yangjiaping

Assuming that all the Yangjiaping specimens carry some combination of these components, we ran the three-component inverse modelling function to find the best-fitting model for each specimen, i.e. the combination of component weightings for C1–C3 that best explains the observed thermal remanence unblocking behaviour. In these examples, we used idealised median curves for each component (Suppl. Fig. A.6) and explored the parameter space from 0 to 300% to account for all possibilities. The weightings are relative to the median curve, e.g. a weighting of 200% multiplies the component's median remanence curve by a factor of 2 across all demagnetisation steps. Naturally magnetic concentrations vary in each specimen, so the magnitude of each component's presence may be significantly different from the median remanence inputs. We ran the script successfully over 158 spec-

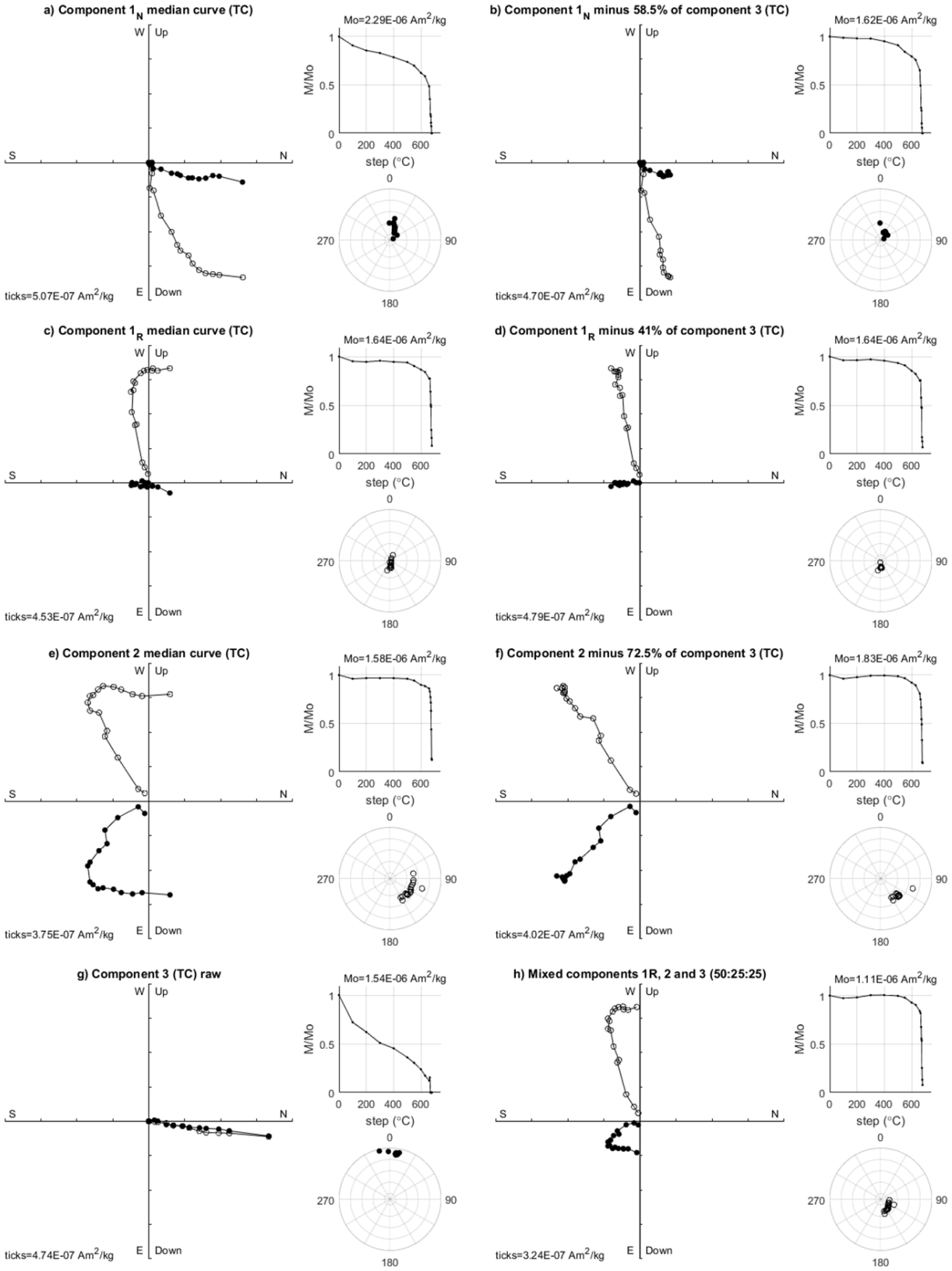

Figure 1.11: (Caption next page.)

Figure 1.11: (Previous page.) (a, c, e and g) Median curves of representative specimens for components $C1_N$, $C1_R$, C2 and C3 from the Yangjiaping section (Tonti-Filippini et al., 2021). Raw specimen data are shown in Suppl. Fig. A.3. (b, d and f) Median curves for $C1_N$, $C1_R$ and C2 after variable subtraction of C3 (Suppl. Fig. A.4). The NRM intensity of $C1_N$ and $C1_R$ match to within 1% after subtraction of the Cretaceous overprint (C3), while C2 is 12% higher. (h) Example of mixing end-member components $C1_R$, C2 and C3 with respective contributions of 50%, 25% and 25%. Note that the demagnetisation directions decay linearly to the origin at the high temperature steps (650 - 680 °C), yielding ChRM directions intermediate between $C1_R$ and C2. All data are mass-normalised (Am^2/kg) and in tilt-corrected (TC) coordinates.

imens and found that 88% produced 'satisfactory' GOFs > 60%, while 77% had 'good' GOFs > 70%, and 44% obtained 'excellent' GOFs > 80%. 96% of the specimens obtained an ACS > 0.7 (satisfactory), while 84% achieved an ACS > 0.8 (good), and 44% had an ACS > 0.9 (excellent).

Fig. 1.12 shows the best-fitting three-component unmixing solution for specimen YG4532A. The model has a high median GOF (84.4%), which indicates that the input data can be explained by a combination of only two components, C1 (67.5%) and C3 (75%). A remarkable similarity exists between the input and output Zijderveld diagrams, remanence decay plots and stereonets. A few spurious steps at the highest temperatures lowered the ACS to 0.887, but this is still considered 'good'.

The statistical distributions given in Fig. 1.12 were calculated by random (Monte Carlo) exploration of the model space (Tarantola, 2004), where the inverse modelling was rerun 1000 times with randomly selected triplets of individual end member profiles (Suppl. Fig. A.3). With three end member components, systematic exploration of the model space becomes much more computationally expensive (in this case, 4320 simulations would be required, where n = 12 * 12 * 30). A solution involving contributions from all three components is shown for specimen YG6598A (Fig. 1.13). The solution has a high median GOF of 84.6% and an excellent ACS of 0.982, explaining the input data by a combination of 70%, 200% and 140% weightings for C1, C2 and C3, respectively. The isosurfaces in Fig. 1.13 (and also Fig. 1.12) indicate that the best-fitting models are elongated along the Z (C3) axis, and more tightly constrained in the X (C1) and Y (C2) axes. Components C1 and C2 have higher remanence magnitudes across the unblocking spectrum (especially above 600°C) and therefore impose a greater influence on the magnitude of the residuals that constrain the solution space.

To model components with dual polarities (e.g. C1), it is easy to flip the polarity of the reference component direction by modifying the input component direction, i.e. adding or subtracting 180° to the declination and inverting the inclination. This was done for the C1 component ($C1_R$) of specimen YG5825A (Fig. 1.14). This could also be achieved by changing the sign of a component's moment vectors. The inverse approach yields a robust match over 85.6% (GOF) of the input data. The solution (Fig. 1.14d) is less tightly

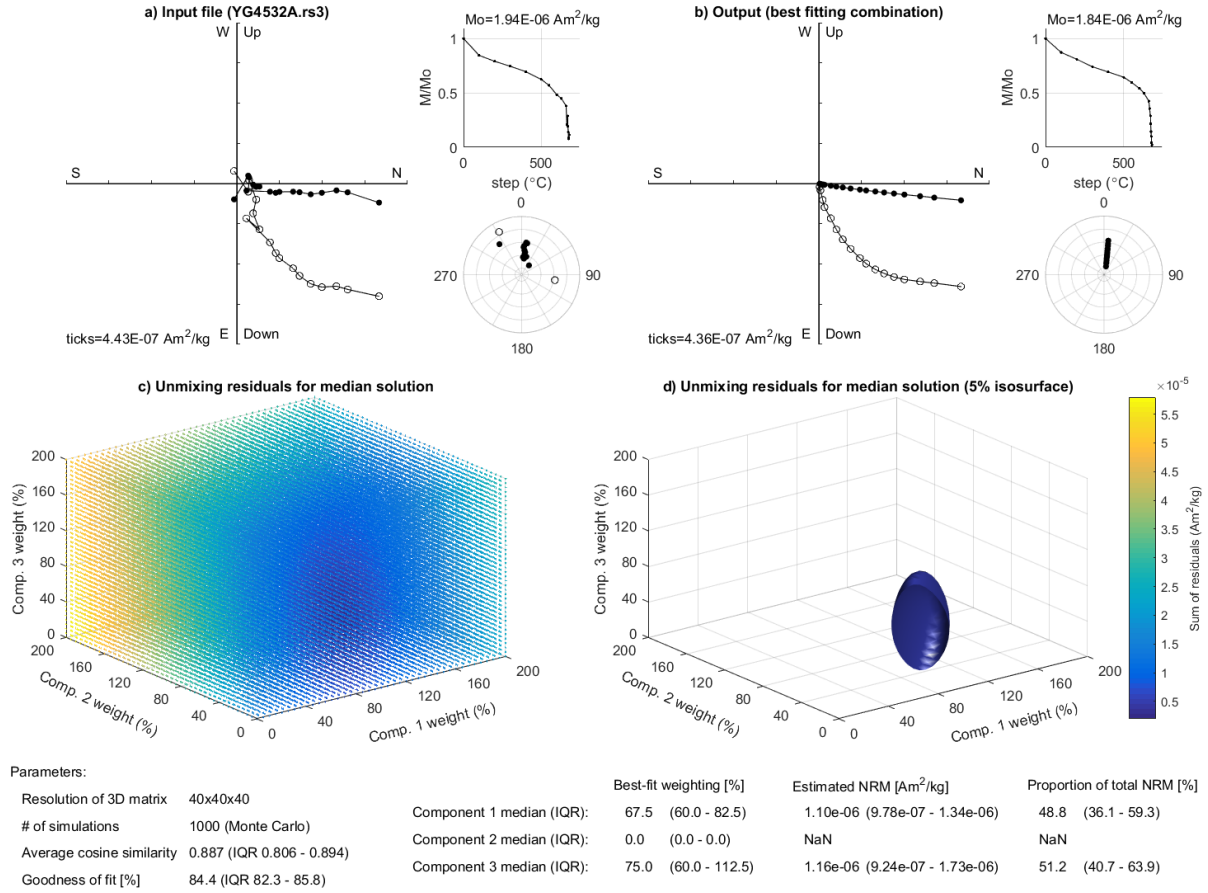

Parameters:

Resolution of 3D matrix	40x40x40
# of simulations	1000 (Monte Carlo)
Average cosine similarity	0.887 (IQR 0.806 - 0.894)
Goodness of fit [%]	84.4 (IQR 82.3 - 85.8)

	Best-fit weighting [%]		Estimated NRM [Am²/kg]	Proportion of total NRM [%]	
Component 1 median (IQR):	67.5	(60.0 - 82.5)	1.10e-06 (9.78e-07 - 1.34e-06)	48.8	(36.1 - 59.3)
Component 2 median (IQR):	0.0	(0.0 - 0.0)	NaN	NaN	
Component 3 median (IQR):	75.0	(60.0 - 112.5)	1.16e-06 (9.24e-07 - 1.73e-06)	51.2	(40.7 - 63.9)

Figure 1.12: Three-component unmixing result for Yangjiaping specimen YG4532A. The model describes a high median GOF – a 67.5% weighting of C1 and 75% of C3 explains 84.4% of the input remanence data. Several spurious steps at the highest temperatures lowered the median ACS to 0.887.

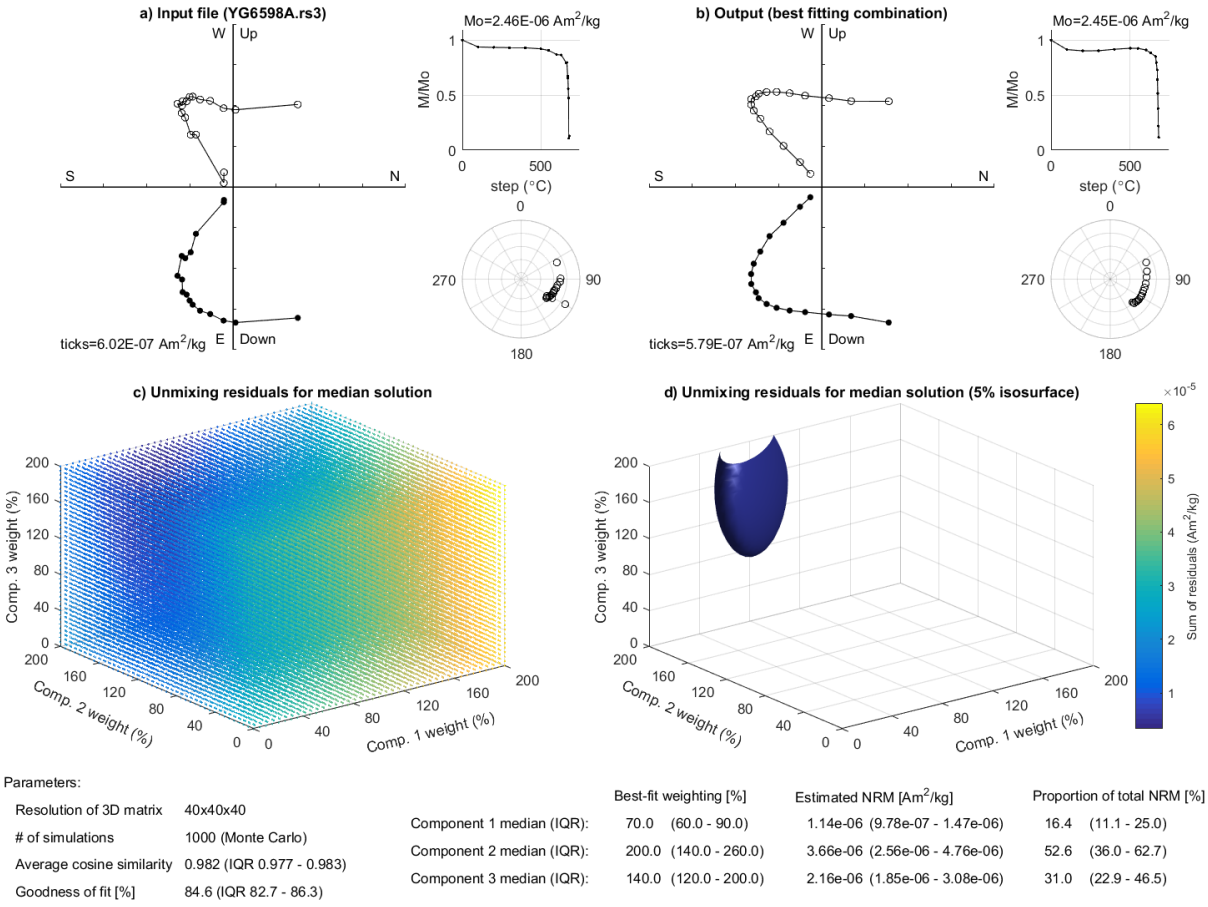

Parameters:

Resolution of 3D matrix	40x40x40
# of simulations	1000 (Monte Carlo)
Average cosine similarity	0.982 (IQR 0.977 - 0.983)
Goodness of fit [%]	84.6 (IQR 82.7 - 86.3)

	Best-fit weighting [%]	Estimated NRM [Am²/kg]	Proportion of total NRM [%]
Component 1 median (IQR):	70.0 (60.0 - 90.0)	1.14e-06 (9.78e-07 - 1.47e-06)	16.4 (11.1 - 25.0)
Component 2 median (IQR):	200.0 (140.0 - 260.0)	3.66e-06 (2.56e-06 - 4.76e-06)	52.6 (36.0 - 62.7)
Component 3 median (IQR):	140.0 (120.0 - 200.0)	2.16e-06 (1.85e-06 - 3.08e-06)	31.0 (22.9 - 46.5)

Figure 1.13: Three-component unmixing result for Yangjiaping specimen YG6598A. In this case, a model with 70% *,* 200% *and* 140% *weightings of components C1, C2 and C3 successfully explains* 84.6% *of the input data (GOF), with an excellent ACS of 0.982.*

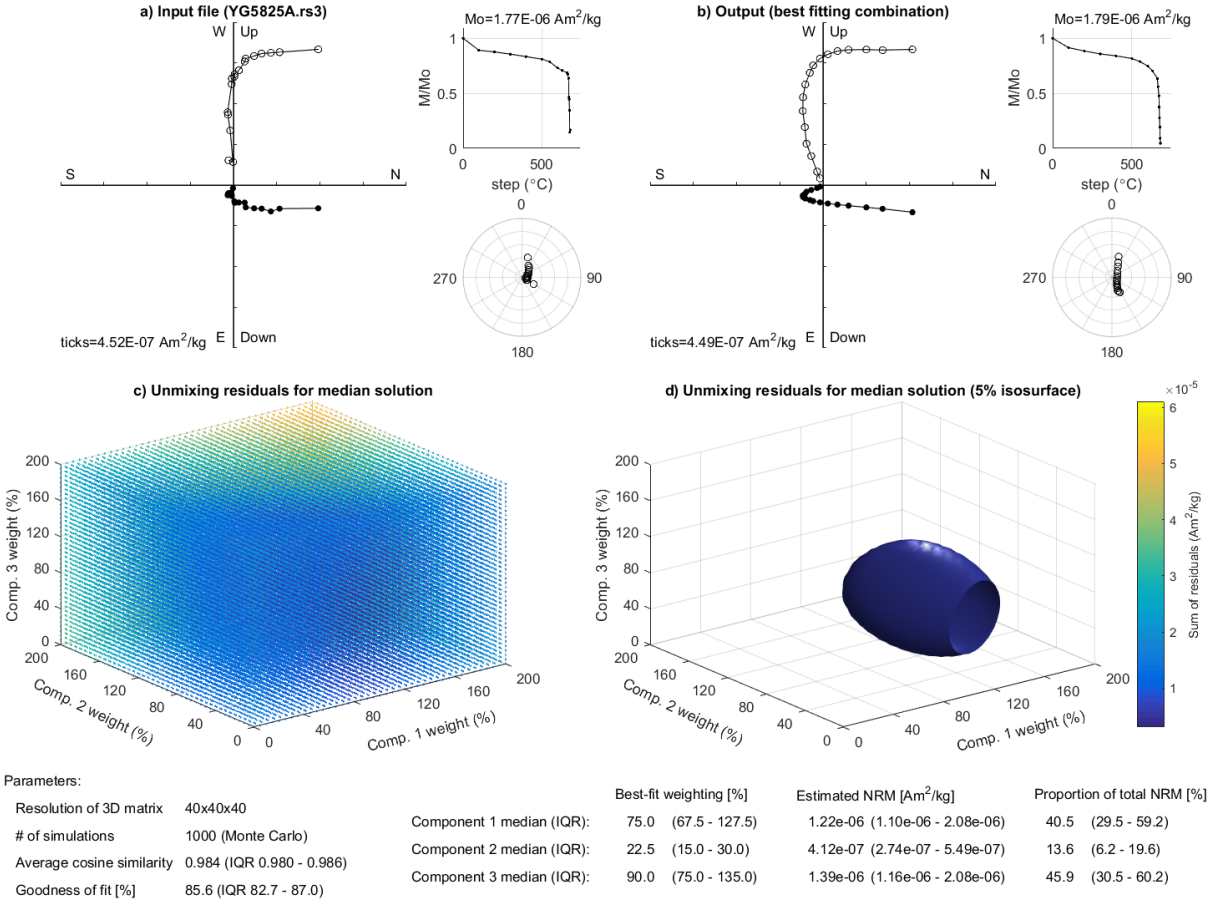

Figure 1.14: Three-component unmixing result for Yangjiaping specimen YG5825A. In this example, the direction of C1 was inverted in order to model the reversed direction of $C1_R$*. The best-fitting model yields a* 75% *weighting for C1,* 22.5% *for C2 and* 90% *for C3, thereby matching* 85.6% *of the input remanence data with an excellent ACS of 0.984.*

constrained, compared to the other examples, as the $C1_R$ direction lies closer to C2 than $C1_N$ is to C2.

Two more examples are shown in Suppl. Fig. A.7 for specimen YG2965B and Suppl. Fig. A.8 for specimen YG6631A, which both had noisy demagnetisation directions upon progressive unblocking. Despite this, the unmixing process resolved the components with high GOFs of 84.6% and 85.1%, respectively.

1.4 Discussion and conclusions

The method presented here for unmixing two or three magnetisation components appears to function well and should be useful for palaeomagnetists trying to unravel complex remanence behaviour in natural materials. The method utilises end-member selection, variable

vector subtraction, and inverse modelling to resolve and quantify contributions for up to three individual magnetic components. It appears to uniquely enable the systematic separation of palaeomagnetic components with non-discrete unblocking or demagnetisation spectra as well as the quantification of component contributions directly from NRM data.

We used stepwise thermal demagnetisation data from red beds suspected of carrying multiple generations of hematite to demonstrate the efficacy of the method. However, the method could be applied to any palaeomagnetic study with stepwise demagnetisation data from materials carrying multiple magnetisation components (e.g. AF demagnetisation of magnetite-bearing rocks). We view this method as a logical step to carry out in combination with PCA to supplement observations from directional analysis. When possible, the results and conclusions made from the inverse modelling should be supported by (or used to inform) further rock magnetic, geochemical and petrographic experiments.

Our approach depends on accurate selection of end-member specimens or components prior to analysis, which may not be possible in all cases and protocols will vary among studies. In cases where end-members can not be identified, the inverse modelling steps could be used in iteration to define the likeliest end-members, e.g., re-running the inverse modelling multiple times and adjusting the input component directions and/or remanence curve shapes with each iteration to maximise the GOF.

The authors are unaware of other approaches that facilitate the systematic quantification of absolute and relative component contributions using directional data alone. Methods exist to unmix and quantify component contributions for isothermal remanent magnetisation (IRM) or anhysteretic remanent magnetisation (ARM) acquisition curves (e.g. Egli, 2004; Gong et al., 2009; Heslop and Dillon, 2007; Maxbauer et al., 2016b), but so far there does not appear to have been any attempt to routinely or systematically unmix component contributions from stepwise demagnetisation data of NRM. Halim et al. (1996) showed that their data could be explained by a combination of synthetic demagnetisation curves, but their method was not systematised for broader use. A method for directly unmixing NRM data is highly desirable as the IRM or ARM acquisition process may magnetise particles which do not necessarily contribute to the NRM.

The scripts herein were run and tested using MATLAB R2016b and R2021b. A link to the scripts and data used in this study can be found below in the Data Availability section. A future goal is to extend the platform to a Jupyter Notebook.

Data availability

MATLAB scripts and data used in this study are available on GitHub at `https://github.com/lmu-magnetism/vector-unmixing`.

Chapter 2

Middle Neoproterozoic (Tonian) polar wander of South China: Paleomagnetism and ID-TIMS U-Pb geochronology of the Laoshanya Formation

Abstract

Paleomagnetic records of middle Neoproterozoic (820-780 Ma) rocks display high amplitude directional variations that lead to large discrepancies in paleogeographic reconstructions. Hypotheses to explain these data include rapid true polar wander, a geomagnetic field geometry that deviates from a predominantly axial dipole field, a hyper-reversing field (>10 reversals/Ma), and/or undiagnosed remagnetization. To test these hypotheses, we collected 1057 oriented cores over a 85 m stratigraphic succession in the Laoshanya Formation (Yangjiaping, Hunan, China). High precision U-Pb dating of two intercalated tuff layers constrain the age of the sediments between 809 and 804 Ma. Thermal demagnetization isolates three magnetization components residing in hematite which are not time-progressive but conflated throughout the section. All samples possess a north and downward directed component in geographic coordinates at temperatures up to 660°C that is ascribed to a Cretaceous overprint. Two components isolated above 660°C reveal distinct directional clusters: one is interpreted as a depositional remanence, while the other appears to be the result of a mid-Paleozoic (460-420 Ma) remagnetization, which is likely widespread throughout South China. The high-temperature directions are subtly dependent on lithology; microscopic and rock magnetic analyses identify multiple generations of hematite that vary in concentration and distinguish the magnetization components. A comparison with other middle Neoproterozoic paleomagnetic studies in the region indicates that the sudden changes in paleomagnetic directions, used elsewhere to support the rapid true polar wander hypothesis (ca. 805 Ma), are better explained by mixtures of primary and remagnetized components, and/or vertical axis rotations.

Reference

This chapter has been submitted and undergone a first round of peer review, and is now in a second round following revisions with JGR: Solid Earth.

Tonti-Filippini, J.A., Robert, B., Muller, E., Paul, A.N., Dellefant, F., Wack, M., Meng., J., Zhao, X., Schaltegger, U., and Gilder, S.A. (in press). Middle Neoproterozoic (Tonian) polar wander of South China: Paleomagnetism and ID-TIMS U-Pb geochronology of the Laoshanya Formation. JGR: Solid Earth, TBD.

Contributions

Funding proposal – BR and SG. Initial fieldwork (2019) – JT, BR, EM, MW, SG and XZ. Supplementary sampling (2021) – JM. Paleomagnetic and rock magnetic measurements – JT with input from SG. Microscopic and mineralogical observations – EM, FD and JT. U-Pb dating – JT and AP under supervision of US. Manuscript – JT with significant input from BR and SG, in consultation with the other authors.

2.1 Background

Magnetic directions preserved in rocks and sediments can be used to estimate past positions of the geomagnetic pole, known as virtual geomagnetic poles (VGPs). A sequence of rocks spanning several million years in time may record progressive changes in VGP position, which can be used to construct an apparent polar wander path (APWP). APWPs represent the combined effect of tectonic plate motion and the net rotation of the mantle and crust with respect to Earth's rotational pole, called true polar wander (Evans, 2002). A key assumption is that Earth's magnetic pole aligns with the geographic (spin) axis, which is known as the geocentric axial dipole (GAD) hypothesis. If the GAD hypothesis is valid, then APWPs can be used to determine past locations of tectonic plates and reconstruct cycles of continental assembly and breakup; globally correlated APWPs can be used to estimate rates of true polar wander.

A key challenge in paleomagnetism is to build accurate APWPs back into the Precambrian (Kodama, 2013). Of particular interest is the Neoproterozoic Era, which saw the end of prolonged environmental stability between 1.8 – 0.8 Ga, a period referred to as the Boring Billion (Roberts, 2013), as well as intermittent episodes of Snowball Earth and extreme greenhouse conditions (Hoffman et al., 1998), culminating in the Cambrian explosion and diversification of complex life after ca. 542 Ma (Marshall, 2006). An explanation of Earth's paleogeography and unique climatic behaviour in the Neoproterozoic is crucial for discerning drivers of long-term climate change and biological evolution. Central to this challenge is unravelling the assembly of the Rodinia supercontinent prior to ca. 900 Ma and its break-up after ca. 750 Ma (Li et al., 2008), but Rodinia's configuration is still debated. Torsvik (2003) described Rodinia as 'a jigsaw puzzle where we must contend with missing and faulty pieces and have misplaced the picture on the box'. The South China Block (SCB) constitutes one of the most enigmatic puzzle pieces, whose Neoproterozoic history has plagued efforts to build a cohesive model of Rodinia (Cawood et al., 2020; Evans et al., 2016; Jing et al., 2021; Park et al., 2021).

Resolving the position and orientation of the SCB in the Neoproterozoic, particularly around 820 – 800 Ma, is complicated by the apparent occurrence of one or two rapid true polar wander (TPW) events which may have rotated Earth's mantle and lithosphere 55 – 90° with respect to the spin axis (e.g., Jing et al., 2020; Li et al., 2004; Niu et al., 2016). Large-scale oscillating TPW events (e.g., Fig. 2.1a), known as inertial interchange true polar wander (IITPW), have been postulated to resolve discordant paleomagnetic directions from other continents and are linked to dramatic global environmental change observed around the same time (Kirschvink et al., 1997). Sudden directional changes observed in South China have been compared with paleomagnetic observations from Svalbard (Maloof et al., 2006), and speculatively correlated with the onset of a global negative carbon isotope anomaly, the Bitter Springs Stage, known as the Bitter Springs TPW hypothesis (Swanson-Hysell et al., 2012).

The debate over South China's position in Rodinia is convolved with the Bitter Springs TPW hypothesis, as paleomagnetic data from the SCB undergo rapid paleolatitude variations between 820 and 780 Ma. Various reconstructions of Rodinia place the SCB in a

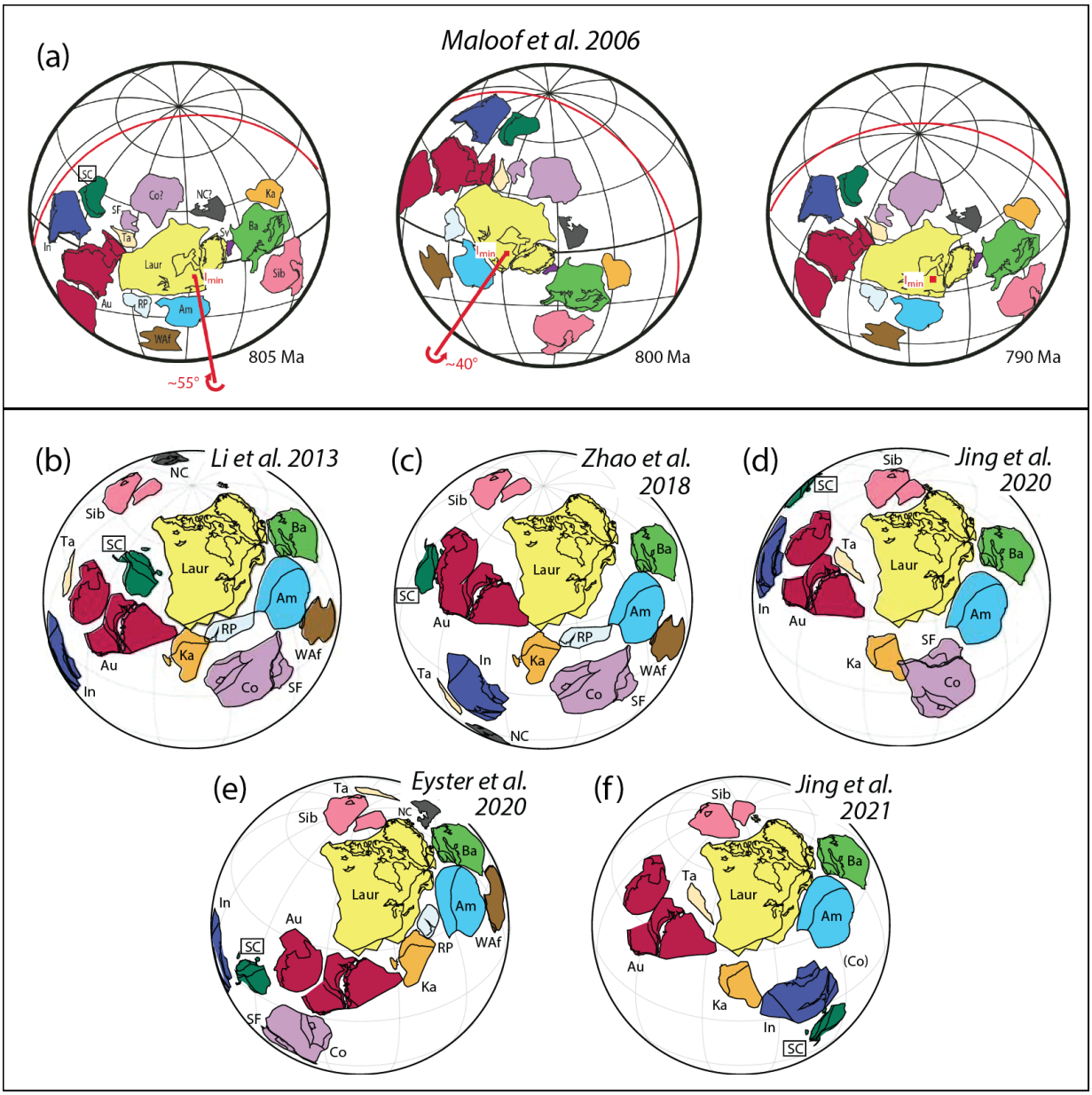

Figure 2.1: (a) Paleogeographic reconstructions of Rodinia during a hypothesized rapid true polar wander (TPW) event between 805 and 790 Ma; the TPW rotation axis (I_{min}) is marked in red (after Maloof et al., 2006). (b-f) Proposed reconstructions of Rodinia with Laurentia fixed in present North American coordinates, modified from Evans (2021). South China occupies completely different positions in each reconstruction (see Eyster et al., 2020; Jing et al., 2021, 2020; Li et al., 2013; Zhao et al., 2018). Am = Amazonia, Au = Australian cratons including Mawsonland, Ba = Baltica, Co = Congo, In = India, Ka = Kalahari, Laur = Laurentia, NC = North China, RP = Rio Plata, SC = South China, SF = Sao Francisco, Sib = Siberia, Sv = Svalbard, Ta = Tarim, WAf = West Africa.

central, marginal or completely isolated position (Fig. 2.1b). Classic 'missing link' models place the SCB at a low latitude between Laurentia and Australia (e.g., Li et al., 2008), while other models such as SWEAT (Southwest US – East Antarctica) place the SCB adjacent to India and/or NW Australia, allowing for a direct fit between Australia and Laurentia (Yao et al., 2019). It is also possible that South China was entirely disconnected from Rodinia and occupied a position near the north pole (e.g., Park et al., 2021). Increasingly, models appear to challenge a SWEAT configuration in the Neoproterozoic, although more and more studies suggest that Australia, India and South China were geographically close through the late Cryogenian to Ediacaran (Zhang et al., 2021, and references therein).

Maloof et al. (2006) and Swanson-Hysell et al. (2012) suggested that testing of the Bitter Springs TPW hypothesis necessitates robust paleomagnetic and geochronologic studies of continuous sedimentary sequences from several cratons. If the rapid TPW hypothesis is valid, then all strata that span the Bitter Springs Stage [ca. 810 – 800 Ma; Halverson et al. (2022)], should show similar excursions in their isotopic and paleomagnetic signals. Resolving these discordant paleomagnetic directions, currently observed only in Svalbard and South China, calls for integrative studies and is an issue of 'major geodynamic significance' (Evans et al., 2016). Raub et al. (2015) notes that the TPW events hypothesized by Maloof et al. (2006) are not directly dated so cannot be precisely correlated with data from South China. This allows for considerable flexibility in paleogeographic models around 800 Ma, so the TPW hypothesis and the precise configuration of Rodinia 'must await better constraints' (Raub et al., 2015).

Other plausible explanations for South China's discordant paleomagnetic data include rapid tectonic plate motion or non-dipolar to hyper-reversing geomagnetic fields driven by nucleation of Earth's inner core (e.g., Driscoll, 2016). Peculiar APWPs could also be an artefact of undiagnosed remagnetization. For example, Zhang and Piper (1997) warned that South China experienced several episodes of tectonic reworking and suffered extensive sub-tropical weathering, thereby highlighting challenges to paleomagnetism, especially going far back in time. Indeed, numerous studies from South China are based on red sedimentary rocks that have complicated magnetization histories; hence, caution is required when interpreting paleomagnetic signals in red beds.

The Yangjiaping (Hunan Province, China) area has a fairly complete geologic record from the Neoproterozoic through the Paleozoic, including Marinoan tillites and cap carbonates (Macouin et al., 2004). Below the tillites lie the Laoshanya Formation red beds, which were previously dated at Yangjiaping to 809 ± 16 Ma (Yin et al., 2003). There, we collected 1057 paleomagnetic cores in a 85 metre-thick section, freshly exposed along a river, as well as 14 cores in the underlying Lengjiaxi Group. We present a paleomagnetic study of those samples, combined with rock magnetic, mineralogical and microscopic analyses, as well as ID-TIMS U-Pb zircon geochronology of intercalated tuffs, in order to shed light on Neoproterozoic geomagnetic field behaviour and the paleogeography of South China around 820 – 800 Ma.

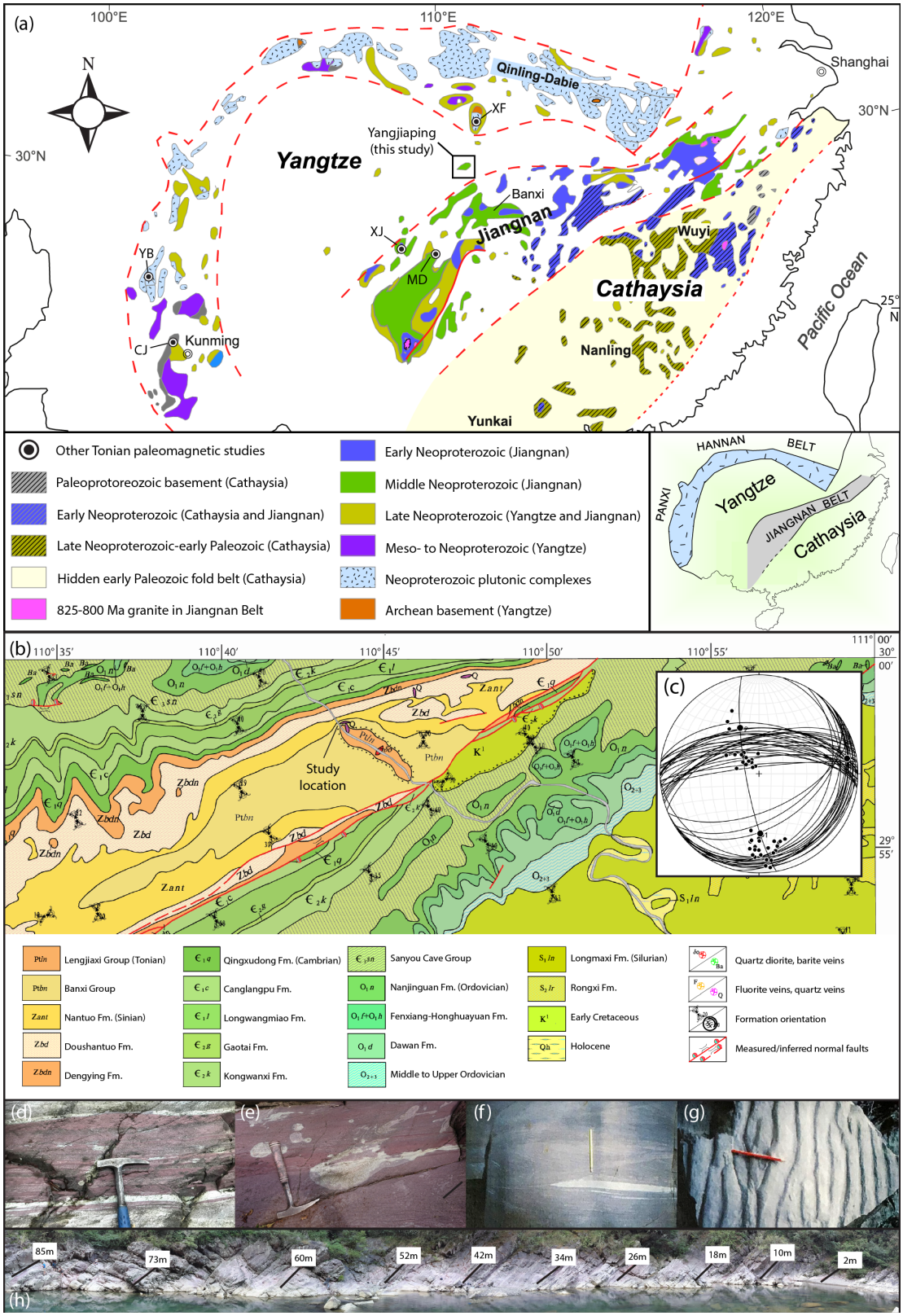

Figure 2.2: (Caption next page.)

Figure 2.2: (Previous page.) (a) Simplified regional map highlighting the Neoproterozoic in South China (after Cawood et al., 2018). Table B.1 lists the Tonian studies (black circles with initials). (b) Geological map of the Yangjiaping area, northwest Hunan (after Li et al., 2017). (c) Measured bedding strikes and dips in the area indicates near-cylindrical folding, with a slightly plunging (11°) axis trending 80°. (d-g) Field photos of the Laoshanya Formation showing (d) alternating green-grey and purple-red sandstones, (e) leaching of the red beds (whitish color) that cuts across bedding, (f) cross-bedding, and (g) ripple marks. (h) Composite photo of sampled section with stratigraphic heights.

2.2 Geological setting

2.2.1 Nanhua rift basin

The South China Block (SCB) consists of two major tectonic elements, the Yangtze craton to the northwest and the Cathaysia block to the southeast (Fig. 2.2a), which probably sutured around 1000 – 820 Ma (Cawood et al., 2013), an event referred to as the Jiangnan or Sibao orogeny. There is still controversy over the timing of their amalgamation, but it is generally accepted that the two blocks formed the SCB when they collided along the Jiangshan-Shaoxing suture zone (Wang et al., 2015, and references therein). After ∼820 Ma, during the hypothesized breakup of Rodinia, the Nanhua rift basin developed along the suture zone (Zhang et al., 2008), which accumulated sediments through the Neoproterozoic to Early Paleozoic (Charvet, 2013). Several rifting phases likely occurred in the basin as indicated by bimodal magmatism ca. 830 – 820 Ma; the lower sequences are dominated by volcaniclastic sedimentary rocks that are interpreted to be continental rift deposits (Wang and Li, 2003).

Rifting terminated in the Nanhua basin in the Late Ordovician to Early Silurian (460 – 400 Ma), perhaps due to inversion of the basin in response to continental convergence (Xu et al., 2016), an enigmatic episode known by several names including the Caledonian (Wang et al., 2007), Wuyi-Yunkai (Li et al., 2010) and Kwangsian (Zheng et al., 2020) orogenic event. We refer to this episode as the Wuyi-Yunkai Orogeny. An explanation for the geodynamic processes that triggered the Wuyi-Yunkai Orogeny is a persistent problem, although an angular unconformity between South China's pre-Devonian and Devonian strata is widespread (Charvet, 2013). Mid-Paleozoic metamorphic and magmatic rocks, as well as evidence of folding and thrusting, are found throughout the Jiangnan orogen and Cathaysia block, but the tectonic response to the Wuyi-Yunkai Orogeny is not well understood within the Yangtze craton (Zheng et al., 2020).

2.2.2 Banxi Group

One of the key rifting successions in the Nanhua basin is the Banxi Group siliclastic sequence (ca. 820 – 730 Ma) that crops out towards the south-eastern edge of the Yangtze craton and is widely exposed in Hunan Province (Zhang et al., 2008). The Banxi Group

is thought to have formed in an intra-continental rift environment and is characterized by thick sedimentary successions and bi-modal magmatism (Cawood et al., 2018). The Banxi Group in Hunan Province has been considered equivalent to the Danzhou Group in northern Guangxi Province (Zhang, 1998) and the Xiajiang Group in eastern Guizhou Province (Lan et al., 2015; Park et al., 2021); however, the age of the base of the Danzhou Group is poorly constrained (Song et al., 2017).

Around the study area, the Banxi Group overlies the Lengjiaxi Group with an angular unconformity (the Wuling unconformity), which crops out throughout the orogen and is broadly constrained as 830 – 813 Ma (Li et al., 2022a). In north-central Hunan, the Cangshuipu Group volcanics were emplaced between the Banxi and Lengjiaxi groups. These volcanics were dated at 824 – 814 Ma (Wang et al., 2003; Zhang et al., 2015b), which provide an additional constraint on the lower age of the Banxi Group. The Banxi Group consists of the Madiyi Formation in the lower part and the Wuqiangxi in the upper (Zhang et al., 2008). The Xihuangshan disconformity (800 – 779 Ma) separates the Madiyi and Wuqiangxi Formations (Li et al., 2022a), referred to elsewhere as the Zhangjiawan and Xieshuihe Formations, respectively (Wang et al., 2003).

The Madiyi Formation crops out across Hunan and is thought to have formed in a shallow marine, oxidizing environment. In northwest Hunan, the formation comprises alternating sequences of distinct dark purple-red mudstones and green sandstones (Fig. 2.2h). A regional study of detrital zircons in the Madiyi Formation yielded age peaks (lower limits) at ~ 808 Ma in the lowermost part, and $803-800$ Ma in the uppermost part (Li et al., 2022a). The Madiyi Formation is characterized as relatively Fe_2O_3-rich and may act as a geochemical barrier in the region: $\sim 80\%$ of the gold deposits in northwest Hunan are hosted in the Madiyi Formation (Yang and Blum, 1999). The Laoshanya Formation is synonymous with the Madiyi Formation in Yangjiaping (Yin et al., 2003), although recent work suggested the Madiyi Formation may be slightly younger (Park et al., 2021; Xian et al., 2020; Zhang et al., 2015b). We use Laoshanya to refer specifically to the outcrop in Yangjiaping, and Madiyi to refer to the wider formation, as our dating shows them to be the same age (Section 2.4.1).

2.2.3 Yangjiaping section

The Yangjiaping section lies in the northwestern Nanhua rift basin (Fig. 2.2b) (Song et al., 2017; Zhang et al., 2000). Yangjiaping is an important landmark for the Precambrian geology of South China and was selected as a 'candidate stratotype section' for the Nanhua system (Yin et al., 2003). At Yangjiaping, the Laoshanya Formation is 148 metres thick (Yin et al., 2004) and presents a continuous sequence of alternating purple-red and green-grey sandstones and siltstones (Fig. 2.2d). For comparison, Madiyi in the southeast part of the basin may be 3500 metres thick (Zhang et al., 2008). The Laoshanya Formation is well-preserved and shows evidence of a shallow marine, near-shore or tidal environment, with cross-bedding (Fig. 2.2f) and ripple marks (Fig. 2.2g). Some beds contain sub-vertical quartz and calcite veinlets up to several centimetres wide. White to pale green 'mottling' is ubiquitous (Fig. 2.2e), often cross-cutting the purple beds, which may be evidence of

localized leaching of iron by secondary fluids (Parry et al., 2004).

The Laoshanya Formation is conformably overlain by the Xiushuihe (Wuqiangxi) Formation (Fig. 2.3), dated at 758 ± 23 Ma by the Sensitive High Resolution Ion Microprobe (SHRIMP) method (Yin et al., 2003). Twelve metres below the Xiushuihe/Laoshanya contact lies a tuff whose SHRIMP zircon U-Pb date constrained the upper age of the Laoshanya Formation to 809 ± 16 Ma (Yin et al., 2003). The Laoshanya Formation (strike/dip = 255°/58°) uncomformably overlies the Lengjiaxi Group (258°/87°), dated elsewhere at 860 − 835 Ma (Zhang et al., 2015b). A five metre thick conglomerate distinguishes the unconformity, which demarcates the base of our section. SHRIMP U-Pb dating of laminated tuff from the underlying Lengjiaxi Group in Yangjiaping yielded 845 ± 12 Ma (Sun et al., 2012).

The Doushantuo Formation (599 ± 4 Ma) in Yangjiaping yielded a single-polarity magnetization that passed a fold test and was interpreted to be primary, indicating a low-latitude position for South China in the Ediacaran (Macouin et al., 2004). However, Zhang et al. (2015a) remarked that the formation does not contain the pattern of reversals common for the Ediacaran elsewhere; the paleopole lies close to other Early Cambrian and Silurian poles for South China; and the positive fold test implies only that the magnetization is pre-folding and not necessarily primary. Macouin et al. (2004) recognized the similarity of their pole to Early Silurian poles, although they considered the loop in South China's APWP between the Early Vendian and Silurian to be a robust feature and not an artefact of remagnetization. More detailed rock magnetic data suggested an episode of magnetite dissolution during early diagenesis (Macouin et al., 2012).

South China was shaped by large-scale Mesozoic deformation in response to the collision of the North and South China blocks that ended by the Late Jurassic (Gilder and Courtillot, 1997; Yan et al., 2003). This collision likely produced the folding at Yangjiaping seen in Fig. 2.2(b) (Gilder et al., 1999). Yang et al. (2021) identified angular unconformities between Middle Triassic and Jurassic strata, and between Cretaceous and pre-Cretaceous strata 20 – 40 km south of Yangjiaping. At Yangjiaping, the Laoshanya Formation through the Late Ordovician Wufeng Formation [442 ± 8 Ma (Xie et al., 2012)] have consistent strikes 250 − 280° and dips 55 − 70°, suggesting a lack of significant deformation until at least the end of the Ordovician. Similarly, no angular unconformity exists between the Neoproterozoic Danzhou Group and Ordovician sedimentary rocks in northern Guangxi, ∼500 km to the south (Li et al., 2022b).

2.3 Methods and equipment

2.3.1 Sampling campaigns

We collected paleomagnetic samples in September 2019 along a river at Yangjiaping (Fig. 2.2b) (Shimen County, Hunan Province) opposite the J01 County Road (29.970°E, 110.732°N). 1057 oriented cores, 2.5 cm in diameter, were drilled over a stratigraphic thickness of 85 m starting at the base of the Laoshanya Formation (Fig. 2.3), with a

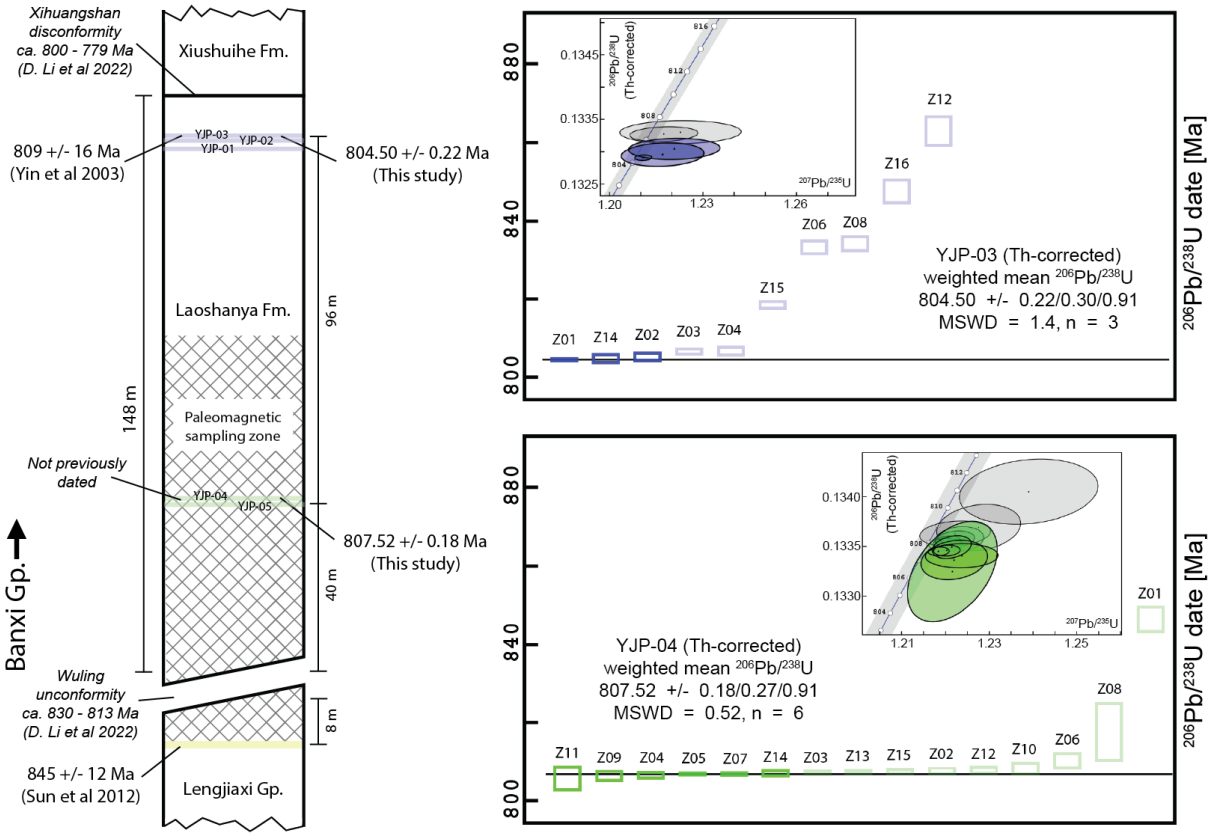

Figure 2.3: Geochronology of the Laoshanya Formation in Yangjiaping with locations of interbedded tuffs (blue, green and yellow stripes). A five metre thick conglomerate marks the base of our section, below which 14 cores were sampled in the Lengjiaxi Group. Previously published dates are shown on the left side of the column; our new dates (YJP-03 and YJP-04) are shown on the right. Coloured rectangles indicate Th-corrected $^{206}Pb/^{238}U$ dates for individual zircons with 2σ analytical uncertainty; transparent rectangles indicate results excluded from weighted means. Corresponding $^{206}Pb/^{238}U$ – $^{207}Pb/^{235}U$ concordia diagrams are inset.

nominal spacing of 5-10 cm; occasionally we drilled 4 or 5 cores in the same horizon with each sample separated along strike by 10's to 100's of cm. An additional 14 cores were drilled over a stratigraphic thickness of 5 m at the top of the underlying Lengjiaxi Group (below the conglomerate). All cores were oriented with sun (when possible) and magnetic compasses. The median magnetic anomaly from the sun compass was -3.4 ± 0.6° (n = 269), indistinguishable from that expected (-3.7°) from the IGRF2020 model (Alken et al., 2021) at Yangjiaping; all compass azimuths were corrected accordingly. In August 2021, five ∼2 kg samples were collected from suspected volcanic tuff horizons within the Yangjiaping section for U-Pb dating (Fig. 2.3).

2.3.2 U-Pb geochronology

High precision U-Pb zircon dating was performed using chemical abrasion - isotope dilution - thermal ionization mass spectrometry (CA-ID-TIMS) at the University of Geneva. Mineral separation involved crushing and milling bulk samples to <300 µm, followed by concentration on a Wilfley table, Frantz magnetic separator and heavy liquids (methylene iodide, density 3.32 g/ml). Crack and inclusion-free zircon crystals were hand-picked under a binocular microscope, thermally annealed at 900°C for 48 hours, and then partially dissolved in concentrated hydrofluoric acid (HF) at 210°C for 12 hours in a Parr^{TM} bomb vessel (Widmann et al., 2019). The partially dissolved grains were then extracted and washed in 6N HCl in 3 ml Savillex beakers overnight (min. 12 h) at 80°C. Individual zircons were washed 4x with 7N HNO_3 in 3 ml Savillex beakers placed in an ultrasonic bath. Samples were then transferred into 200 µl Savillex microcapsules, mixed with 1-2 drops of EARTHTIME ^{202}Pb-^{205}Pb-^{233}U-^{235}U (ET2535) tracer solution (Condon et al., 2015; McLean et al., 2015) and dissolved with 2-3 drops of concentrated HF in Parr^{TM} digestion vessels at 210°C for 48 hours. After dissolution, samples were dried at 120°C, re-dissolved in 3N HCl, and then U and Pb were separated using anion exchange column chemistry. Chemical preparation was carried out in a class 100 clean-air facility. U and Pb were loaded together on outgassed, zone-refined, Re filaments with a silica-gel/phosphoric acid emitter solution (Gerstenberger and Haase, 1997), and measured on either a Thermo Scientific Triton TIMS or an IsotopX Phoenix TIMS.

The measured isotopic ratios were corrected for interferences of $^{238}U^{18}O^{16}O$ on $^{235}U^{16}O_2$ using a $^{18}O/^{16}O$ composition of 0.00205 based on repeat measurements of the U500 standard. Mass fractionation of U was corrected using a double isotope tracer with a $^{235}U/^{233}U$ of 0.99506 ± 0.00005 (1σ). The Pb blank isotopic composition is $^{206}Pb/^{204}Pb$ = 17.84 ± 0.37 (1σ), $^{207}Pb/^{204}Pb$ = 15.25 ± 0.33 (1σ) and $^{208}Pb/^{204}Pb$ = 37.05 ± 0.90 (1σ), based on total procedural blank measurements. Repeat analyses of the ET100 solution ($^{206}Pb/^{238}U$ date: 100.173 ± 0.003 Ma; Schaltegger et al., 2021) yielded a value of 100.1678 ± 0.0046 Ma (MSWD = 3.2, n = 32/40). All zircon $^{206}Pb/^{238}U$ dates were corrected for ^{230}Th-^{238}U disequilibrium using a Th/U_{magma} of 3.5 ± 1.0.

To determine the U-Pb age of each tuff we take the youngest cluster of ≥ 3 analyses, assuming the zircons crystallised until the time of eruption and all Pb-loss is mitigated by the chemical abrasion procedure, in line with previous U-Pb ID-TIMS studies which show

that youngest date clusters are generally a reliable measure for eruption age (e.g., Edward et al., 2023; Schaltegger et al., 2015). Older dates are assumed to be from recycled zircons or associated with inherited cores, wall rock contamination, and/or prolonged growth in magma chambers. We report weighted mean U-Pb age uncertainties at the 2σ level in the format A±X/Y/Z, where A = weighted mean age, X = analytical uncertainty, Y = combined analytical and tracer uncertainty, and Z = combined analytical, tracer and decay constant uncertainty (Schoene et al., 2006).

2.3.3 Paleomagnetism

Paleomagnetic samples were measured at the Paleomagnetic Laboratory, Ludwig-Maximilians-Universität (LMU-Munich). Cores were cut into 2.2 cm high cylindrical specimens using a non-magnetic saw. Specimens were thermally demagnetized in a magnetically-shielded, paleomagnetic oven with an accuracy of ± 1°C (Volk, 2016). Remanent magnetizations were measured using a 2G Enterprises superconducting rock magnetometer via the automated SushiBar system (Wack and Gilder, 2012). Before treatment and after each heating step, bulk susceptibilities were measured at room temperature with a Bartington MS2 susceptibility meter. Repeat measurements on a subset of specimens were measured with an Agico JR6 spinner magnetometer to check for consistency. 22 specimens underwent stepwise alternating field (AF) demagnetization up to 90 mT prior to thermal demagnetization, which generally removed <10% of the natural remanent magnetization (NRM) so was discontinued. All paleomagnetic measurements were made inside a 90 m^3 magnetically shielded room with an average residual field <500 nT.

2.3.4 Rock magnetism

Based on the paleomagnetic experiments, select samples were subjected to a suite of rock magnetic investigations. Samples were crushed into powder using a porcelain mortar (unsieved). Hysteresis parameters and isothermal remanent magnetization (IRM) acquisition curves in applied fields up to 1.8 T were measured with a Princeton Measurements Corporation MicroMag 3900 vibrating sample magnetometer (VSM) at LMU-Munich. Low temperature experiments were performed on the same instrument down to 77 K with a liquid nitrogen cryostat. Thermal susceptibility curves were measured up to 700°C in air using a Agico MFK1-FA Kappabridge with a CS-4 furnace at the University of Oslo. Anisotropy of magnetic susceptibility (AMS) measurements on 99 non-demagnetized core specimens were carried out with an Agico MFK1-FA Kappabridge at the University of Tübingen, with a peak field intensity of 200 A/m and an operating frequency of 976 Hz. Anisotropy of anhysteretic magnetic remanence (AMR) measurements were made on the same 99 specimens using the SushiBar at LMU-Munich with a peak AF field of 90 mT and a DC bias field of 0.1 mT (Wack and Gilder, 2012).

2.3.5 Mineralogical and microscopic analyses

25 samples were selected for mineralogical analyses. Polished thin sections were first observed using transmitted and reflected light microscopy at LMU-Munich. Scanning electron microscopy (SEM) analyses were performed with a Hitachi SU5000 Schottky Field-Emission Gun (FEG) SEM (LMU-Munich), and on core slices polished to 0.5 µm with a Zeiss Ultra55 FEG SEM at the Institut de Minéralogie, Physique des Matériaux et de Cosmochimie (Paris). Backscattered secondary electron (BSE) images were acquired using an angle selective backscattered detector with accelerating voltages of 15 - 20 kV, and working distances of 7.5 - 10 mm. Elemental compositions were determined by energy dispersive X-ray spectrometry (EDXS) using an QUANTAX EDS detector after copper calibration. Semi-quantification of the spectra was achieved using the ESPRIT software package (Bruker) and the phi-rho-z method.

Results from EDXS elemental composition data obtained by SEM were cross-checked with XRD measurements to more confidently identify the mineralogy. Four ∼10 g core samples were finely ground and homogenized in an agate mortar for X-ray diffraction (XRD) at the Institut de physique du globe de Paris (IPGP, France). XRD analyses on the powders were performed using a Panalytical Xpert Pro transmission diffractometer with a copper anode operated at 45 kV and 40 mA and a slit of 0.5° at a 240 mm radius. The 2θ scan was performed in continuous mode from 4° to 90° (2θ) with steps of 0.0001°. Peak identification was performed using pattern search on the X-ray diffraction database of reference spectra Crystallography Open Database (`http://www.crystallography.net`).

2.4 Results and observations

2.4.1 U-Pb geochronology

Samples YJP-01, YJP-02 and YJP-03 lie 12 m below the top of the Laoshanya Formation (Fig. 2.3); YJP-01 and YJP-03 are 1.8 m apart. Samples YJP-04 and YJP-05 (0.6 m apart) lie 40 m above the base of the formation, near the middle of the paleomagnetic sampling zone, 96 m below YJP-01. Song et al. (2017) measured a stratigraphic thickness of 184 m for the Laoshanya Formation in Yangjiaping (perhaps along the road); our measurements on the riverside outcrop match the stratigraphic thickness of 148 m obtained by Yin et al. (2004).

Analyses of 44 individual zircons from the upper three samples (YJP-01 to YJP-03) yielded dates predominantly between 863 and 804 Ma based on Th-corrected $^{206}Pb/^{238}U$ ratios, with minor (n<4) clusters at 1.0, 1.7, 2.0 and 2.4 Ga. Sample YJP-03 yielded the youngest age plateau at 804.50 ± 0.22/0.30/0.91 Ma (MSWD = 1.4, n = 3), which we interpret as the depositional age for this part of the section. YJP-01 and YJP-02 contained many subhedral or rounded zircons that yielded dates between 861 and 807 Ma, with no distinct plateau, which we interpret as inherited or recycled.

We analyzed 29 zircons from the lower sample group. Sample YJP-04 contained hundreds of pristine euhedral zircons and yielded the youngest age plateau at 807.52 ±

0.18/0.27/0.91 Ma (MSWD = 0.52, n = 6), which is interpreted as the depositional age. YJP-05 contained large subhedral zircons that yielded scattered dates between 1015 and 818 Ma, with an age plateau at 818.91 ± 0.18/0.27/0.92 Ma (MSWD = 0.45, n = 3). Given that YJP-05 is situated only 0.6 m below YJP-04, we consider it unlikely that this is a true depositional age as it implies a hiatus of 11.4 Myr which is not supported by field observations. Th/U_{zircon} ratios for YJP-05 are also lower (<0.75) than those of YJP-03 and YJP-04 (generally 0.9 to 1.2), suggesting a different provenance or metamorphic overgrowth, and increased likelihood of inheritance. Moreover, a depositional age >814 Ma would be superpositionally inconsistent with the inferred ages of the underlying Wuling unconformity and the Cangshuipu volcanics.

Assuming no significant depositional hiatuses exist, these results yield an accumulation rate of 32 ± 4 m/Myr (or 3.2 ± 0.4 cm/kyr) for the Laoshanya Formation (with analytical uncertainty only). Using linear extrapolation (Blaauw and Christeny, 2011), our findings suggest that the Laoshanya Formation was deposited between 808.7 [median, 95% range = 809.6-808.0] and 804.2 [median, 95% range = 804.7-803.5] Ma (Fig. B.4), and can be broadly correlated with the lower Madiyi Formation and upper Xiajiang Group. Our results agree well with the regional compilation of Li et al. (2022a) who reported age peaks in detrital zircons at ∼ 808 Ma for lower Madiyi and 803 to 800 Ma for upper Madiyi. The age of 807.52 ± 0.18/0.27/0.91 Ma in the middle (40 m height) of the paleomagnetic sampling zone is assigned to the paleopole in the following sections.

2.4.2 Paleomagnetic results

1188 specimens were thermally demagnetized up to 680°C with progressive decreases in temperature steps from 100 to 2°C (Fig. 2.4). Many specimens demonstrated erratic demagnetization behaviour above 660°C which was accompanied by a large (tenfold) increase in bulk susceptibility, indicating alteration. Three coherent components (A, B and C) were identified using principal component analysis (Kirschvink, 1980), as described below and shown in Fig. 2.4 with summaries in Fig. 2.5 and Table 2.1. Specimens often appeared to contain variable concentrations of all three components, which could be resolved and quantified with vector unmixing analyses (Tonti-Filippini and Gilder, 2023). Some samples also contained a spurious component which demagnetized below 100-200°C and generally aligned with the present day field; this is interpreted to be a viscous remanent magnetization (see Butler, 1992, Chapter 3) and not considered further.

Components A, B and C

1016 specimens (86%) contained a coherent north and down (in situ coordinates) directed component that unblocked mostly between 100 and 660 °C (Figs. 2.4a and d). This component is referred to as component A and is ubiquitously present in both the Laoshanya Formation (n = 1002) and the Lengjiaxi Group (n = 14). Component A often occurs in combination with a higher temperature component (B or C), although in ca. 6% of the

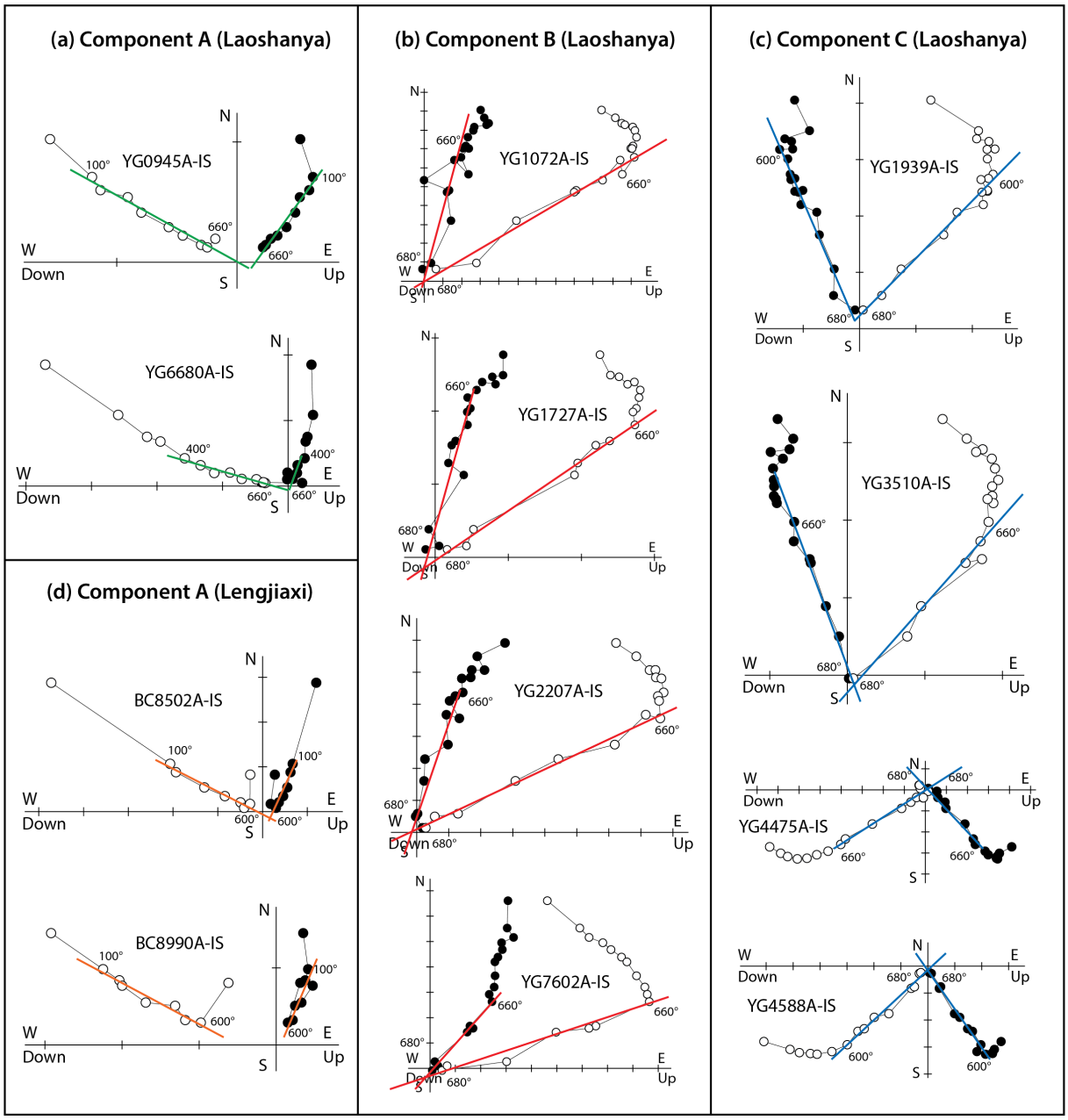

Figure 2.4: Zijderveld (1967) diagrams of representative samples (in geographic coordinates) from the three component groups (A-C) from the Yangjiaping section displayed with best-fitting ChRM components not forced to the origin. All tick marks are 10^{-3} A/m. In (a), only component A is present, removed below 660 °C. Specimens from component B (b) group generally unblock to the origin between 660 and 680 °C with single-polarity directions, after removal of component A. Component C (c) unblocks to the origin between 660 and 680 °C and has dual-polarity ChRM directions after removal of component A. (d) Specimens from the Lengjiaxi Group (below the conglomerate) contain component A, but not B or C.

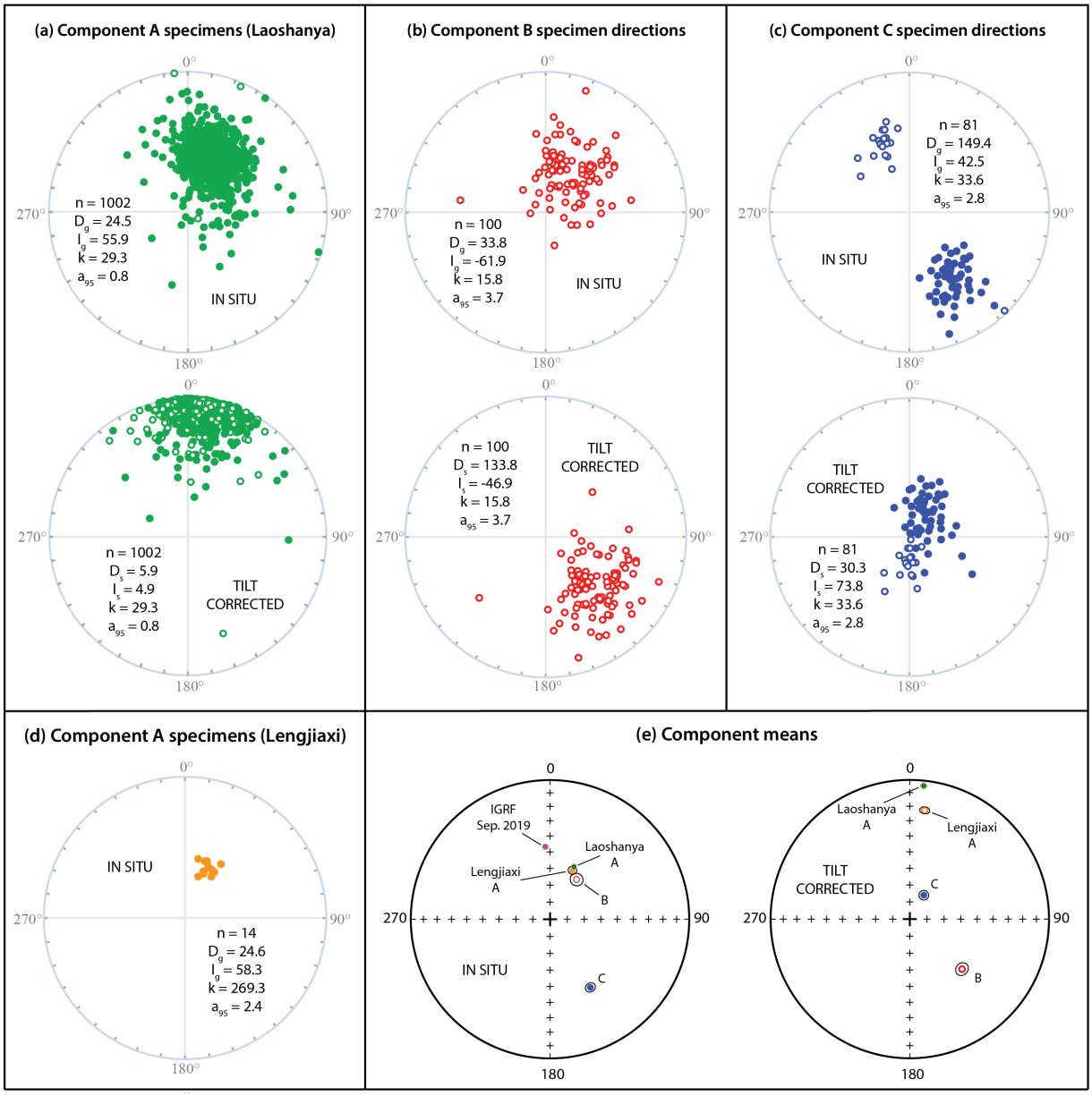

Figure 2.5: Stereonet plots of component A-C paleomagnetic directions in geographic (in situ) and stratigraphic (tilt-corrected) coordinates. Filled circles are lower hemisphere, open circles upper hemisphere. (a-c) Components A and B have a single-polarity while component C has dual-polarities. (d) Specimens from the Lengjiaxi Group only contain component A, indistinguishable to that from the Laoshanya Formation in geographic coordinates. (e) Specimen mean directions for components A, B and C are distinguishable from the expected IGRF direction (Alken et al., 2021). α_{95} ellipses are shown in black; α_{95} for Laoshanya A component is smaller than the point indicating the direction.

Table 2.1: Summary of paleomagnetic results from Yangjiaping (29.970 °N, 110.732 °E). n = number of specimens. D and I are declination and inclination in (g) geographic (in situ) and (s) stratigraphic (tilt-corrected) coordinates (°). κ and α_{95} are the precision parameter and 95% confidence ellipse (Fisher, 1953). Pos./neg. rev. test = positive or negative reversal test after McFadden and McElhinny (1990). A, B and C refer to the magnetization component.

Name	n	D_g	I_g	D_s	I_s	κ	α_{95}	Comments
Lengjiaxi Gp.								Strike/dip = 258/87
Lengjiaxi A	14	24.6	58.3	7.8	-22.2	269.3	2.4	Neg. fold test
Laoshanya Fm.								Strike/dip = 255/58
Laoshanya A	1002	24.5	55.9	5.9	4.1	29.3	0.8	Neg. fold test
Laoshanya B	100	33.8	-61.9	133.8	-46.9	15.8	3.7	
Laoshanya C	81	149.4	42.5	30.3	73.8	33.6	2.8	Neg. rev. test
Laoshanya C*	44	150.9	43.4	25.4	74.1	48.3	3.1	Pos. 'B' rev. test

*Filtered for specimens that decay linearly to the origin and have MAD $< 10°$ (Fig. B.3).

specimens, it is the sole magnetization component. A fold test is negative at 99% confidence limits (McElhinny, 1964), indicating component A was acquired after folding.

181 specimens (15%) displayed coherent demagnetization behaviour from 660 to 680 °C that decays to the origin on Zijderveld diagrams (Figs. 2.4b and c). The high-temperature directions form two clusters on a stereonet (Figs. 2.5b and c), which are referred to as components B (n = 100) and C (n = 81). Component B consists of single-polarity, southeast and up directions in tilt-corrected (stratigraphic, s) coordinates (Fig. 2.5b). Despite spanning 85 metres of section, component B directions are present only in one polarity.

Component C (n = 81) comprises dual-polarity directions with steep inclinations in tilt corrected coordinates; 62 samples have positive inclinations and 19 negative (Fig. 2.5c). A reversal test (McFadden and McElhinny, 1990) is negative at the 95% confidence level. However, the reversal test is positive (B classification) if the specimens are filtered for the directions that decay linearly to the origin with maximum angular deviations (MAD) $\leq 10°$ (n = 44, Fig. B.3). Large MAD values likely arise from unresolved overlapping components (B+C). Components B and C were only found in the Laoshanya Formation so no fold test could be performed at the local level. Below, we show the results of a regional fold test, which is negative for component B and positive for component C.

Sedimentology

Median bed thickness defines three distinct parts (Fig. 2.6a). In the lowermost 20 m, median bed thickness ranges from 0.10 to 0.25 m for sandstones and 0.05 to 0.10 m for siltstones. This part preserves abundant ripple marks, suggesting a shallow, tidal or near-shore environment. Between 20 and 54 m, the median thickness of the sandstone beds

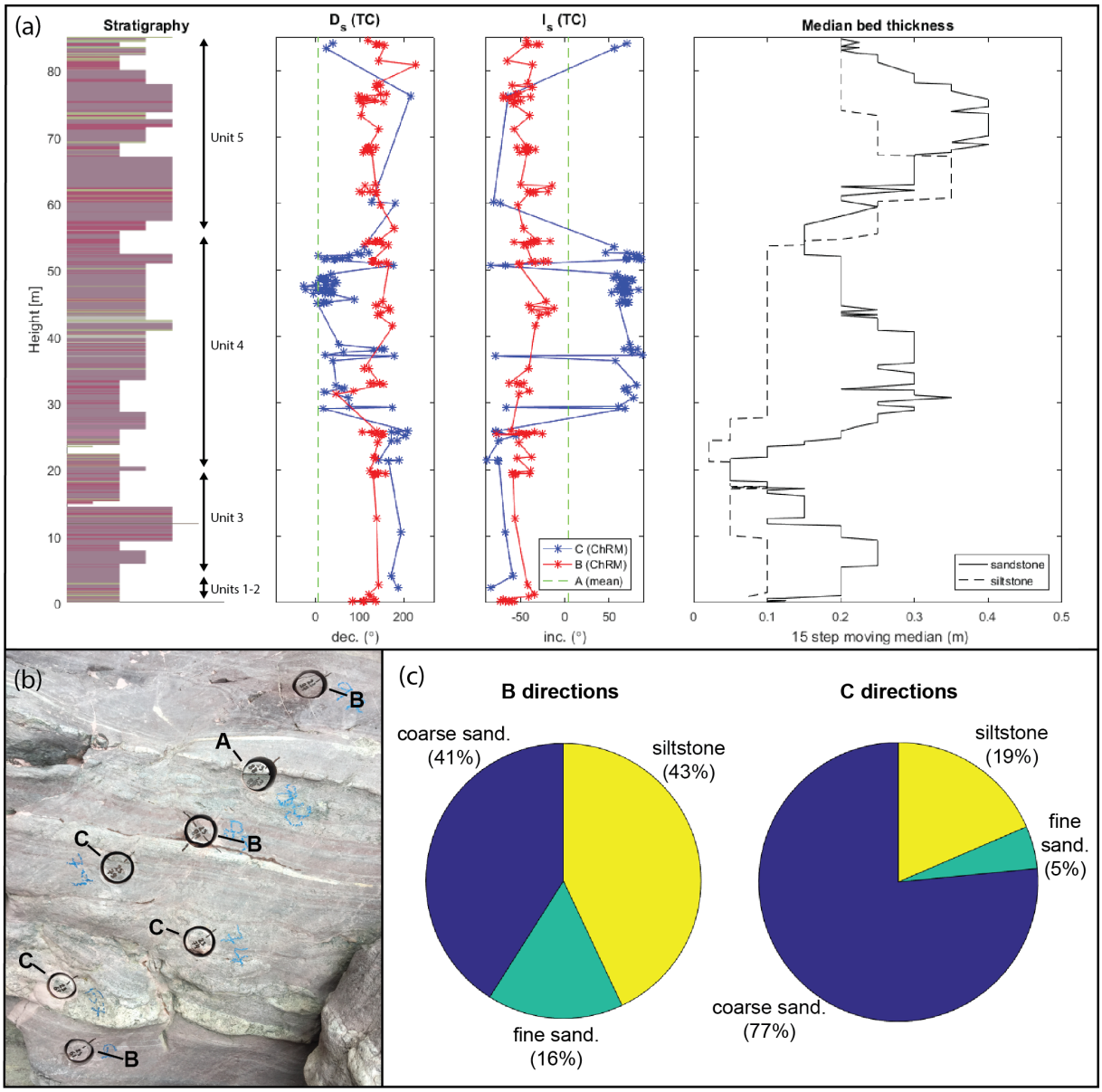

Figure 2.6: Lithological characteristics of paleomagnetic directions. (a) Graphical representation of the paleomagnetic section (Laoshanya Formation, Yangjiaping), with stratigraphic units identified by Yin et al. (2004). The section is shown alongside the paleomagnetic results (D_s and I_s = declination/inclination in stratigraphic [tilt corrected] coordinates) and median bed thickness by lithology. (b) Field photo of interbedded siltstone/sandstone that contain the components A-C as indicated. (c) Component C was more frequently identified in the coarse sandstone beds, while component B was found more in siltstones and fine-grained sandstones.

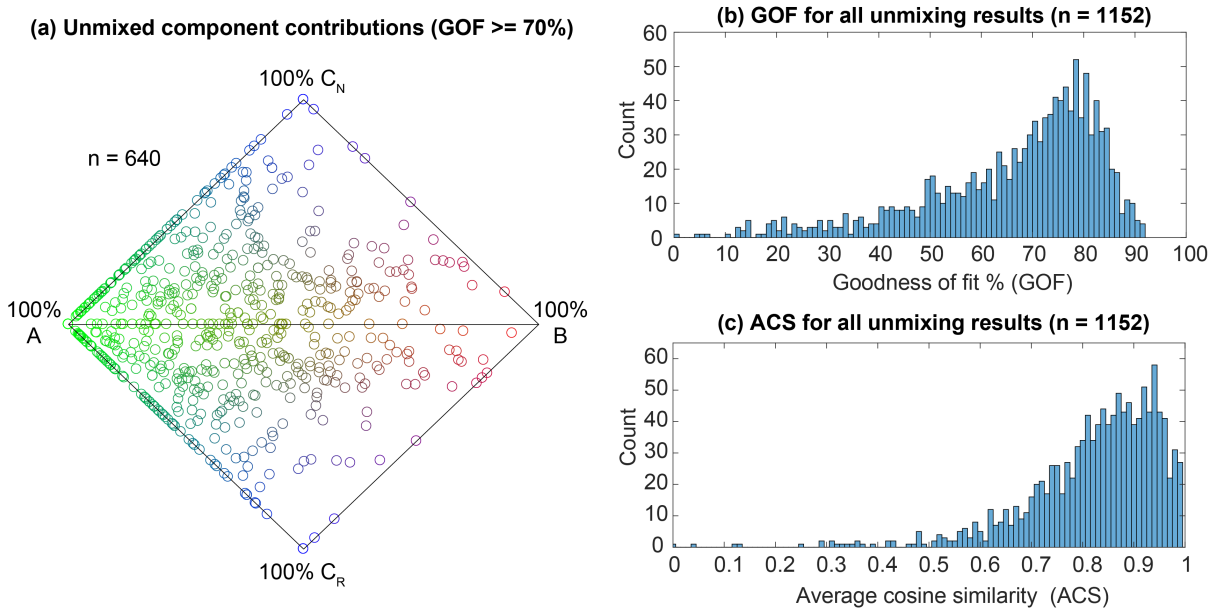

Figure 2.7: Results of vector unmixing analyses. (a) Specimen unmixing results with goodness of fit (GOF) ≥ 70 % (n = 640), shaded by component contribution where green = A, red = B and blue = C. Results are shown on a double ternary plot as a proportion of total NRM, unmixed using median component curves derived in Tonti-Filippini and Gilder (2023), representing estimated combinations of components A, B and C_N (positive inclinations) or C_R (negative inclinations). Distributions of (b) GOF and (c) average cosine similarity (ACS) for all Laoshanya unmixing results (n = 1152).

increases up to 0.35 m. This part contains graded bedding and some cross-bedding, indicating more energetic deposition. Median thickness increases towards the top of the section (54-85 m) for both siltstones (up to 0.35 m) and sandstones (up to 0.4 m) which could indicate a more stable, perhaps deeper, depositional environment; cross-bedding and ripple marks are absent. These three parts compare well with stratigraphic units 1-5 described by Yin et al. (2004).

We compared the paleomagnetic results against the stratigraphic log (Fig. 2.6a) to test the correlation between lithology and magnetization components. Specimens containing component B arise mainly in the siltstone and fine sandstone beds (59%), with 41% taken from coarse sandstone beds (Figs. 2.6b and c). 77% of the specimens having component C come from coarse sandstones, while 23% come from finer sediments. Component C appears more frequently in the middle part (20-54 m), while component B is more abundant in the bottom (0-20 m) and top (54-85 m) parts. The highest density of specimens containing component C occurs in the thick sandstone beds between 45 and 50 m. This is not an artefact of sampling density as the spacing between specimens was kept constant at 5-10 cm throughout the section.

Vector unmixing

To quantify component contributions to the NRM, we performed vector unmixing analyses (Tonti-Filippini and Gilder, 2023) on 1152 specimens from the Laoshanya Formation (Fig. 2.7). A goodness of fit (GOF) $\geq$ 70% was achieved for 640 specimens using the mean component directions from Table 2.1 and the median demagnetization curves derived by Tonti-Filippini and Gilder (2023), i.e., demagnetization data for more than half the specimens could be accurately modelled by superimposed contributions from components A, B and/or C. In the following sections, we grouped the specimens by their dominant component, i.e., the estimated component contribution must be at least $\sim$ 40 % of the total NRM to qualify for that component group. However, 98% of the specimens contain some combination of two or three of the components.

2.4.3 Rock magnetic results

Thermal remanence curves for group A samples gradually decay between 100 and 660 °C (Figs. 2.4a and d), consistent with fine-grained or pigmentary hematite (Collinson, 1974). Those in groups B and C unblock in a narrow range between 660 and 680 °C (Figs. 2.4b and c), consistent with crystalline hematite (Özdemir and Dunlop, 2002, 2005). To further characterize remanence carriers, we carried out rock magnetic experiments on fresh specimens from cores chosen to best represent component groups A, B, and C.

High temperature experiments

Fig. 2.8 shows representative magnetic susceptibility vs. temperature curves (9 out of 25 measured). All samples exhibit a rapid decline in susceptibility between 660 and 700 °C, indicative of the Néel temperature in hematite. Another commonality, although variable in magnitude, is the existence of a phase with a Curie temperature around 100–200 °C that is non-reversible upon cooling. This could be indicative of titanium-rich titanohematite, titanomagnetite or goethite.

The thermal susceptibility curves can be divided into three categories:

1. Samples in the first category (Figs. 2.8a-b, d-e and g) have reversible behavior with a Hopkinson peak around 660 °C, characteristic of single-domain (SD) hematite grains (Dunlop, 1974).

2. Samples in the second category (Figs. 2.8c and h-i) have irreversible behavior upon cooling below 600 °C, with a new or enhanced Hopkinson peak around 560 °C, near the Curie temperature of magnetite. This is indicative of the creation of SD magnetite at high temperatures, which also explains the increase in bulk susceptibility above 600 °C observed in the thermal demagnetization experiments; the susceptibility of magnetite is several orders of magnitude higher than hematite (O'Reilly, 1984).

3. The third category (Fig. 2.8f) has steep slopes in the cooling curves around 560-600 °C, indicative of magnetite. However, the susceptibility of the cooling curves may be

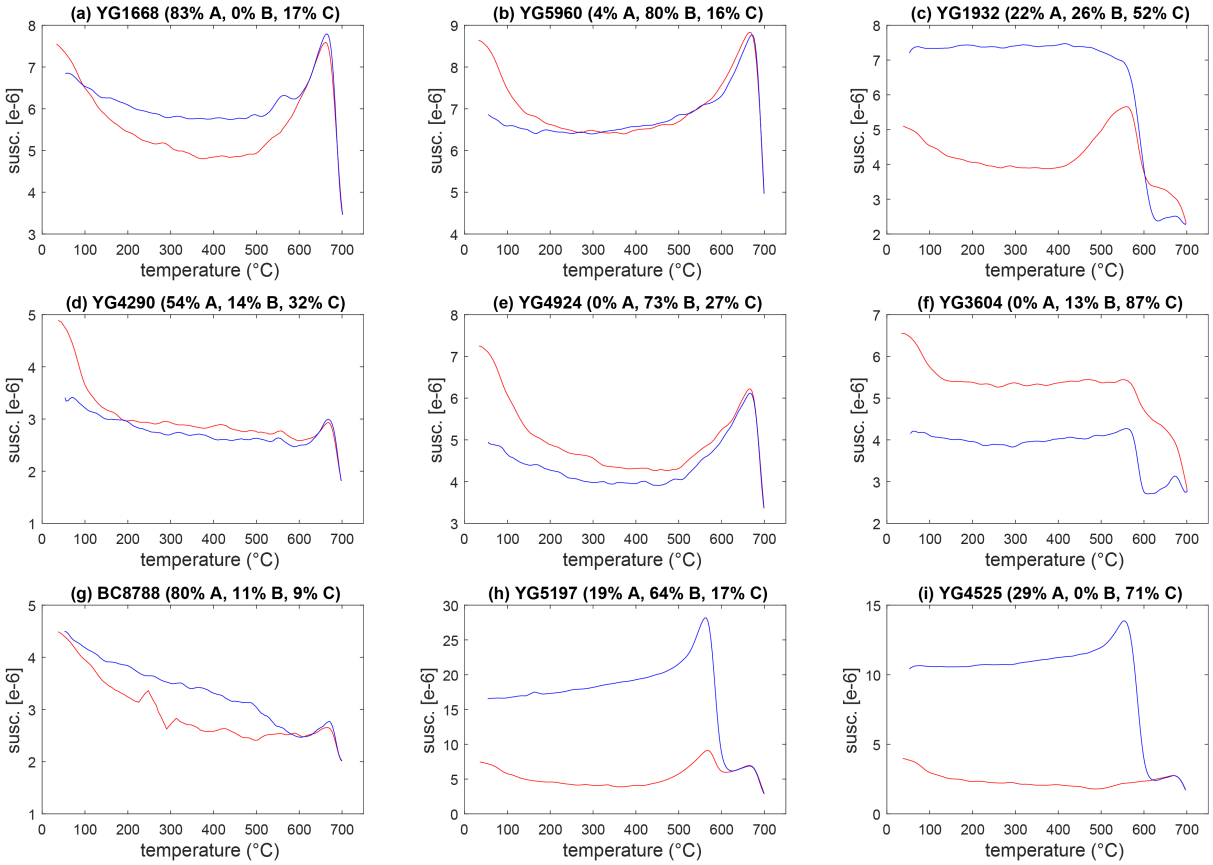

Figure 2.8: Susceptibility (not mass-normalized) vs. temperature curves for each component group between 20 and 700 °C (in air) (red lines indicate heating, blue lines cooling). Component contributions estimated by vector unmixing analysis are shown in the subtitles. Most specimens show a Hopkinson peak around 660 °C, with rapid decay up to 700 °C, consistent with SD hematite. The Hopkinson peaks appear more pronounced in specimens with a dominant (> 50%) component A (a, d, and g) or B (b, e, and h), compared to those with a dominant component C (c, f, and i). Some specimens, e.g., (c), (e) and (i), exhibit a Hopkinson peak upon cooling around 560 °C, likely due to the creation of magnetite during heating. All samples have a phase with a Curie temperature below 150 °C that is destroyed by heating, which may indicate the presence of high-Ti titanohematite, titanomagnetite or goethite.

lower than the heating curves, suggesting some pre-existing magnetite was oxidized to hematite. At higher temperature, new magnetite was created, sometimes in lower concentration when the cooling curve is below the heating curve.

Low temperature experiments

Low temperature experiments were performed on the VSM using a liquid nitrogen cryostat (Fig. B.1). A magnetizing field of 1.8 T was applied at room temperature (293 K) then switched off. Magnetic remanence was then measured in a null field down to 100 K and then upon warming to room temperature at a rate of 0.25 °/s. Pure hematite typically shows a drop in remanence through the Morin transition (Özdemir et al., 2008) around ∼250 K; however, none of the Yangjiaping samples displayed either a measurable Morin transition or a Verwey transition (characteristic of magnetite), at least until 100 K (note that temperature stability of the cryostat decreases approaching 100 K). Dekkers and Linssen (1989) observed similar low temperature behaviour in natural hematite and suggested that impurities (e.g., adsorbed silica) might suppress the Morin transition. Small amounts of Ti (e.g., 1 wt.%) can also suppress the Morin transition (Özdemir et al., 2008), so the absence of a measurable Morin transition is not uncommon. We found no evidence for a Verwey transition in the ca. 100-123 K range indicative of magnetite.

Hysteresis (VSM)

Hysteresis parameters were determined for 22 samples up to 1.5 T (Figs. 2.9a-b), although hematite can require >10 T to fully saturate (Rochette et al., 2005). Linear corrections (75-90% to 1.5 T) were subtracted to account for paramagnetic contributions. The corrected hysteresis loops for samples with dominant A or B components (Figs. 2.9c-d) are broad and do not saturate, consistent with single domain (SD) hematite (Özdemir and Dunlop, 2014). Samples in group C (Fig. 2.9e) show narrow wasp-waisted curves, indicating populations of grains with contrasting coercivity. These wasp-waisted loops are similar to multidomain (MD) hematite behaviour observed by Özdemir and Dunlop (2014). Compositional variations in titanohematite grains could also explain wasp-waisted hysteresis behaviour (Roberts et al., 1995), as can mixtures of magnetite and hematite.

Samples in group C have bulk coercivities (Hc) an order of magnitude lower and saturation magnetizations (Ms) $2-3$ times higher than those in groups A and B (Fig. 2.9f). Values of Hc between 10 and 100 mT in group C imply hematite grain sizes of 10-300 µm (Özdemir and Dunlop, 2014), while values between 300 and 600 mT (for groups A and B) imply smaller hematite grain sizes, on the order of d = 0.1-3.0 µm. However, we note that these numbers pertain to very crystalline hematite, and natural hematite can have a maximum in coercivity at a much smaller grain size. Kletetschka and Wasilewski (2002) estimated the SD to MD grain size transition at 100 µm for hematite, suggesting that the group C hematite is more MD rich than groups A and B. As would also be expected for MD hematite, most samples from group C have only minor or non-existent Hopkinson peaks (Fig. 2.8).

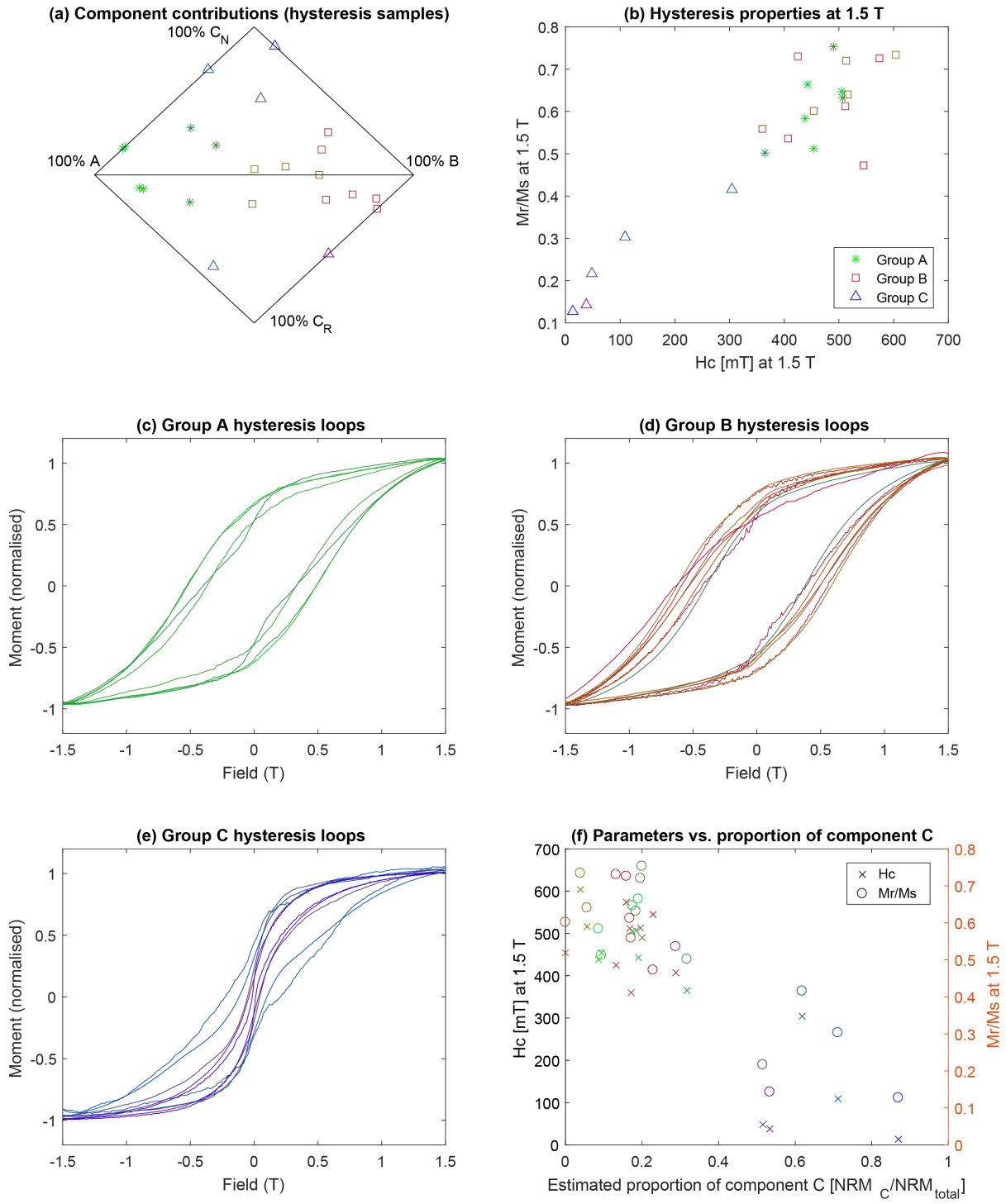

Figure 2.9: (Caption next page.)

Figure 2.9: (Previous page.) High field experiments. (a) Vector unmixing results for samples used in the hysteresis experiments, with dominant components indicated by blue triangles (C), red squares (B) and green stars (A). The same colour shading is preserved in b-f. (b) Samples with higher Mr/Ms ratios have higher coercive forces (Hc). Lower Hc values can indicate larger hematite grain sizes (Özdemir and Dunlop, 2014), and/or mixtures of magnetite with hematite. (c-e) Room temperature hysteresis curves for specimens from component groups A, B, and C. Groups A and B have wide curves consistent with single domain hematite. Group C has wasp-waisted loops, indicating populations of grains with distinctly different coercivity spectra. (f) Mr/Ms and Hc values (at 1.5 T) correlate negatively with the proportion of component C.

Anisotropy (AMS and AMR)

We measured the anisotropy of magnetic susceptibility (AMS) on 99 non-demagnetized core specimens (Figs. 2.10a-e and B.2a-c). Anisotropy degrees (P) were <1.1, with maximum axes (K1) trending 235° on average in the horizontal plane (tilt-corrected coordinates). Intermediate (K2) and minimum (K3) axes spread over a NW-SE great circle, with some clustering in the vertical and horizontal planes. AMS directions are not markedly different among the three groups, although group C has a more pronounced tectonic fabric (Fig. 2.10c). The intermediate tectonic fabrics are typical of sedimentary rocks in thrust-and-fold belts (Saint-Bezar et al., 2002). However, the K2-K3 plane implies a 325° shortening direction (235°-trending fold axis), which differs from the measured strike of our section (255°) by 20° (Fig. 2.10e).

Anisotropy of magnetic remanence (AMR) was measured on the same 99 specimens (Figs. 2.10f-j and B.2d-f) using the refinement method of Wack (2023). Groups A-C have similar fabrics as AMS, although more scattered (Figs. 2.10f-h). P values are generally <1.2 with mean principal axis directions are similar to those for AMS, with maximum axes (M1) declinations trending 227°, compared to 235° for AMS (K1). Considering all results together, 29 specimens have P >1.2 (mean P = 1.12 for n = 99). Mean M1 axes for those (P >1.2) specimens trend 245°, 20° clockwise relative to the total population (Figs. 2.10i-j). The more anisotropic specimens occur in groups A and B, suggesting they absorbed more of the tectonic stress that produced the deformation in Yangjiaping. This is not surprising since finer-grained sediments (Section 2.4.2) with higher clay contents typically absorb more tectonic strain (Kodama, 2012).

2.4.4 Mineralogy and microscopy

X-ray diffraction peaks are dominated by quartz (25-34 %), albite (12-20 %), muscovite (42-54 %) and chlorite (2-5 %) (e.g., Fig. B.5). Hematite is the main iron-bearing mineral whose concentration varies from 2 to 6 wt.%. Chlorites also contain up to 4 % Fe (EDXS data). SEM observations and EDXS analyses accord well with the XRD data. SEM images show that fine-grained micas and silicates (chemically consistent with muscovite and chlo-

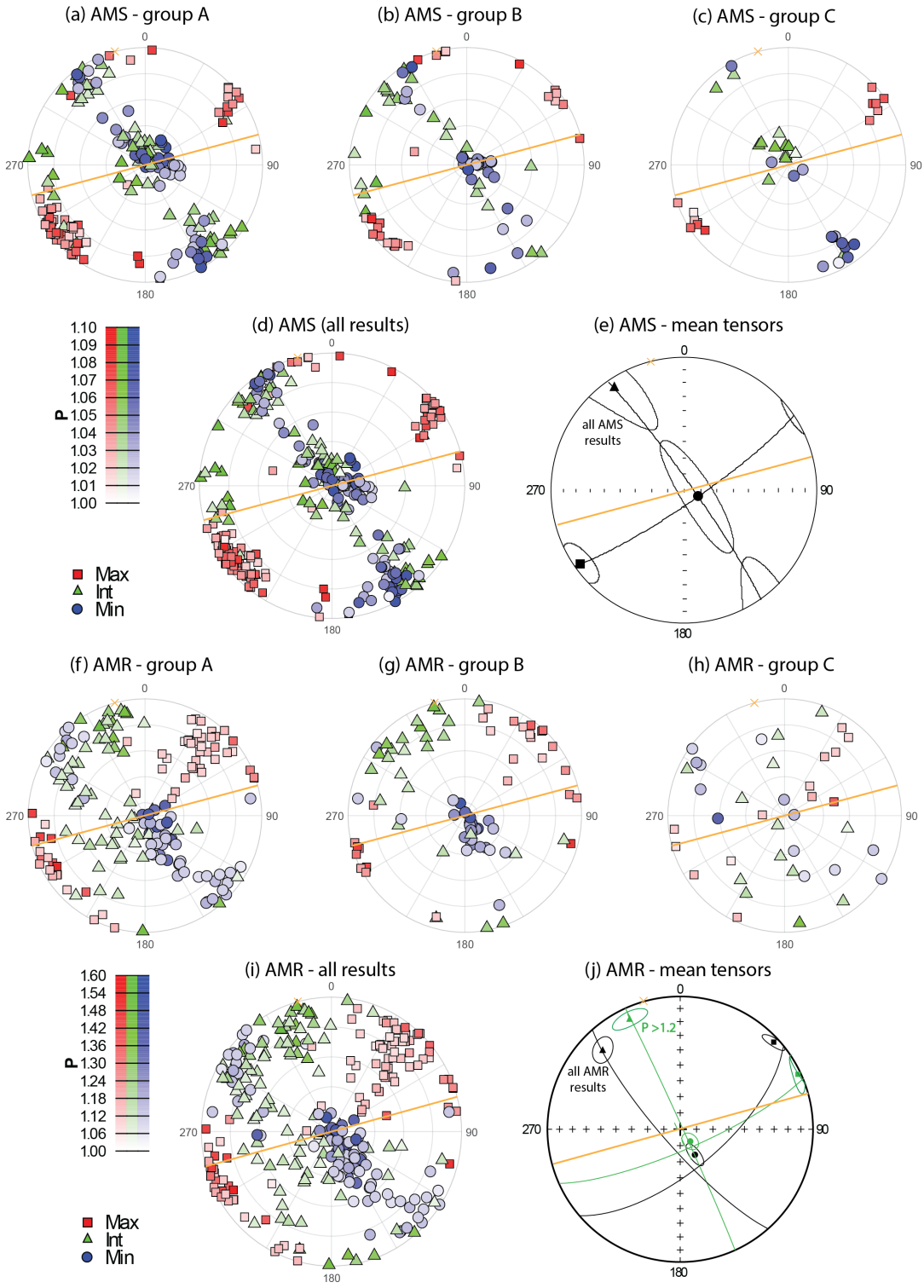

Figure 2.10: (Caption next page.)

Figure 2.10: (Previous page.) Stereonet plots of principal axes directions for anisotropy of magnetic susceptibility (AMS) and anisotropy of magnetic remanence (AMR) measured in Laoshanya samples. The strike in Yangjiaping is shown in orange. Symbols are shaded by anisotropy degree (P). Note the different scales between AMS and AMR. (a-c) AMS principal axes directions of the three component groups in tilt-corrected coordinates. Groups A and B have sedimentary fabrics (K3, the minor axis, lies perpendicular to the bedding plane) with varying degrees of a tectonic overprint. Maximum anisotropy axes (K1) lie approximately parallel to strike, while some K3 axes are rotated toward the horizontal along a great circle trending perpendicular to strike. Group C records a strong tectonic fabric, with horizontal K3 directions and K2 (intermediate axis) directions perpendicular to bedding. (d) AMS principal axes directions for all samples. (e) The mean K2-K3 plane defines a shortening direction oriented 325°. (f-h) AMR principal axes directions for groups A and B are generally compatible with those from AMS. Group C has mostly incoherent fabrics. (i) Taken together, the most anisotropic samples have AMR K1 directions that parallel more closely to the fold axis direction than AMS. (j) Mean AMR tensors divided by shape anisotropy. Samples with P >1.2 are more consistent with the regionally-defined compression axis (345°) – all results (black) = 316°, for P >1.2 (green) = 335°.

rite) cluster around coarse grains of quartz and alkaline feldspar. Accessory minerals, such as vermicularite, calcite, apatite, zircon, monazite and rutile, were chemically characterized by EDXS.

SEM images (Fig. 2.11) show abundant hematite in all samples. Fine, needle-like hematite flakes, generally < 1 µm, are ubiquitous but more dominant in group A samples (Figs. 2.11a-f). Samples from groups B and C contain large (30–100 µm), Ti-rich hematite and martite (hematite pseudomorphic after magnetite) grains showing trellis textures of exsolution typical of Ti-magnetite and/or (hemo-)ilmenites (Figs. 2.11g-r). Samples from group B also show abundant 1–2 µm hematite platelets scattered throughout the matrix, or in dense clusters, which presumably replaced and/or oxidized Fe-rich grains (Figs. 2.11g-k). Larger grains in group B appear to be more leached, with empty Ti-rich (rutile) lattices left behind, surrounded by hematite platelets (Fig. 2.11l). Group C samples generally contain fewer hematite flakes in the matrix than the other sample groups (Figs. 2.11m-p), consistent with minimal Fe remobilization. Overall, these observations suggest there was greater Fe remobilization in groups A and B than in group C.

2.5 Interpretation and discussion

Our experimental results offer several insights into the nature of the remanent magnetizations in the Laoshanya Formation:

1. SEM analyses show that group C samples contain abundant detrital (ca. 30 – 100 µm) Ti-rich hematite grains indicative of MD grain sizes, consistent with an igneous

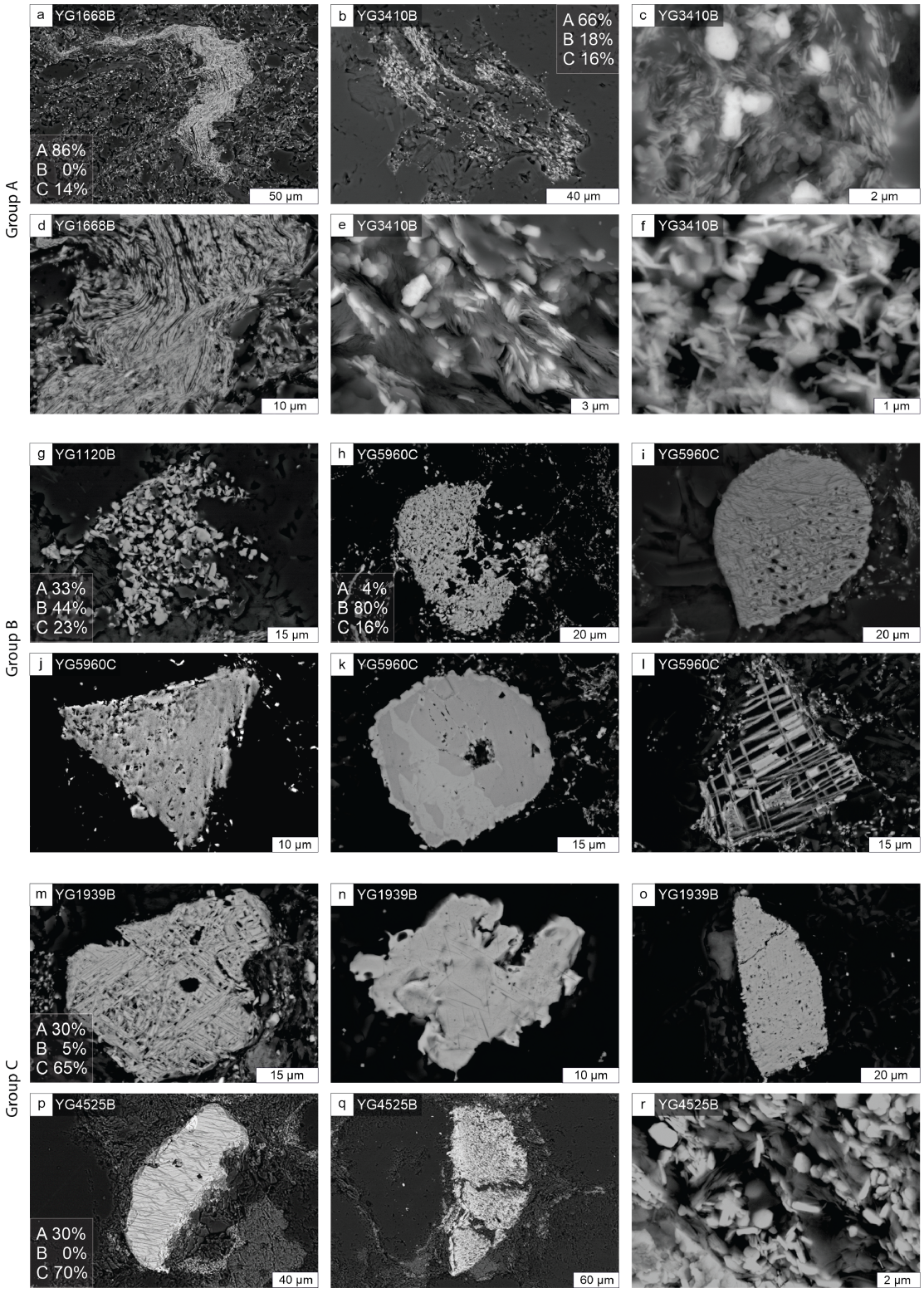

Figure 2.11: (Caption next page.)

Figure 2.11: (Previous page) SEM images indicating component proportions estimated by vector unmixing analyses. (a-f) Specimens dominated by component A show pervasive Fe remobilization and fine, needle-like hematite flakes, generally <1 μm. (g-l) Component B-rich specimens contain dense clusters of hematite platelets ca. 1–2 μm which appear to have formed in situ, perhaps from the leaching of Ti-rich trellis structures. (m-r) Specimens with a high proportion of component C generally have fewer fine-grained hematite flakes and platelets, and are dominated by large (30-100 μm) Ti-rich hematite and martite grains with exsolution features typical of converted Ti-magnetite and/or (hemo-)ilmenite.

or metamorphic source (Basu and Molinaroli, 1989), and therefore a primary/detrital remanence (DRM). These samples also contain a reduced presence of < 1-2 μm (SD-sized) hematite flakes relative to the samples from groups A and B. Hysteresis curves for group C samples appear wasp-waisted, indicating distinct magnetic populations or dominantly MD grains. Thermal-susceptibility curves for group C also showed minor to non-existent Hopkinson peaks, consistent with MD behaviour.

2. Hysteresis parameters suggest that samples from groups A and B are dominated by SD hematite. Thermal-susceptibility curves for groups A and B also show distinct Hopkinson peaks. This is supported by SEM observations of abundant sub-micron hematite particles in these samples, consistent with Fe remobilization and secondary fluid circulation, potentially from the dissolution of Fe-rich minerals (Walker et al., 1981). The fact that the SEM images show the SD hematites to be secondary products supports a chemical formation, and hence, a CRM.

3. AMR fabrics indicate group A and B specimens may have absorbed more tectonic stress, with higher anisotropy and an inferred strain axis rotated 20° relative to the other component groups, consistent with higher clay content/more fine-grained material.

2.5.1 Components in the Laoshanya Formation

Of the three magnetization components isolated in this study, component A fails the fold test between the Laoshanya and Lengjiaxi formations. The corresponding direction at 0% unfolding is D = 24.5°, I = 55.9°, α_{95} = 0.8°, composed solely of normal polarity, similar to a widespread overprint component found throughout South China, originally described by Kent et al. (1987). The corresponding pole at lat = 68.6°N, lon = 176.7°E, dp/dm = 0.8°/1.1° is near-sided with respect to Cretaceous reference poles for South China. The unfolding path of component A intersects the Cretaceous poles of Huang et al. (2018) at 10-20% unfolding; however, the reference pole is based mostly on sedimentary rocks, which can be affected by inclination shallowing. Given that the overprint is a CRM and the reference poles are based mostly on continental sediments with DRM, one would expect a CRM to be immune from inclination shallowing, as found by Meng et al. (2022). Hence, we

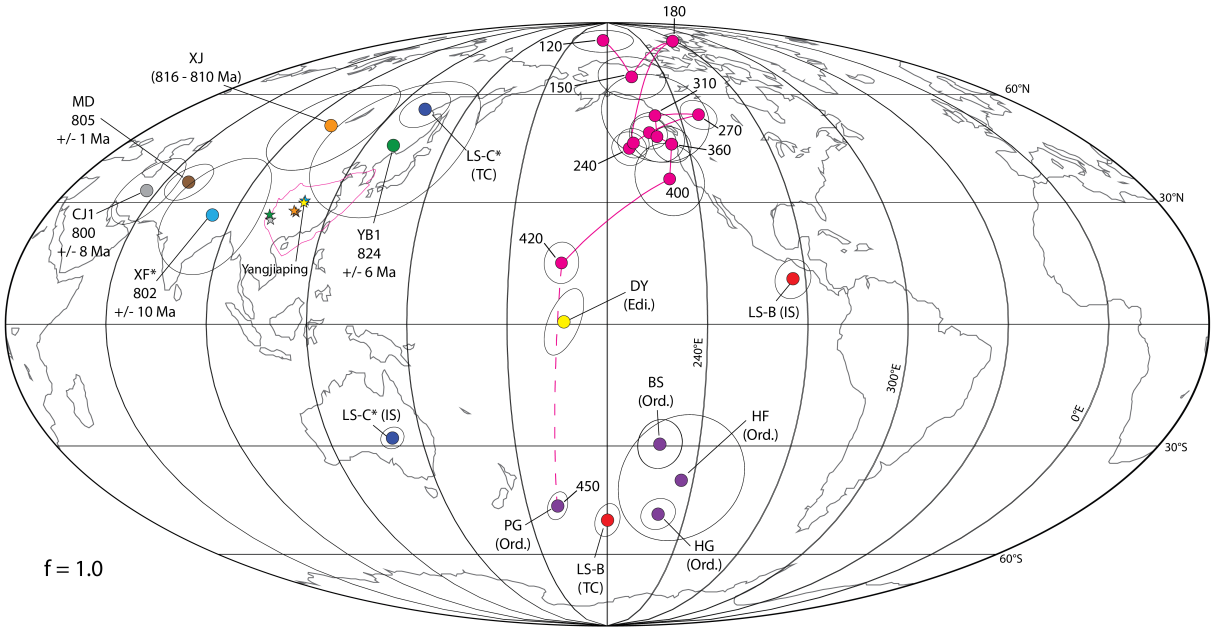

Figure 2.12: Laoshanya (LS) Formation poles from components B and C in in situ (IS) and tilt-corrected (TC) coordinates plotted with the APWP for South China from Huang et al. (2018) shown in pink. LS-C and Tonian (820-800 Ma) poles are shown in normal (northern hemisphere) polarity for the sake of comparison, although an inverted (southern hemisphere) configuration is also possible (Jing et al., 2021). LS-B is shown in reversed (southern hemisphere) polarity as the LS-B (TC) pole lies close to the 450 Ma segment of the APWP (the line is dashed as there is only one study pole, PG, older than 420 Ma). LS-B (IS) and LS-C* (IS and TC) lie far from the reference path. Table B.1 provides details of relevant Tonian poles (820-800 Ma). Ordovician (Ord.) poles are shown in purple (Table B.2). The Ediacaran (Edi.) pole from the Doushantuo Formation in Yangjiaping (DY) is shown in yellow. Stars indicate site locations. No shallowing correction was applied for this initial comparison (f = 1.0).*

interpret component A to be a Cretaceous overprint acquired during the normal superchron [120-83 Ma (Ogg, 2012)].

The interpretation of components B and C is more complicated. Taken at face value, both components could be primary, as they display near-identical thermal remanence behaviour. Fig. 2.12 plots the corresponding poles in both geographic and stratigraphic coordinates, together with a 450 to 120 Ma APWP for South China (Huang et al., 2018). The component B pole in tilt-corrected (TC) coordinates [LS-B (TC)] lies in proximity to the 450 Ma segment of the reference APWP. Component B in geographic/in situ (IS) coordinates [LS-B (IS)] and the TC and IS poles for component C lie far from the reference curve.

Fig. 2.12 also plots our data alongside select Tonian to pre-Devonian poles from the SCB (Tables B.1 and B.2, assessed in Appendix B). LS-B (TC) lies among several Ordovician poles for the SCB. Together with the rock magnetic and microscopic observations (Section 2.4), we interpret component B to be an Ordovician-aged chemical remagnetization. This coincides with a mineralogical study in Yangjiaping that indicates the Banxi Group may have experienced very low-grade metamorphism (ca. 260°C) in the mid-Paleozoic (Wang et al., 2014). Estimated temperatures increase to 360°C towards eastern Hunan and the Jiangnan belt, whose heat source was linked to the Wuyi-Yunkai (Caledonian) Orogeny (Wang et al., 2016a). Moreover, Cawood et al. (2018) suggested that the Banxi Group and its equivalents in the Jiangnan belt were reworked between 460 – 420 Ma; this timing is supported by metamorphic and petrogenetic analyses together with $^{40}Ar/^{39}Ar$ and U-Pb dating across the Wuyi-Yunkai orogen (Li et al., 2010).

The component C pole, LS-C* (TC), lies close to Tonian poles from the 824 ± 6 Ma Yanbian Dykes (Niu et al., 2016) and 816 – 810 Ma Xiajiang Group (Park et al., 2021). The similarity with other Tonian-aged poles, as well as its dual-polarity, lead us to interpret component C as primary. Reversal frequency in the Tonian (ca. 807.5 Ma) based on seven polarity intervals between 20 – 54 m (34 m), where the highest density of component C directions are found (Fig. 2.6a), yields 0.21 reversals per metre or 6.7 reversals/Myr (rev/Myr) given an accumulation rate of 32 m/Myr. This is a minimum value, as the true number could be higher if the signal was obscured by component A or B overprints. Our estimate for the Tonian is higher than the present rate of 4 – 5 rev/Myr for the past 5–10 Myr (Ogg, 2012), but is within estimated rates for the rest of the Phanerozoic, which often exceed 5 – 10 rev/Myr (Torsvik et al., 2021), and the Ediacaran at 6 – 24 rev/Myr (Hounslow et al., 2018; Meert et al., 2016). For comparison with other studies, we have grouped the component C directions into 'sites' of n=8–12 (Table B.3), although we use the filtered specimen mean (n=44) to define our pole (LS-C*).

2.5.2 Paleomagnetic poles from South China

We assess relevant Tonian (820-800 Ma) poles in Appendix B. We excluded poles CJ3 (Jing et al., 2020) and YB2 (Niu et al., 2016) because they lack reversals and fail the statistical requirements of Meert et al. (2020). Poles XJ, CJ1 and MD were derived from sedimentary rocks; Park et al. (2021) corrected these poles for inclination shallowing with a blanket flat-

tening factor (f) of 0.6. However, none of these studies applied any E/I or anisotropy-based methods to justify this factor. We applied the E/I correction method (Tauxe and Kent, 2004) to Laoshanya component C directions (n = 81) but could not obtain a meaningful result (i.e. our data were labelled 'pathological'), which may be due to contamination by the component A and B overprints. Our E/I assessment of all 169 specimen data from Park et al. (2021) corrected the mean inclination from -72.5° to -75.7°, equivalent to f = 0.81, although we recognise that the E/I method may overestimate shallowing effects if applied to data spanning several sites (e.g., Meng et al., 2017). Therefore, we find it difficult to justify using f = 0.6. To estimate a flattening factor, we applied a range of f values on inclinations from sedimentary poles (CJ1, MD, XJ and LS-C*) from 1.0 to 0.6 and compared them to those from igneous poles (XF* and YB1), keeping the igneous inclinations fixed (Table B.4). A value of f=0.8 produced the lowest standard deviation across all poles, so we used this value to correct the sedimentary poles. This assessment relies on an assumption that all the 820-800 Ma poles are coeval, which is discussed further below.

Fig. 2.12 shows that the Tonian poles appear to undergo high amplitude and rapid motion between 820 and 800 Ma, which some workers have previously interpreted as reflective of a rapid TPW oscillation (e.g., Jing et al., 2020; Li et al., 2004; Niu et al., 2016). However, Park et al. (2021) showed that the arc distances between the ∼815 and ∼805 Ma (Xiajiang and Madiyi) poles are much smaller than what would be predicted by the Bitter Springs TPW hypothesis, although they considered that this could be explained by differential plate motion. Park et al. (2021) also described how the data could be interpreted to represent a stable high-latitude position for South China at ca. 825-805 Ma, inconsistent with rapid TPW, if the Svalbard data are removed as constraints. Our new data from Laoshanya supports this interpretation, as our ∼808 Ma pole lies between the Xiajiang and Madiyi poles chronologically, but does not fall on the inferred TPW path. Furthermore, the Laoshanya (808 Ma) and Madiyi (805 Ma) formations are both precisely dated and very similar in age, but the poles are 50° apart, implying extremely rapid motion of ca. 17°/Myr, which is an order of magnitude greater than TPW rates estimated for the Phanerozoic (Torsvik et al., 2012). Therefore, in the following sections, we consider alternative hypotheses to explain the data.

Scenario 1: Vertical axis rotations dispel TPW

All the 820–800 Ma poles for South China show similarly steep inclinations, implying a high paleolatitude for the SCB (Fig. 2.12). We can be particularly confident in inclinations from sedimentary rocks, whose paleohorizontal can be robustly measured by the bedding attitudes. However, all paleomagnetic poles can be susceptible to uncertainty associated with vertical axis rotations, especially when going far back in time, like in the Precambrian. Vertical axis rotations can lead to poles distributed along small circles centered on the sampling sites, as shown in Fig. 2.13(a). Therefore, the large changes in declination can be explained without the need for IITPW, if rotations are permitted. Although the interior of South China experienced only minor rotations (<20°) since the Cretaceous (Meng et al.,

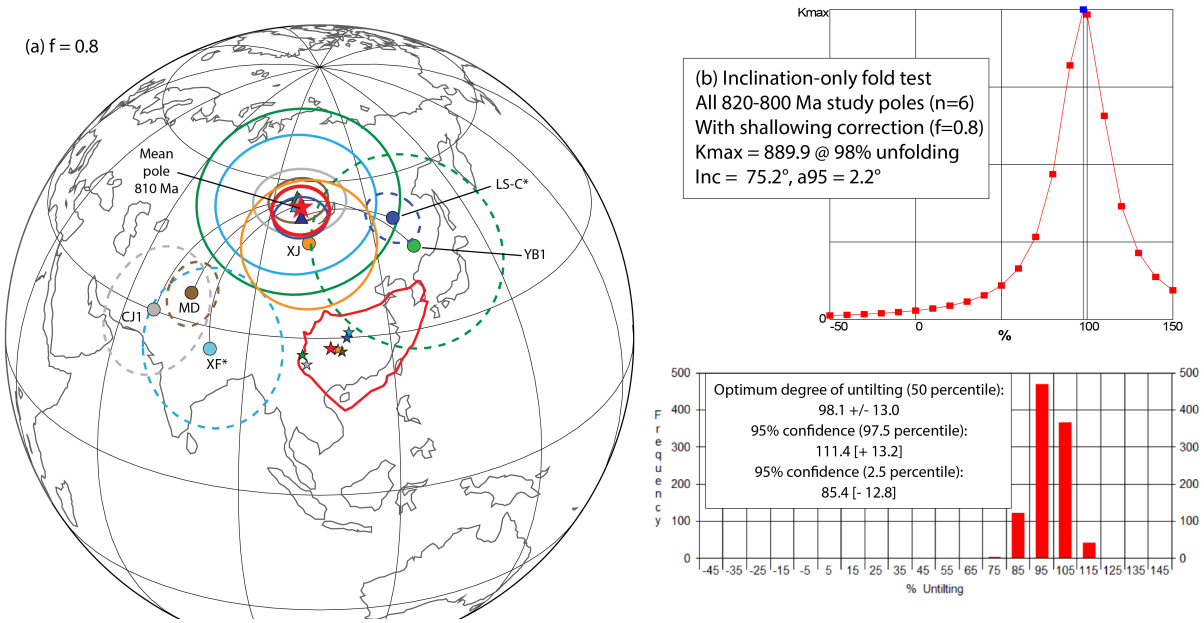

Figure 2.13: Scenario 1: Can vertical axis rotations explain discordant paleomagnetic data in the Tonian? (a) If allowed to rotate, all Tonian poles (820-800 Ma) collapse to define a group pole ca. 810 Ma. XJ was held fixed as its site location (and pole) lies between all the other sites (and poles). The outline of the SCB and the group mean pole are in red. Dashed circles indicate pole locations before vertical axis rotations. Poles are summarized in Table B.1 and Appendix B. (b) An inclination-only fold test with parametric sampling (Enkin and Watson, 1996; Watson and Enkin, 1993); k maximizes at $98 \pm 13\%$ *unfolding.*

2022), Permo-Triassic rocks exhibit a large variability in declination that matches the rotational amplitude of the Tonian data (Gilder et al., 2008; Tan et al., 2007). We therefore entertain the possibility in Scenario 1 that the SCB experienced internal vertical axis block rotations that streaked the Tonian poles out about a small circle centered on the sampling sites.

Under this scenario, all poles are considered to be based on primary, approximately coeval magnetizations, obtained at similar paleolatitudes. We arbitrarily kept XJ fixed as it passed a regional fold test and its site and pole lie in the middle of the other sites and poles. After allowing the other 820-800 Ma poles to freely rotate about their respective sampling sites, the poles come into close coincidence (Fig. 2.13a). If the data were primary, a regional fold test on the directions would be meaningless given the dispersion in declination, yet an inclination-only fold test would be independent of the differential rotations. An inclination-only fold test (Enkin and Watson, 1996) yielded a maximum precision parameter κ_{max} at $98 \pm 13\%$ unfolding with an inclination of 75.2° (Fig. 2.13b). Therefore, by accounting for vertical axis rotations, the 820-800 Ma South China poles can be explained without the need to invoke rapid TPW, extreme plate motion or anomalous field behaviour. Assuming that Xiajiang is representative of the overall continent (without vertical axis rotation), we thus calculate a mean pole of $P_{lat} = 54.1°$, $P_{lon} = 99.0°$ ($A_{95} = 5.0°$, N = 6 studies) which we consider representative of the Tonian for the SCB at ca. 810 Ma.

The rotations required by Scenario 1 are quite large (over 90° between CJ1 and LSC/YB1), so it is worth considering whether these are realistic with respect to the tectonics of South China. The structural framework of the Yangtze craton is dominated by a large curved orocline, readily observed in regional maps and satellite imagery. Tan et al. (2007) and Gilder et al. (2008) showed that this trend is reflected in paleomagnetic directions from Late Permian to Middle Triassic rocks in South China. Differences in rotations can exceed 180° among sites when integrating over the past ca. 300 Myr. Rotation magnitudes could be even more dispersed when integrated over an additional 500 Myr.

Scenario 2: Pervasive Ordovician remagnetization

In Scenario 2, we consider the possibility that remagnetization is pervasive in the SCB. We fit a small circle running through three, presumably primary Ordovician poles (HF, HG and BS), centered on their mean site location (Fig. 2.14a). When plotted in the southern hemisphere, the 'Tonian' CJ1, MD and XF* poles lie near the small circle swath, suggesting that Ordovician remagnetization may be a common feature that better explains the origin of their remanences. Indeed, the Madiyi (MD) pole was derived from silty mudstones, like component B in the Laoshanya Formation. This is curious, as silty mudstones can carry primary detrital remanences, as revealed through intraclast conglomerate tests (Opdyke and DiVenere, 2004; Swanson-Hysell et al., 2019; Tauxe et al., 1980). The Chengjiang (CJ1) study also reports a mid-inclination secondary component (CJ3) which is offset from the primary component (à la Laoshanya components B and C). Therefore, an Ordovician remagnetization advocated in Scenario 2 provides an alternative explanation for the rapid pole variations ca. 805 Ma, whereby some of the magnetization components are wholly or

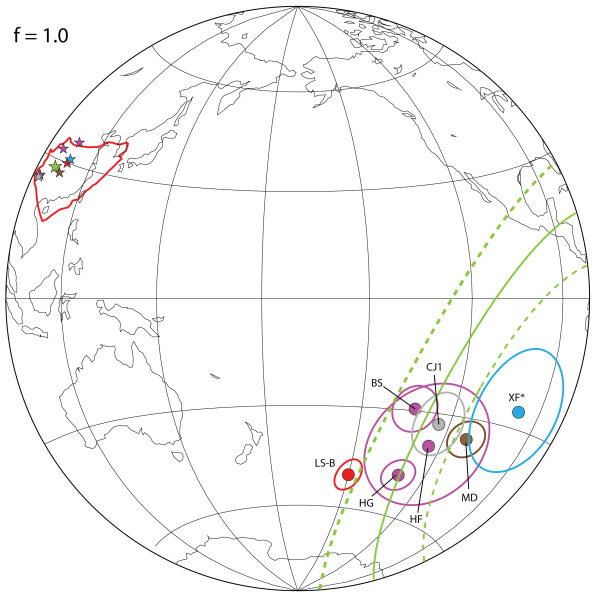

Figure 2.14: Scenario 2: Can an Ordovician remagnetization account for the discordant directions in South China? When plotted in the southern hemisphere, the CJ1, MD and XF poles (Table B.1) overlap with several Ordovician poles (purple, see Table B.2), suggesting they may be affected by Ordovician remagnetization. No corrections for inclination shallowing were applied in this comparison (f=1.0). A small circle (green) is plotted through HF, HG and BS poles, centered on the mean site location (PG was excluded from the small circle calculation as it has a significantly different inclination). Dashed lines show* 95% *confidence limits.*

partially overprinted. Large amplitude and rapid TPW would therefore be explained as a mixing of components acquired at distinctly different times.

Remagnetization could have occurred during a mid-Paleozoic deformation event (i.e. the Wuyi-Yunkai Orogeny). Consistent with this idea, Chang et al. (2022) mapped the Banxi Group as unconformably overlain by Devonian strata, thereby supporting an Ordovician-Silurian deformation event. 90 km to the south-east of Yangjiaping, an angular unconformity occurs at the top of the Middle Ordovician Guniutan Formation (Schmitz et al., 2010), however, near Yangjiaping, the formations above and below the Guniutan Formation have similar bedding orientations. Chen et al. (2014) described a significant hiatus between the Ordovician Wufeng and Silurian Longmaxi (Lungmachi) formations in Zhangjiajie, 100 km south of Yangjiaping. Zheng et al. (2020) dated the onset of this hiatus to 447 ± 1.4 Ma using rhyolitic tuffs in the top of the Wufeng Formation, 30 km to the north of Yangjiaping, and linked the hiatus to deformation/uplift caused by the Wuyi-Yunkai Orogeny. An Ordovician age for the deformation and remagnetization is consistent with the apparent age of component B in the Laoshanya Formation, as its pole overlaps several Ordovician poles.

2.5.3 Summary of discussion

We show that rapid pole variations postulated for ca. 820-800 Ma can be explained by vertical axis rotations and/or regional remagnetization in South China, without invoking extreme plate motion, rapid TPW or abnormal field geometry. South China's poles for this time are distributed along a small circle centered on the mean site location and can be brought into close alignment if vertical axis rotations are permitted. Furthermore, some poles derived from Tonian-aged rocks lie within a swath of Ordovician poles (when plotted in the same hemisphere), leading us to conclude that paleomagnetic data from other Madiyi-equivalent formations may reflect a regional overprint, not primary remanences. A complicated mixture of primary and secondary magnetizations may have led some studies to support a rapid TPW (or IITPW) event. Similarity between South China's Tonian and Ordovician paleolatitudes could be contributing to the confusion, if an Ordovician remagnetization is widespread.

Our results call for careful consideration of paleomagnetic signals in sedimentary sequences containing diverse lithologies, particularly those with hematite-bearing (red) mudstones and sandstones. Further work is needed to unravel the response of the Yangtze craton to the Wuyi-Yunkai Orogeny and understand mechanisms for (re)magnetization of pre-Silurian strata. If the discordant poles are indeed artefacts of a tectono-thermal event in the Ordovician, then any proposed remagnetization mechanism must be capable of resetting or overprinting paleomagnetic signals across a range of lithologies and magnetic mineralogies, as is also true for the Cretaceous overprint component.

2.6 Conclusions

The Laoshanya Formation in Yangjiaping contains a complicated paleomagnetic record which offers a unique opportunity to investigate remanence acquisition processes in hematite-bearing sedimentary rocks. Remarkably, the red beds seem to have preserved a primary (depositional) Tonian signal (component C), as well as secondary magnetizations residing in hematite created in the Ordovician (B) and/or Cretaceous (A). From our study we conclude the following:

1. Stepwise thermal demagnetization of 1152 samples isolated three end-member magnetization components (A-C) that combine in a complex and out-of-sequence manner throughout the 85 m of sampled section. Vector unmixing identifies the proportions of the three components, which are distinguished by their rock magnetic characteristics and microscopy, and may respectively represent the most common hematite phases found in red beds: pigmentary coatings, intergranular authigenic grains, and detrital specularite grains.

2. Component A is an overprint acquired during the Cretaceous normal superchron, a common direction found throughout South China. Thermal remanence curves for this component are consistent with fine-grained or pigmentary hematite, assumed to have formed by the oxidation of Fe-rich minerals. This interpretation is consistent with rock magnetic experiments and microscopic observations of abundant (< 1 µm) hematite flakes and needles in all specimens.

3. Component B is found mostly in fine-grained beds and likely formed authigenically at temperatures up to 260°C in Yangjiaping, and up to 360°C in Tonian-aged red beds farther south. In the Laoshanya Formation, the component resides in fine idiomorphic hematite crystals (1–2 µm) and/or in dense clusters/pseudomorphs of microplaty hematite. The corresponding pole lies near several Ordovician poles from the SCB, suggesting that the age of magnetic acquisition is Ordovician. We link component B to a regional low-grade tectono-thermal (< 260°C) event in the Late Ordovician, which may have partially or fully remagnetized pre-Silurian formations on the Yangtze craton.

4. Component C is carried mostly by coarse-grained hematite and is interpreted to be a primary remanence based on a positive reversal test. High-precision U-Pb dating of zircons extracted from two tuff horizons in the section yielded dates of 807.52 ± 0.18/0.27/0.91 Ma and 804.50 ± 0.22/0.30/0.91 Ma, which constrain the depositional age of the section between 809 and 804 Ma (using linear extrapolation). The primary nature of Component C is further supported by its agreement with some coeval poles from South China. Our new pole supports a stable, high-latitude position for the SCB between 809 and 804 Ma, and therefore a peripheral location with respect to the Rodinia supercontinent.

Chapter 3

Geochemical and petrophysical data distinguish primary and secondary magnetizations in Precambrian sediments from South China

Abstract

Vector unmixing analyses of 1188 Precambrian red bed samples from South China (Laoshanya Formation, Hunan Province) identified three magnetization components: a primary (ca. 805 Ma) detrital remanence and two overprints, one thought to be Ordovician–Silurian in age and the other Cretaceous. Here, we report geochemical, petrophysical and mineralogical data that fingerprint the three magnetization components. We find that rocks with primary paleomagnetic signals contain high relative abundances of coarse quartz and feldspar grains and are impoverished in major and trace element concentrations. Rocks remagnetised in the Ordovician–Silurian have significantly higher densities, are relatively abundant in phyllosilicates (particularly muscovite), and have high alkali (Cs, Be, Rb and K) concentrations. Rocks containing a significant Cretaceous overprint exhibit the highest iron concentrations and correlate strongly with rare-earth elements and heavy metals. Only weak correlations exist between any magnetization component and permeability or connected porosity. The data lead us to conclude that remagnetisation (overprinting) was mainly caused by thermal alteration of existing clay minerals yet was not due to the influx of external fluids that permeated the rocks. Fluctuating abundances of clay material produced an unusual pattern of alternating primary and secondary paleomagnetic signals in the Laoshanya Formation. The occurrence of a very low-grade tectono-thermal event in northwest Hunan is consistent with regional observations of clay mineralogy. Our innovative approach could be used to identify and characterise remagnetisations in other red beds containing complicated paleomagnetic signals arising from hematite.

Reference

This chapter is in preparation for Geochemistry, Geophysics, Geosystems.

Tonti-Filippini, J.A., Muller, E., Robert, B., Dellefant, F., Weller, D., Busigny, V. and Gilder, S.A. (in prep.). Geochemical and petrophysical data distinguish primary and secondary magnetizations in Precambrian sediments from South China. Geochemistry, Geophysics, Geosystems. TBD.

Contributions

Funding proposal – BR and SG. Petrographic observations – FD and JT. Geochemical, isotopic and mineralogical analyses – EM and VB. Petrophysical measurements – DW. Vector unmixing analyses – JT. JT wrote the manuscript with significant input from the other authors.

3.1 Background

Reconstructing the pre-Pangean geography of South China is a long-standing geophysical problem (e.g. Cawood et al., 2020; Jing et al., 2021; Park et al., 2021). The paleomagnetic record of the Neoproterozoic, in particular, is complicated by large and apparently rapid changes in magnetic directions which have been linked to episodes of enhanced true polar wander (TPW) caused by dramatic fluctuations in mantle convection behaviour (e.g. Fu et al., 2022). However, many studies from South China supporting rapid TPW in the Neoproterozoic are based on observations from red sedimentary rocks with complicated magnetisation histories (Zhang and Piper, 1997). Chapter 2 showed that the rapid changes in paleomagnetic directions, observed in Tonian sedimentary rocks in South China, could be artefacts of mid-Paleozoic remagnetisation, where subtle changes in lithology had an influence on a rock's ability to preserve a primary magnetisation and its susceptibility to later remagnetisation. If a mid-Paleozoic remagnetisation is widespread, it may be corrupting other interpretations of paleomagnetic data, e.g. Jiao et al. (2018) and Jing et al. (2022) also postulated rapid TPW events for South China in the Cambrian and Ordovician, respectively.

Primary depositional signals are often obscured by low-grade diagenetic and metamorphic overprinting (Posth et al., 2013). Chemical remagnetisation is a matter of persistent debate in paleomagnetism (Elmore et al., 2012), and is intertwined with our understanding of the physical connections between tectonic events, magmatism, fluid flow and mineralisation (e.g. Walter et al., 2018). Temporal and physical proximity of chemical remagnetisations to orogenic activity is frequently observed and has led many to believe that orogenically-driven fluids play an important role in the formation of secondary magnetisations (Oliver, 1986). But chemical remanent magnetisations (CRMs) can often be found in rocks with very low permeabilities and without evidence for fluid alteration, which require an alternative explanation (e.g. Katz et al., 1998). Diagenetic processes can form CRMs in terrestrial sandstones and carbonates without the presence of external fluids, e.g. by the dissolution/remobilisation of ferrous ions through maturation of organic matter, or the release of ferrous ions during illitization of clay minerals (Maxbauer et al., 2016a, and references therein).

Subtle diagenetic effects are particularly problematic for paleomagnetists studying hematite-bearing sedimentary rocks, which are often targeted for their relatively stable magnetisation. Hematite can occur as a detrital mineral as well as the result of many diagenetic processes, e.g. as fine-grained pigmentary coatings or as large crystalline (specularite) grains (Løvlie et al., 1984). Much debate surrounds the nature of magnetisations carried by specularite, as there appear to be many examples where it can carry both a detrital remanent magnetisation (DRM) and/or a CRM acquired millions of years after deposition (Kodama, 2012). Remagnetisations are typically detected with the aid of paleomagnetic field tests, such as fold and reversal tests (Van der Voo, 1990). However, these tests may not always constrain the timing of the magnetisation and false-positives can occur, e.g. if the remagnetisation has occurred a long time after deposition but before folding, or if the remagnetisation occurred over a long interval of dual geomagnetic field

polarities (Huang et al., 2020). This can be particularly complicated if a rock carries both DRM and CRM components with similar unblocking spectra, which can result in a spurious single component which behaves like a primary magnetisation (Dinarès-Turell and McClelland, 1991).

The 809 – 804 Ma Laoshanya Formation in Yangjiaping presents a unique opportunity to investigate remanence acquisition processes in hematite-bearing sedimentary rocks (Chapter 2). Three paleomagnetic components were identified in order of their relative dominance, based on thermal demagnetisation of 1188 core specimens. Component A is ubiquitous in the section and appears to be a single-polarity Cretaceous overprint acquired after folding (north and down in geographic coordinates), which is common across South China (Gilder and Courtillot, 1997). Component B is found in 8% of specimens and is represented by single-polarity mid-inclination directions (south-east and up in tectonic coordinates), which is probably a mid-Paleozoic (Ordovician) remagnetisation. Component C is found in 7% of specimens and contains steep dual-polarity directions (in tectonic coordinates), and is interpreted to be a primary (or early diagenetic) signal. Throughout this chapter we refer to component C as primary, component B as secondary, and component A as tertiary. Component A unblocks below 660 °C, while components B and C unblock up to 680 °C. The components appear to reside in different generations of hematite, which complicates the analysis of demagnetisation data and best-fitting line procedures (Kirschvink, 1980). Chapter 1 showed that the three components have superimposed unblocking spectra which can be isolated and quantified using vector unmixing analysis.

The primary component (C) appears to be more dominant in coarser-grained beds, while the secondary component (B) is found more frequently in finer-grained beds (Chapter 2), indicating that grain size and/or porosity may play a significant role in remagnetisation. The pole derived from component B is similar to several derived from Precambrian strata nearby (e.g. Xian et al., 2020), suggesting that mid-Paleozoic remagnetisation may be a regional effect. However, it is difficult to explain how such a phenomenon can be so widespread yet mysteriously selective. For example, component B directions were not found in the Lengjiaxi Group (below the Laoshanya Formation) or in the study of a younger (Ediacaran) formation from the same section (Macouin et al., 2004). Remagnetisation in the Ordovician could be linked to an orogenic event, which probably reworked formations in the Jiangnan Belt ca. 460 – 420 Ma (Cawood et al., 2018). Although recorded observations of a mid-Paleozoic orogeny in South China date back nearly a century (Ting, 1929), explanations of its mechanisms and effect on the Yangtze Craton are outstanding problems (Charvet, 2013; Domeier, 2018; Zheng et al., 2020).

A widespread remagnetisation in Yangtze Craton could be the result of migrating fluids (e.g. organic or Fe-rich rich fluids, or alkaline/hydrothermal brine). According to Lan et al. (2019, and references therein), the mid-Paleozoic orogeny induced low greenschist metamorphism in South China's pre-Silurian strata, with composite folding, regional cleavages, shearing, and emplacement of granites, and is responsible for the production of key hydrothermal ore deposits concentrated between 445 – 420 Ma. Observations from scanning electron microscopy (SEM) of samples from the Laoshanya Formation showed some remobilisation of iron, e.g. titanohematite (or former ilmenite) grains in various states of

alteration, often leaving behind rutile grains with relict skeletal and trellis structures, and abundant 1–2 micron hematite flakes scattered throughout the surrounding matrix (Chapter 2). Alkaline fluids can infiltrate fine-grained sediments and enhance the reddening of clay minerals, often altering or replacing detrital minerals with Fe-oxides (Walker, 1976). Fe-Ti oxides can also breakdown during hydrothermal activity, forming rutile and releasing iron into fluids (Pochon et al., 2017).

Given the selective nature of the remagnetisation, a mechanism dependent on external fluids would require the finer-grained sediments to have maintained greater porosity and/or permeability than the coarser-grained sediments. However, remagnetisation could also be a product of thermal alteration. Wang et al. (2014) studied clay mineralogy in Yangjiaping and estimated a peak anchi-metamorphic temperature of 260°C for the Banxi Group in northwest Hunan (which they link to the mid-Paleozoic orogeny). Selective remagnetisation by thermal alteration would therefore be dependent on the abundance of reactive and/or hydrated clay minerals, which can precipitate Fe-oxides in situ. Ilmenite can also breakdown to rutile and hematite by oxidation at temperatures below 400 °C (McEnroe and Brown, 2000).

In this chapter, we explore possible mechanisms for an Ordovician remagnetisation in the Yangtze Craton, with detailed observations of samples from the Laoshanya Formation in Yangjiaping. Understanding the nature and timing of remagnetisation in Yangjiaping, where both primary and secondary magnetisations appear in the same outcrop, is crucial for decoding the complicated paleomagnetic record of the Yangtze Craton and mid-Paleozoic tectonic events in South China. To aid our comparison, we performed several geochemical, isotopic, petrophysical and mineralogical analyses to supplement the paleomagnetic and rock magnetic experiments detailed in Chapter 2. Our analyses are compared to the results of vector unmixing of the paleomagnetic data (Chapter 1), which allow us to quantify the absolute contributions of paleomagnetic components and test remagnetisation hypotheses.

3.2 Methods

3.2.1 Microscopic analyses

Petrographic observations were made on thin sections with a transmitted and reflected light microscopes. Scanning electron microscope (SEM) observations on the same thin sections are presented in Chapter 2.

3.2.2 Geochemical and isotope analyses

40 samples were selected for geochemical analyses. Bulk chemistry and trace element concentrations were measured using Multi Collector Inductively Coupled Plasma Mass Spectrometry (MC-ICP-MS) at the Institut de physique du globe de Paris (IPGP, France). Approximately 50 mg of powdered samples was dissolved using a mixture of concentrated HF-HNO3, evaporated to dryness, re-dissolved in Aqua Regia solution and re-evaporated

to dryness, all in PFA beakers heated to 110 °C in a class 1000 clean laboratory. The residues were then re-dissolved in 10 ml 3N HNO3 overnight at 80 °C and archived. Splits of 100 μl from the archive solutions were taken up in 5 ml $\sim$ 0.28 M HNO3 for ICP-MS measurements. An internal standard (TILL01) and a procedural blank were also prepared with the samples. Iron concentration was measured with an Agilent 7900 quadrupole ICP-MS at IPGP. Measurements were performed using a collision-reaction cell with helium gas (5 ml/min) to remove polyatomic interferences. A scandium internal-standard was injected after inline mixing with the samples to correct for signal drift and matrix effects. The uncertainty on the elemental concentration measurements was lower than $\pm$ 5 %.

3.2.3 Petrophysical measurements

34 core samples were measured for rock density, permeability and connected porosity at LMU Munich. Permeability measurements were made using a Vinci Technologies steady-state gas permeameter (GPE) at room temperature. Connected porosity measurements were made with a Quantachrome Instruments Ultrapyc 1200e Helium gas pycnometer.

3.2.4 XRD analyses

For 15 selected core samples, a slice of about 10 g was finely ground and homogenized in an agate mortar and used for X-ray diffraction (XRD) at IPGP. XRD analyses were performed using a Panalytical Xpert Pro transmission diffractometer with a copper anode operated at 45 kV and 40 mA and a slit of 0.5° at 240 mm radius distance. The 2θ scan was performed in the continuous mode from 4° to 90° (2θ) with a step of 0.0001°. Peak identification was performed using pattern search on the X-ray diffraction database of reference spectra "Crystallography Open Database (COD)" (from http://www.crystallography.net/). XRD identifications were cross-checked with results from energy dispersive X-ray spectrometry (EDXS) elemental composition data obtained by scanning electron microscopye (SEM) to more confidently identify the mineralogy of (core) samples. The relative abundance of the major minerals ($>$ 5%) was then estimated by Reference Intensity Ratio in the DIFFRAC.EVA software (Brucker), a semi-quantitative method.

3.3 Results

3.3.1 Microscopy

In Fig. 3.1, we present several images from conventional microscopy. Samples carrying a strong primary magnetisation (component C) are dominated by much larger quartz and feldspar grains (often $>$ 100 microns), and minimal red cement (Figs. 3.1a and c). Samples dominated by a secondary magnetisation (component B) appear to have a much greater proportion of fine-grained red cement, and quartz and feldspar grain sizes generally $<$ 50 microns (Figs. 3.1b and d).

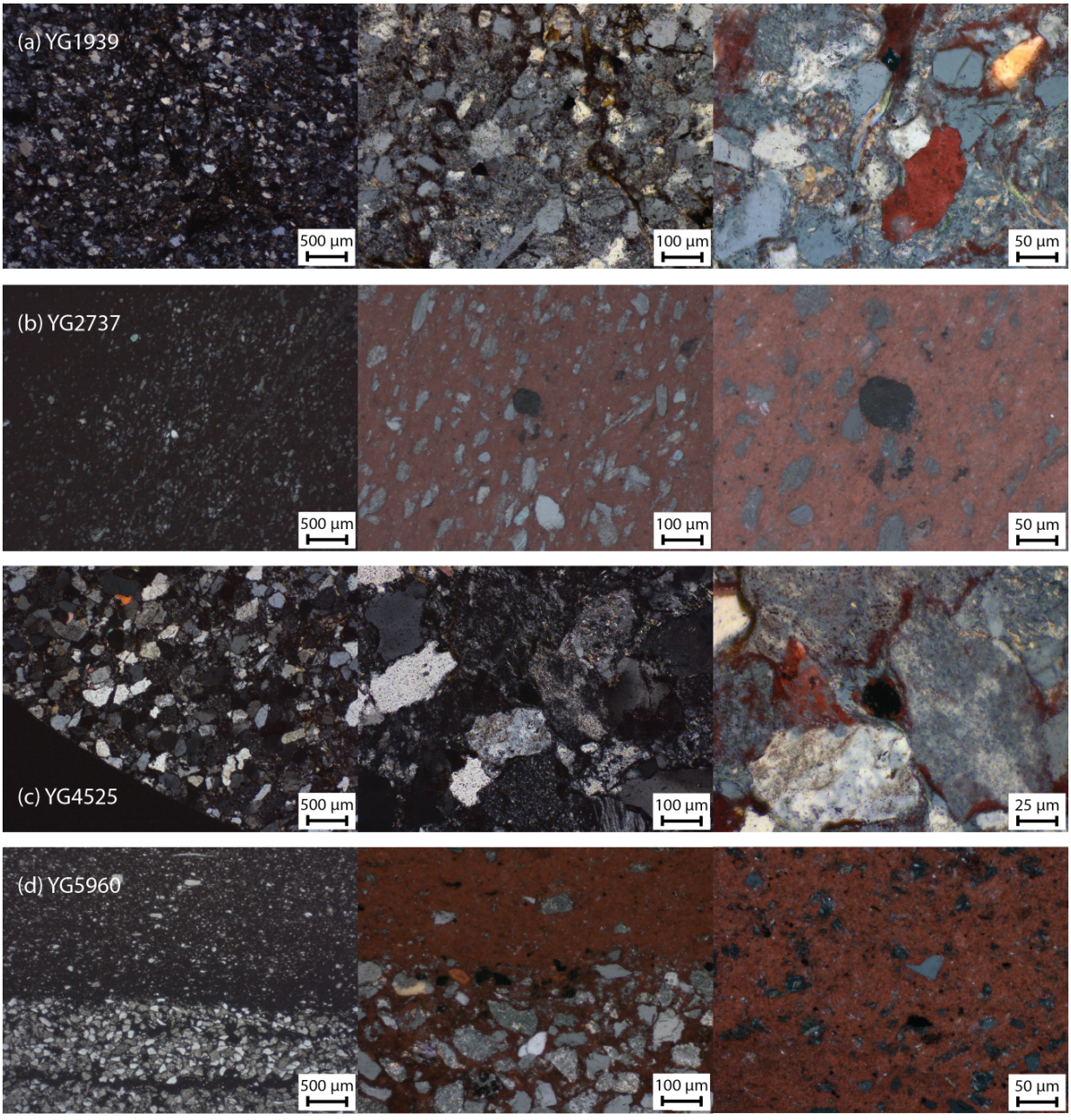

Figure 3.1: Transmitted light images for selected samples. (a) and (c) have a strong primary component C and contain much larger quartz and feldspar grains (ca. 100 – 200 µm), with minimal red cement. (b) and (d) have strong secondary A and B components, with smaller quartz and feldspar grains (< 50 µm) and a much greater proportion of red cement.

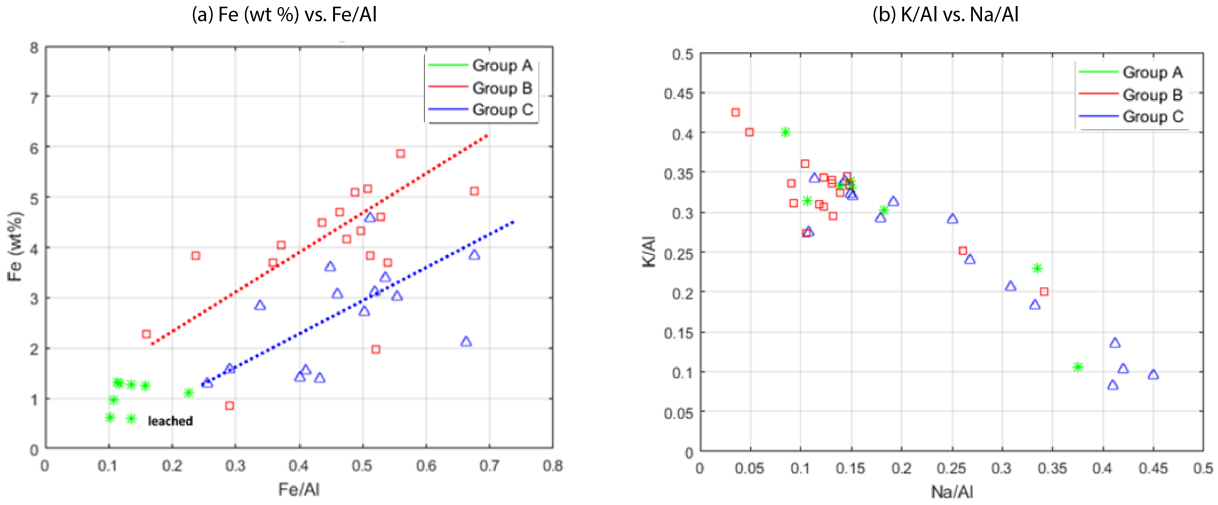

Figure 3.2: (a) Component groups A-C show different leaching trends, with group B relatively enriched in Fe. Specimens containing only component A appear to be the most leached. Groups B and C both appear to be trending towards group A, but from different starting points. (b) Groups B and C have different proportions of K and Na, relative to Al, which could reflect differences in feldspar composition. Data were normalised to Al as it appears to be resistant to leaching.

3.3.2 Geochemistry

The specimen component groups A – C are separated on an Fe (weight %) vs. Fe/Al leaching plot (Fig. 3.2a). We have normalised by Al to account for variability in detrital input, as Al appears to be resistant to leaching. Groups B and C appear to show two different leaching trends, with group B relatively enriched in Fe compared to group C. Group A specimens appear to have been most effected by the leaching process. Groups B and C are also separated on a K/Al vs. Na/Al plot (Fig. 3.2b).

18 samples were selected for Fe isotope analysis. Groups B and C are separated on plots of d56Fe vs. Fe wt.% (Fig. 3.3a) and d56Fe vs. Fe/Ti (Fig. 3.3b). Rayleigh distillation lines were calculated from sample YG4525, which appeared to be the least altered, with different fractionation factors α. Samples appear to be globally leached, with most samples leached by 50 per cent or more (relative to YG4525). Fractionation of 0.2 ± 0.1 is typical of abiotic reactions (biotic fractionations are usually higher). Samples from group B are more fractionated than groups A and C.

3.3.3 Petrophysics

As shown in Fig. 3.4(a), group B samples have a higher rock density, i.e. 2.75 – 2.85 g/ccm, than groups A and C which are generally ca. 2.7 g/ccm, closer to the density of pure quartz (2.65 g/ccm). Groups B and C have a very low permeability, ca. 0.4×10^{-17}

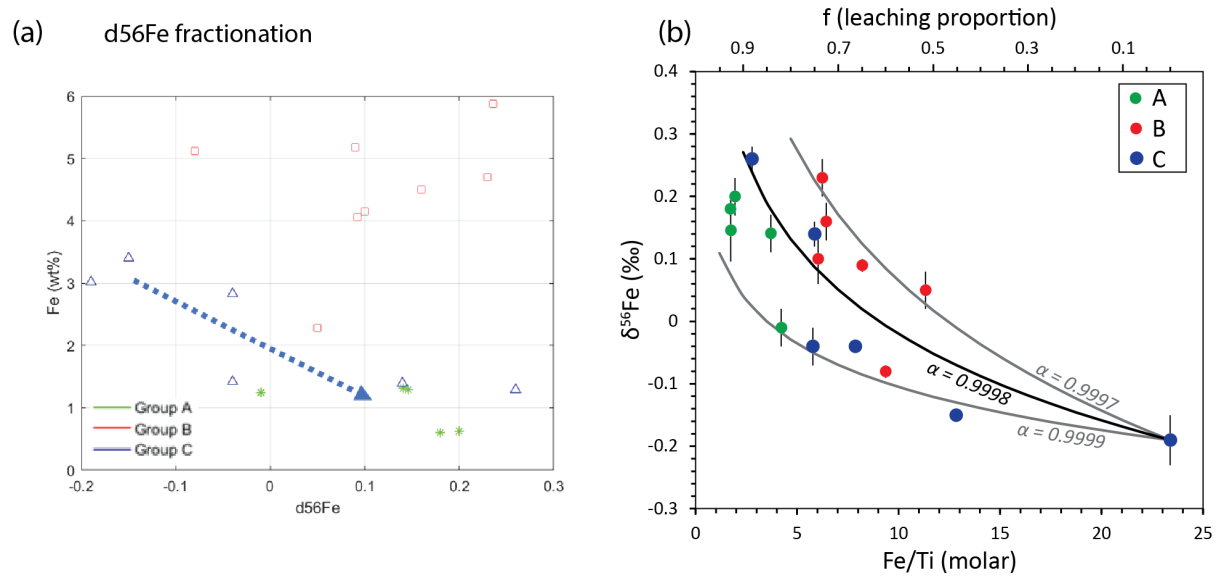

Figure 3.3: (a) Some group C samples show slightly negative d56Fe values (-0.2 to 0), while those for groups A and B are slightly positive (0 to +0.3). (b) Rayleigh fractionation lines are calculated from the least altered sample (YG4525). Most samples are leached more than 50 per cent (relative to YG4525). Group B samples are slightly more fractionated than groups A and C.

m^2, which is half the permeability of group A, ca. $0.8{\times}10^{-17}$ m^2 (Fig. 3.4b). Group C has the lowest connected porosity, between 1–3%, which is lower than group A, ca. 2–4%, and group B, ca. 2.5–5% (up to 9%) (Fig. 3.4c).

3.3.4 XRD results

Samples are dominated by quartz, feldspar (estimated by albite and anorthite), muscovite and chlorite, with only minor (< 5 % hematite). These results are presented and discussed further in Section 3.3.5.

3.3.5 Vector unmixing

Correlations with element concentrations

We compared the results of vector unmixing analyses (Chapter 1) with major and trace element concentrations of specimens for which we have data (Section 3.3.2). Unmixing results were filtered for those with a goodness of fit > 70%, which left 26 specimens. In Table 3.1, we present Pearson correlation coefficient (r) values for positive linear correlations between the estimated mass-normalised moments of each paleomagnetic component and element concentrations (measured in ppm or weight %). We consider r values > 0.7 to be strong, 0.5 to 0.7 moderate, 0.3 to 0.5 weak or low, and < 0.3 very weak or non-existent,

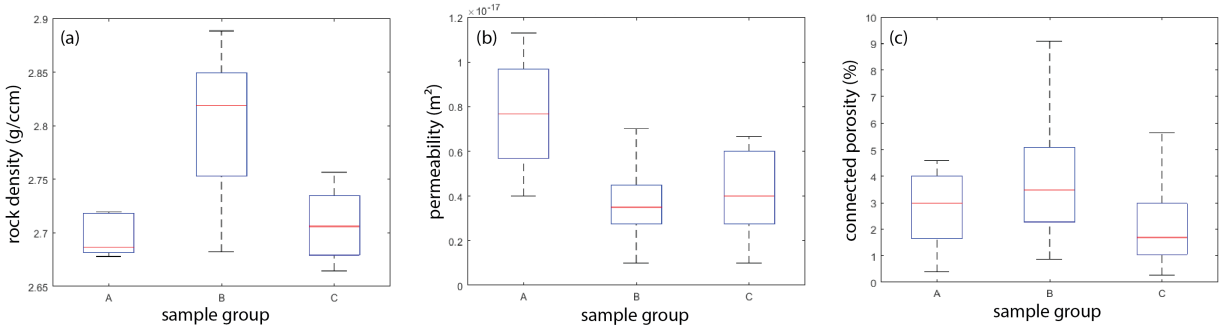

Figure 3.4: Petrophysical measurements for rock density (a), permeability (b) and connected porosity (c) across sample groups A-C. Group A has a low density and significantly higher permeability. Group B has a higher density and low permeability. Group C has a low density and low permeability. There is little different in connected porosity between component groups, although group C has the lowest (1-3%), and group B shows a lot of variability (up to 10%).

although this is subjective (Ratner, 2009).

Component A is strongly correlated with transition metals (particularly Y, Fe and Ti) and many lanthanides (e.g. Ho, Dy, Er and La). Component B is moderately correlated with several alkali and alkaline metals (particularly Cs, Be, Rb and K). Component C shows very weak or non-existent correlations across all elements. There were no significant negative correlations (i.e. r < -0.315) for any component. In Fig. 3.5 we show the two strongest correlations for components A and B respectively. For the geochemical analyses, we present the data in terms of absolute element concentrations and magnetic component magnitudes as these produced the strongest correlations. Normalising element data by Al or Ti, and/or normalising the component data as relative proportions (of total remanence) only reduced correlation coefficients.

Correlations with petrophysical properties

We also performed vector unmixing analyses for specimens subjected to petrophysical experiments, i.e. rock density, permeability and connected porosity (Section 3.3.3). Again, we filtered unmixing results for those with GOF > 70%, which left 27 specimens. In Fig. 3.6, we present the estimated component magnitudes (mass-normalised) against measured petrophysical parameters. Components A and B show moderate positive correlations with rock density, while component C has a weak negative relationship. Components A and B show weak negative relationships with permeability, while component C shows a weak positive relationship. Component B has a weak positive relationship with connected porosity, while A and C show no relationship.

As with the geochemistry data, correlations between petrophysical parameters and component magntitudes only decreased if we normalised the components relative to total NRM, with the exception of rock density. In Fig. 3.7, we present specimen rock den-

*Table 3.1: Correlation coefficients (r) for estimated component magnitudes (from vector unmixing analysis) versus major and trace element concentrations, with top 20 elements listed in descending order. Element concentrations were measured in ppm unless otherwise noted. Transition metals are in **bold**, lanthanides in italics, and alkali and alkaline metals are underlined. Component A appears to be well-correlated with transition metals (particularly Y, Fe and Ti). Component B shows strongest correlations with alkali and alkaline metals (particularly Cs, Be, Rb and K). Component C shows very weak or non-existent correlations across all elements (r < 0.3).*

	Component A		Component B		Component C	
Rank	element	r	element	r	element	r
1	**Y**	0.726	Cs	0.596	**Mo**	0.250
2	**Fe***	0.700	Be	0.569	**W**	0.167
3	*Ho*	0.694	*Er*	0.554	**Cd**	0.136
4	*Dy*	0.658	Tl	0.552	**Mn***	0.122
5	*Er*	0.657	Bi	0.549	As	0.095
6	Pb	0.648	Rb	0.547	**Ni**	0.086
7	*La*	0.640	*La*	0.542	Na*	0.076
8	Bi	0.630	*Ho*	0.536	**Cu**	0.056
9	**Ti***	0.596	**Y**	0.535	B	0.034
10	Sr	0.584	**Zr**	0.522	Li	0.031
11	Cs	0.568	K*	0.521	Ca*	0.029
12	*Tm*	0.562	*Tm*	0.520	**Cr**	0.023
13	Ge	0.538	Al*	0.500	**Ti***	0.023
14	*Tb*	0.530	*Dy*	0.500	Sr	0.017
15	Sb	0.492	Ba*	0.491	**Ag**	-0.001
16	**Cr**	0.491	Ga	0.488	**Zn**	-0.040
17	Be	0.490	B	0.488	Sb	-0.048
18	U	0.487	Ge	0.487	**Y**	-0.066
19	**Zr**	0.483	U	0.483	Cs	-0.072
20	*Pr*	0.473	**Hf**	0.473	*Ho*	-0.077

*measured in weight %.

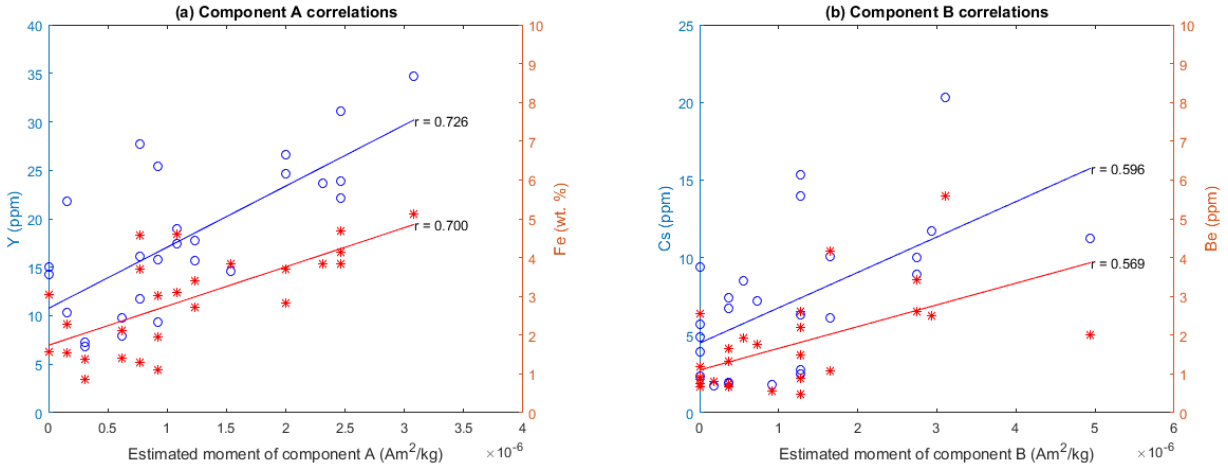

Figure 3.5: (a) The abosolute magnitude of component A, estimated with vector unmixing (Chapter 1), correlates strongly with Y (in ppm) and Fe (weight %). (b) Component B correlates moderately with Cs and Be (in ppm).

sity vs. the proportional contribution of each component (i.e. NRM_x/NRM_{total}, where $NRM_{total} = NRM_A + NRM_B + NRM_C$, from the unmixing analyses). Now we see a very weak/non-existent correlation with component A, but moderate positive and negative correlations with components B and C, respectively.

Correlations with mineralogy

Vector unmixing analyses was performed on the 15 samples for which we have XRD data (Section 3.3.4) and the results were filtered for those with GOF > 70%, which left 10 specimens. The strongest correlations are found when the components are represented as a proportion of the total NRM (Fig. 3.8). Component A has weak relationships with the abundance of quartz and feldspar, and with hematite concentration, but a moderately negative relationship with muscovite. Component B has a strong negative relationship with the abundance of quartz and feldspar, and strong positive relationships with the abundance of hematite and muscovite. Component C has the same strong relationships as component B, but in the opposite sense.

3.4 Interpretation and discussion

Our microscopy (Section 3.3.1) showed that specimens carrying the secondary component (B) are much more matrix-supported, with a greater proportion of red cement and smaller quartz and feldspar grains. The specimens carrying the primary component (C) have larger quartz and feldspar grain sizes, and minimal clay content (i.e. are clast-supported).

Geochemical analyses (Section 3.3.2) showed that group B is enriched in Fe relative to group C. We interpret this to indicate that either: group B was deposited with additional

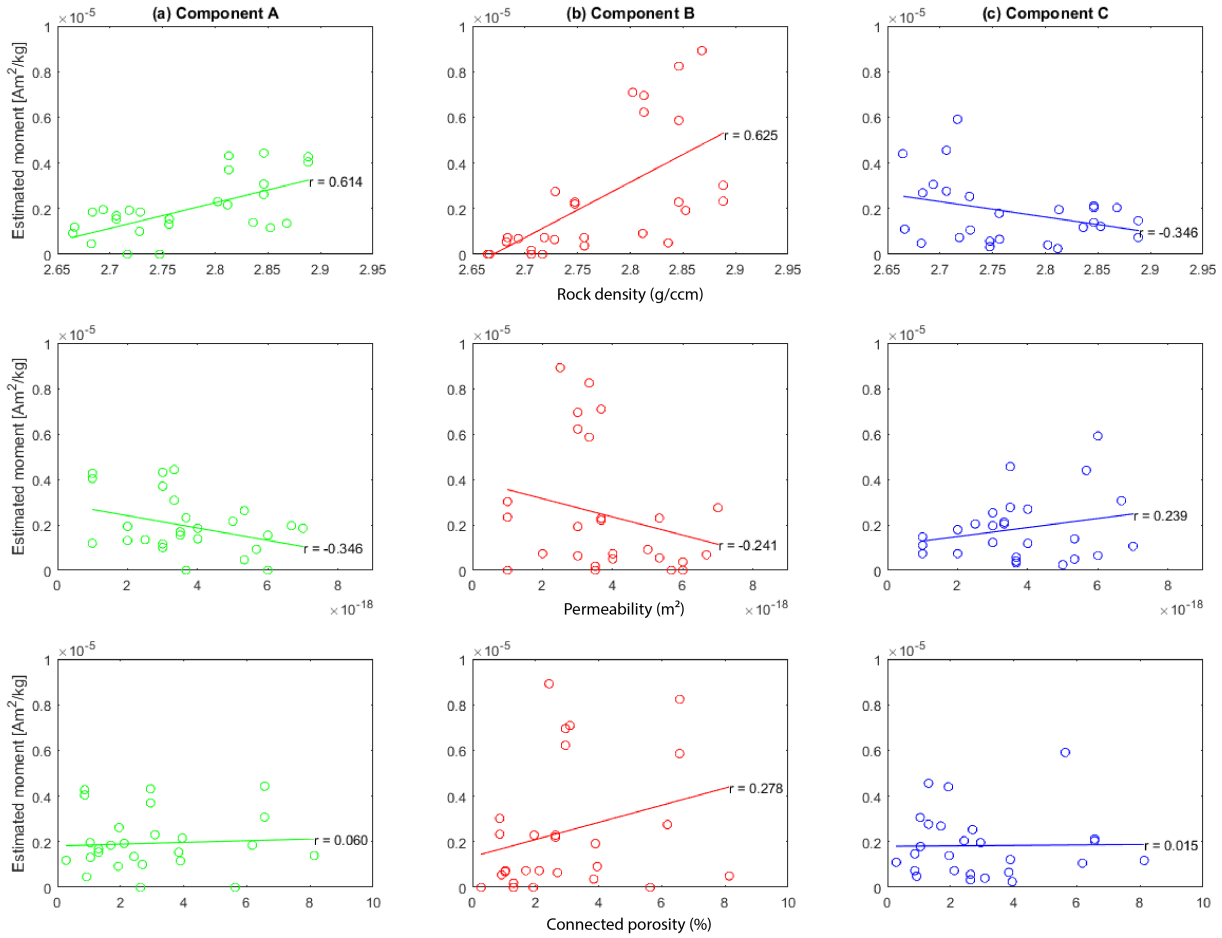

Figure 3.6: Component magnitudes (estimated with vector unmixing in Chapter 1) vs. petrophysical measurements. (a) Component A shows a moderate correlation with rock density and a weak negative relationship with permeability. (b) Component B correlates with rock density, but shows very weak or non-existent relationships with permeability. (c) Component C shows a weak negative relationship with rock density and very weak relationship with permeability. None of the components correlate with connected porosity (i.e $r < 0.3$).

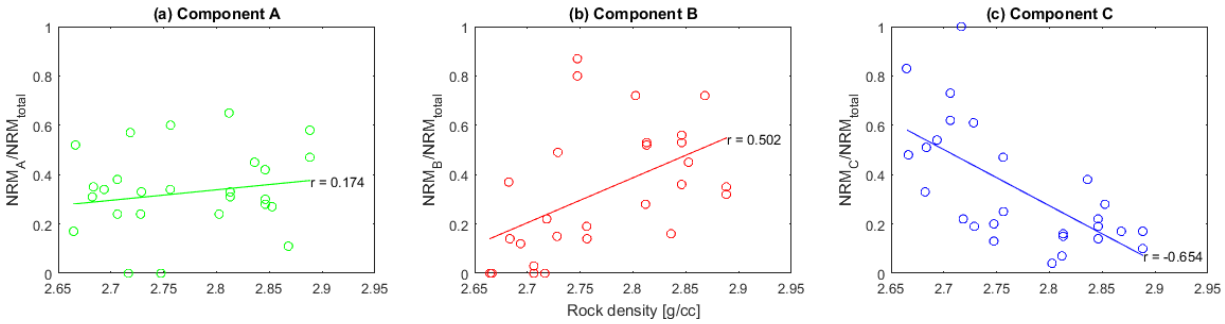

Figure 3.7: Component proportions (normalised by total magnetisation) vs. rock density. Components B and C show moderate positive and negative relationships with rock density, respectively.

Fe-bearing minerals, e.g. clays and aluminosilicates; or group B more readily absorbed or captured Fe-bearing fluids at a later stage. However, isotope analyses suggest that the section was globally leached, during which Fe was only depleted and not enriched. The least altered sample, YG4525, is also the sample with the largest grain sizes (Fig. 3.1c). Specimens containing only component A appear to be the most leached. Between groups B and C, there may also be differences in K/Al versus Na/Al, which we interpret to be changes in feldspar composition.

In Section 3.3.5 we showed that the magnitude of the Cretaceous overprint (component A) is strongly correlated ($r = 0.700$) with total Fe content (weight %), as well various REEs. A direct correlation with Fe content supports an overprint mechanism involving late-stage oxidation of existing Fe-bearing minerals and fine-grained hematite pigmentation, perhaps following uplift and/or infiltration of meteoric groundwater (Blodgett et al., 1993). The latter mechanisms seems unlikely as component A shows a weak negative relationship with permeability (Fig. 3.5), although we can only measure present-day permeability. During the Cretaceous, inland South China was dominated by an arid climatic environment, perhaps due to the presence of a coastal mountain chain preventing moist Pacific air from reaching the continent's interior (Chen et al., 2022). Prolonged oxidation and formation of fine-grained hematite during a stable superchron, the ca. 35 Myr Cretaceous Long Normal-Polarity Chron (Ogg, 2012), may explain why a Cretaceous overprint is so widespread in South China.

Interestingly, the magnitude of component B is not well-correlated with total Fe content. Rather, our analyses suggest that reactive elements (particularly alkali metals such as Cs, Be, Rb and K) may be more important indicators of remagnetisation. Katz et al. (2000) suggested a similar explanation for remagnetisation of the Vocontian trough, proposing that potassium content plays an important role in diagenesis of clays and subsequent chemical remagnetisation. Indeed, the proportion of Na to K (normalised to Al content), which we interpret to be representative of variations in feldspar composition, seems to be an important indicator of primary versus secondary magnetisation (Fig. 3.2b).

Our analyses in Section 3.3.5, show that rock density may also be an indicator of

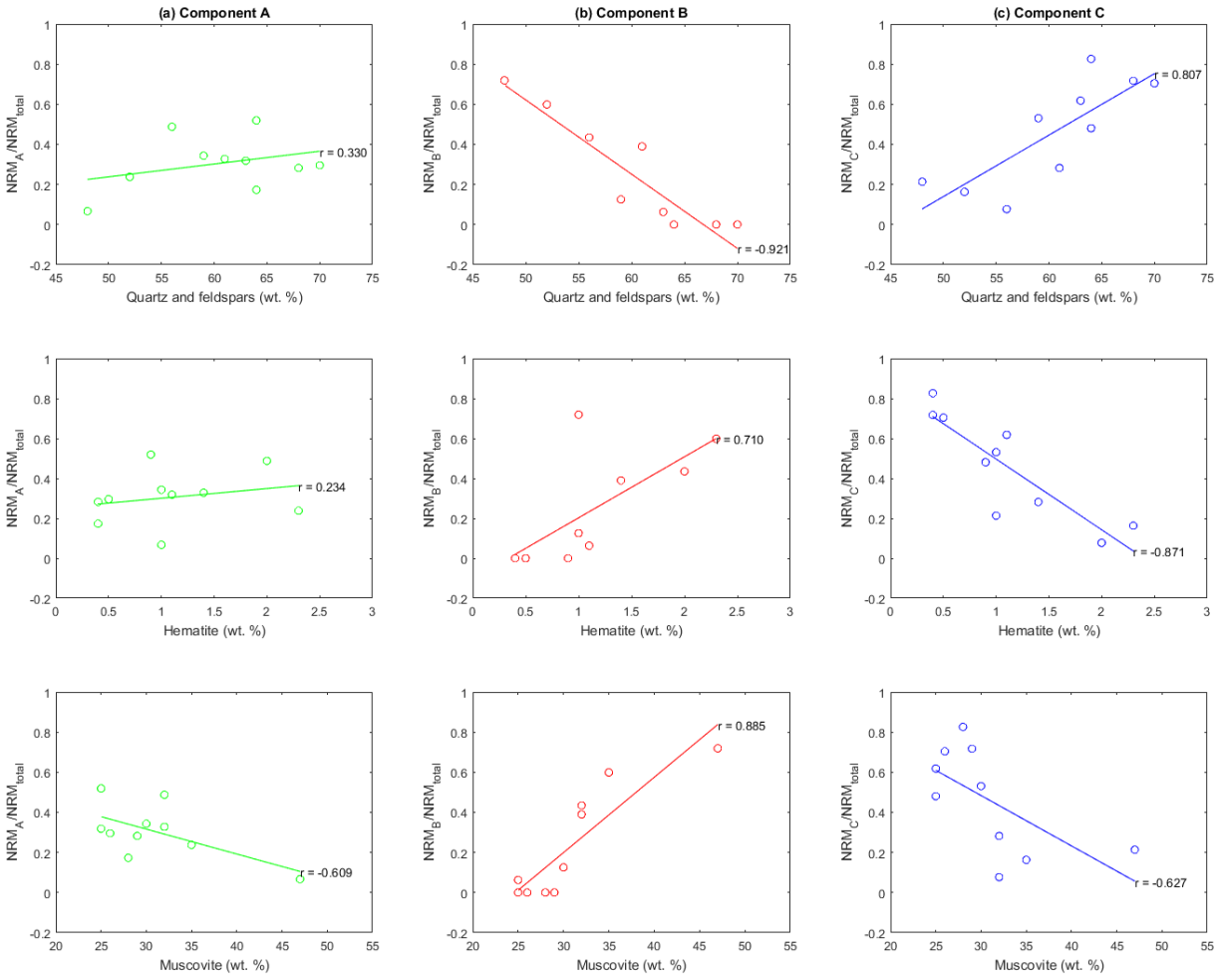

Figure 3.8: Component proportions (normalised by total magnetisation) vs. mineral quantities estimated by XRD (in weight %). (a) Component A shows moderate negative relationship with muscovite. (b) Component B shows a very strong negative correlation with the abundance of quartz and feldspar grains, and strong positive relationship with hematite and muscovite. (c) Component C is strongly correlated with the proportion of quartz and feldspar grains, and negatively correlated with hematite and muscovite.

remagnetisation in sandstones. Rock density has a moderate positive relationship with component B (r = 0.502) and a moderately strong negative relationship (r = -0.654) with component C (when normalised to total NRM). We interpret rock density as a proxy for relative grain size and abundance of clay content. Specimens containing components B and C have extremely low permeabilities, ca. 0.4 $\times 10^{-17}$ m^2 (Fig. 3.4a). However, somewhat counter-intuitively, the specimens containing component C have a significantly lower density, ca. 2.7 g/ccm (Fig. 3.4b), and a lower connected porosity, ca. 1–3 % (Fig. 3.4c). We speculate that quartz overgrowth may have played a significant role in the preservation of component C, enabled by the reduction of porosity and permeability during early diagenesis. Quartz cementation is the most important control on porosity in sandstones, which can be retarded or prevented by the the presence of clays bearing Fe oxides and hydroxides (Busch et al., 2017; McBride, 1989).

Our interpretation is supported by XRD analyses, which show that the proportions of components B and C are strongly correlated with the abundances of quartz and feldspars, muscovite, and hematite. This suggests that remagnetisation was probably limited by the original clay content. Muscovite, albite and chlorite can be detrital, but are also typical low-grade metamorphic minerals (Haldar and Tišljar, 2020, Chapter 6). Clay minerals (e.g. smectite) can be transformed to muscovite during very low-grade metamorphism (Árkai, 2002). Fe can be liberated from clay minerals during alteration and nucleate on phyllosilicates as hematite or a precursor to other Fe-oxides (Blodgett et al., 1993). Indeed, smectite has long been recognised as a source for Fe during widespread chemical remagnetisation (Katz et al., 2000). $^{40}Ar/^{39}Ar$ dating of micas (specifically biotite, muscovite and sericite) from Neoproterozoic rocks in the Jiangnan Orogen have revealed ages of ca. 450–420 Ma (Li et al., 2016; Xu et al., 2015), consistent with the timing of the Paleozoic orogeny.

3.5 Conclusions

In this paper, we investigated magnetisation mechanisms for three paleomagnetic components identified in the Laoshanya Formation red beds of Yangjiaping, South China:

1. The youngest component (A), previously identified as an overprint of Cretaceous age, is strongly correlated with bulk Fe concentration (in weight %) and several REEs (in ppm). In absolute terms, component A has a moderate positive relationship with rock density and a weak negative relationship with permeability, although these correlations are non-existent when the component is normalised by total magnetisation. These observations suggest the component was not formed as a result of fluid flow. Component A likely formed as a result of low-temperature oxidation of existing Fe-bearing grains, perhaps following uplift/exposure during the Cretaceous Long Normal Superchron.

2. Component B appears to be an mid-Paleozoic (460-420 Ma) remagnetisation which may be widespread in the Yangtze Craton. In Yangjiaping, the component is moderately correlated with alkali metals (particularly Bs, Ce, Rb and K), and with rock

density in both absolute and relative terms. Component B is not well-correlated with bulk Fe concentration, and has very weak relationships with permeability and porosity. This suggests that the formation of component B is also not related to fluid flow, although group B specimens appear to be more fractionated than the other component groups. Rather, the magnitude of component B is most closely related to mineral composition (as estimated by XRD), showing a strong negative correlation with the abundance of quartz and feldspar grains, and a strong positive correlation with the abundance of muscovite. This suggests that the remagnetisation is related to the abundance of phyllosilicates, and probably driven by the alteration of detrital clay minerals (e.g. smectite).

3. The primary component (C) is considered to be a depositional or early diagenetic signal from the mid-Neoproterozoic (809–804 Ma). The magnitude of the component has very-weak or non-existent correlations across all measured element concentrations and petrophysical properties, although it has a moderate negative relationship with rock density when normalised by total magnetisation. Component C has strong relationships with mineral composition in the exact opposite sense of component B, and a particularly strong relationship with the abundance of coarse quartz and feldspar grains. Specimens from the component C group have a very low permeability, similar to those from group B, but have the lowest connected porosity across all three groups. Preservation of component C could have been enabled by lower clay content and/or greater quartz cementation during early diagenesis.

Our observations highlight several novel techniques which could be used to identify remagnetisations in similar formations elsewhere. Namely, that the results of vector unmixing analyses (i.e. estimated component magnitudes) can be tested for correlations with geochemical, petrophysical and mineralogical measurements. In our case, the magnitude of the primary component is not (or very weakly, $r < 0.3$) correlated with any element concentration or petrophysical parameter when viewed in absolute terms. Therefore, researchers seeking primary DRMs from similar formations may be best served to target sandstones with coarser grain sizes and a higher proportion of quartz and feldspar grains (i.e. minimal clay content). To identify remagnetisations, component magnitudes could be tested for correlation (i.e. $r > 0.5$) with element concentrations, particularly Y, Fe, REE and heavy metals (e.g. Pb, Bi and Tl), and with alkali metals (e.g. Cs, Be, Rb and K). Strong positive correlations with rock density and/or the abundance of phyllosilicates (particularly muscovite) may also indicate remagnetisation.

Conclusions and perspectives

In this thesis, I sought to resolve complicated paleomagnetic signals observed in ca. 800 million year old sedimentary rocks from South China. I found that the signals do not reflect major tectonic upheaval (i.e. rapid TPW) or radical field geometry. Rather, the signals can be explained by widespread remagnetisation of the Yangtze Craton during a mid-Paleozoic orogeny (ca. 440 Ma). This orogenic event appears to have partially remagnetised pre-Paleozoic strata in South China.

In the first chapter, I developed a novel technique which allows paleomagnetists to better understand how multiple magnetisation components, with similar unblocking spectra, can combine. I show that conventional best-fitting line procedures, when applied to superimposed components, can produce spurious directions which deviate from the 'true' directions of end-members and obscure the paleomagnetic record. With accurate end-member selection, my method can be used to quantify absolute contributions from individual paleomagnetic components. I demonstrated the method with thermal demagnetisation data from various red beds in China. However, my unique approach can be broadly applied to all multicomponent problems in paleomagnetism and will be a useful tool for anyone trying to untangle complicated paleomagnetic signals.

I hope other paleomagnetists will use my method to test remagnetisation hypotheses across a range of other lithologies (e.g. volcanic rocks) and demagnetisation methods (e.g. AF demagnetisation). The MATLAB scripts I developed in Chapter 1 are freely available online: `https://github.com/lmu-magnetism/vector-unmixing`. Future work will involve converting the scripts to a Python format, e.g. a Jupyter notebook, that will be more accessible and easier to use. My scripts could also be optimised to run more efficiently; currently the inverse modelling uses 'brute force' to find the best solution. This means that the Monte Carlo simulations used to calculate uncertainties take $>$ ten minutes per specimen to run. More sophisticated inverse modelling techniques, such as Bayesian inversion, could also be implemented to make the scripts run faster.

In Chapter 2, I detailed a full paleomagnetic and rock magnetic investigation of the Laoshanya Formation in Yangjiaping (Hunan, China). I show that the Laoshanya Formation contains three paleomagnetic components which reside in different generations of hematite. The most dominant component appears in all samples and unblocks below 660 °C, which I interpret to be a Cretaceous overprint, common in South China. Two other components reside in only 15% of specimens and unblock up to 680 °C. One appears to be a primary (depositional) signal formed at ca. 807 Ma, while the other appears to be sec-

ondary magnetisation formed during the Late Ordovician (460–420 Ma), as the paleopole derived from the latter overlaps with several Ordovician paleopoles. Interplay between these two high-temperature components has produced an unusual pattern of directions which alternates between steep, dual-polarity directions and shallower, single-polarity directions. The primary component places South China in a tectonically stable, high-latitude position between 809–804 Ma, and supports a conventional GAD field for this time period.

The prevalence of the Ordovician signal appears to be related to the abundance of fine-grained material, e.g. iron-bearing clays, which were likely altered during a low-grade tectono-thermal event (< 260 °C). Regional comparisons suggest that remagnetisation may be complicating paleomagnetic signals from other pre-Ordovician strata on the Yangtze Craton. Specifically, several studies from 820–800 Ma report paleopoles which are rotated some 45–90° (counter-clockwise from the Laoshanya paleopole). However, these paleopoles overlap with Ordovician paleopoles when plotted in the same hemisphere, implying that they may overprinted.

Further work is needed to investigate the possibility of remagnetisation in other paleomagnetic studies from South China in the Neoproterozoic. It is difficult to discern at the level of detail as reported in journal articles, but several studies appear to also contain paleomagnetic directions derived from samples that span different lithologies, i.e. mudstones and sandstones. My work shows that subtle changes in lithology can have a significant impact on the fidelity of the magnetic record, and these changes must be afforded careful consideration. Although somewhat unsettling, I hope my findings can help to identify similar problems elsewhere. I view the Laoshanya Formation as a kind of 'Rosetta Stone' for rapid TPW in the Neoproterozoic, where the presence of two signals in the very same outcrop allows us to decode them by direct comparison.

In the third chapter, I show how this decoding could be performed, at least for sedimentary rocks of a similar age in South China. Using the vector unmixing method from Chapter 1, and the results of geochemical, mineralogical and petrophysical experiments, I tested for correlations between the magnitudes of the components in each sample and other quantities (e.g. element concentrations). I show that the the Cretaceous component from the Laoshanya Formation is correlated with concentrations of iron as well as various rare-earth elements and heavy metals. The Ordovician component correlates with alkali concentrations (Cs, Be, Rb and K), as well as rock density and the abundance of phyllosilicates (particularly muscovite). The primary component does not correlate with any element concentrations, but does have a strong relationship with the abundance of quartz and feldspar grains, and the lack of phyllosilicates. There are no strong relationships between any component and permeability or connected porosity, suggesting that external fluids did not a have a significant role in the formation of secondary components. The strength of each overprint was therefore probably controlled by the relative abundance of detrital material (i.e. clay content) available for alteration.

My approach in Chapter 3 could be useful for testing remagnetisation hypotheses in other hematite-bearing sedimentary rocks. Vector unmixing is something that can be done retrospectively, as long as the original (specimen-level) demagnetisation data are available. Unfortunately, geochemical and petrophysical data are not routinely collected or reported

during paleomagnetic studies, so this would require significant additional work as well as fresh samples. However, we showed that rock density could be a 'low-tech' indicator of remagnetisation in red beds. Specimens are often weighed before demagnetisation in order to mass-normalise the data. If specimen volumes are consistent (or were directly measured), bulk density could be tested for correlation with component magnitudes to identify remagnetisation, assuming the effects we see are not unique to the Laoshanya Formation.

I believe that the novel techniques I applied in this thesis could be broadly used to investigate remagnetisation (and TPW) hypotheses elsewhere. Remagnetisation is still an obscure phenomenon and I expect that there are significant insights to be gained through application of these methods in other locations and periods of the geologic record. To conclude a chapter on TPW in the Encyclopedia of Geomagnetism and Paleomagnetism (Gubbins and Herrero-Bervera, 2007), Vincent Courtillot describes a 'somewhat bothering feeling' that TPW will remain an elusive geophysical problem. I admit that I experienced a similar feeling many times in the early stages of this project. Overall, I hope that my work in this thesis is a positive step towards resolving some baffling paleomagnetic phenomena, and will help shine a light on Earth's enigmatic Neoproterozoic history.

Appendix A

Chapter 1 supplementary material

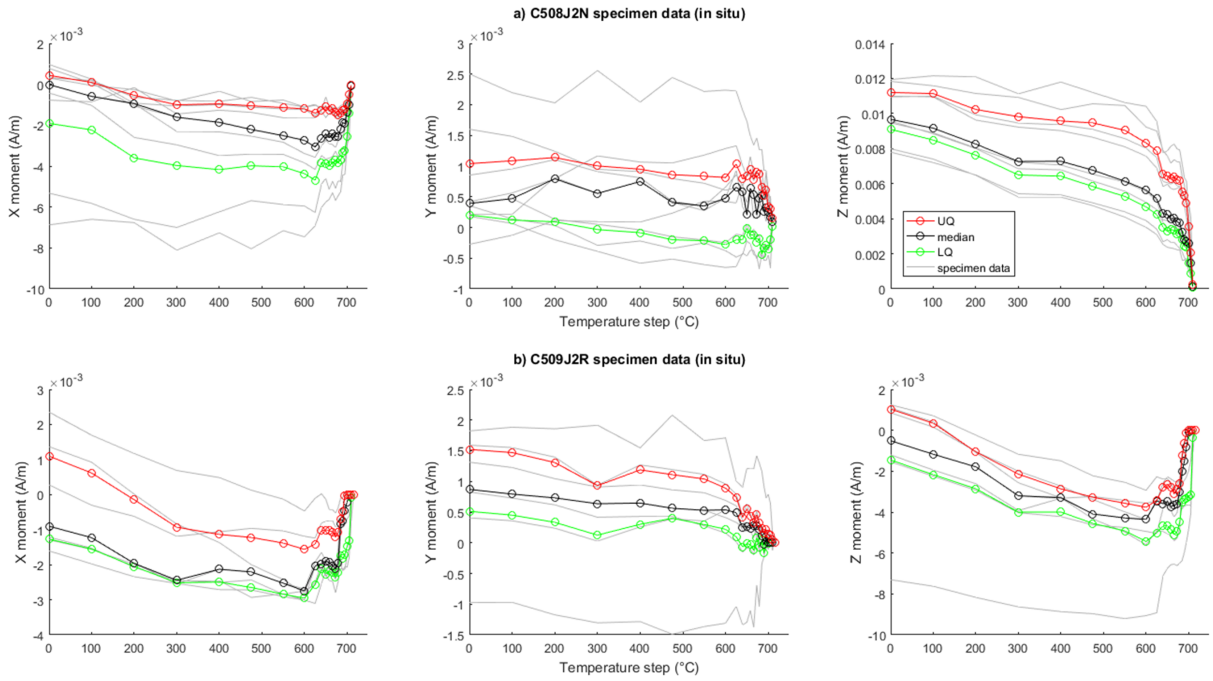

Figure A.1: (a and b) Compiled profiles for the Middle Jurassic red beds from Gilder and Courtillot (1997). Nine specimens from sites C508 (normal polarity) and seven specimens from site C509 (reversed polarity) were selected as representative specimens. The median moment vectors across all demagnetisation steps for all specimens were calculated with lower (25%) and upper (75%) quartiles (LQ and UQ). All data are shown in geographic (in situ) coordinates and volume-normalised remanence (A/m).

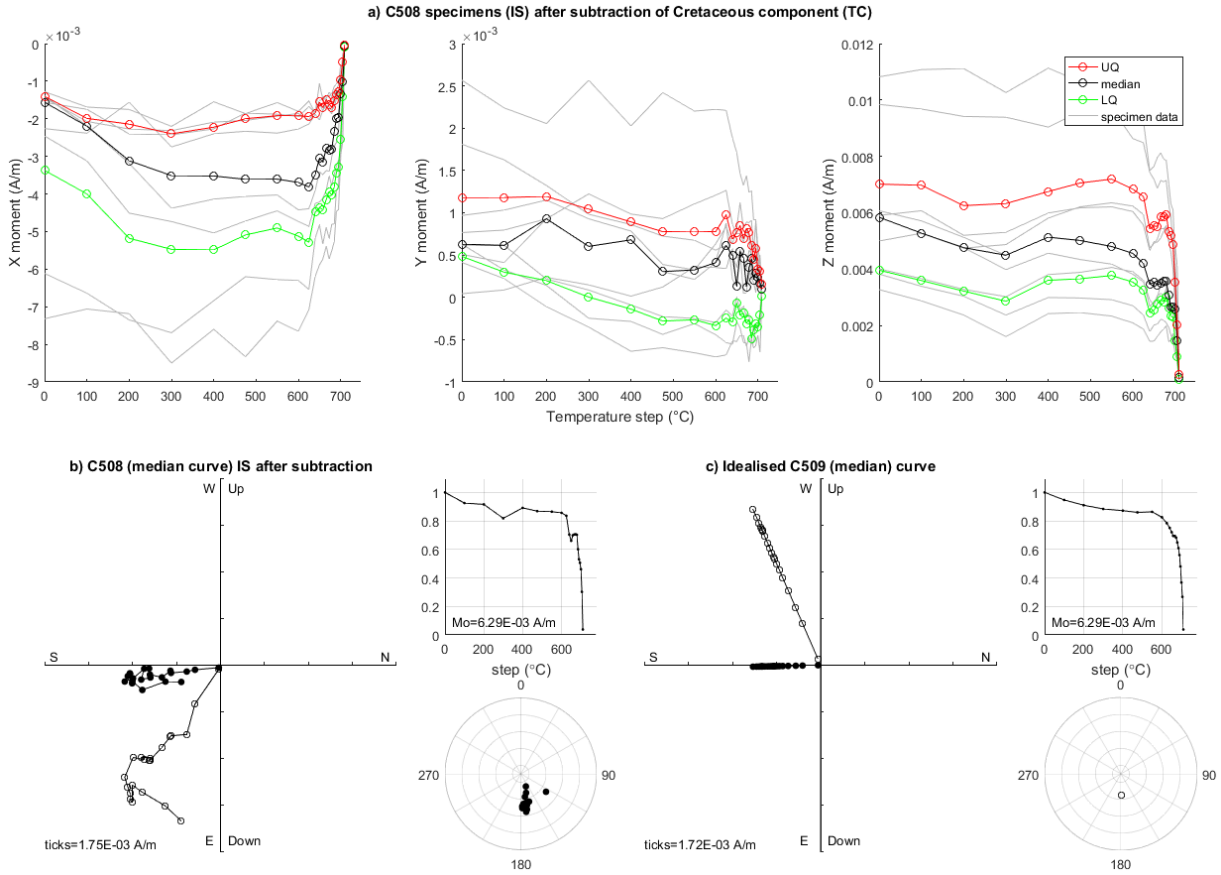

Figure A.2: (a) Median curves obtained with specimen data and (b) end-member profile for Jurassic site C508 (IS) after variable subtraction of Cretaceous (TC) component from specimen demagnetisation data. In this case, demagnetisation spectra for each specimen were corrected by variable subtraction of an idealised Cretaceous curve (Fig. 1.7c) using a κ-maximising algorithm. (c) an idealised curve produced for modelling site C509 by smoothing the C508 end-member profile and applying a uniform direction $Dg = 178.8°$ and $Ig = -65.3°$, obtained by PCA for site C509 (Gilder and Courtillot, 1997). All results are expressed in geographic coordinates and volume-normalised remanence (A/m).

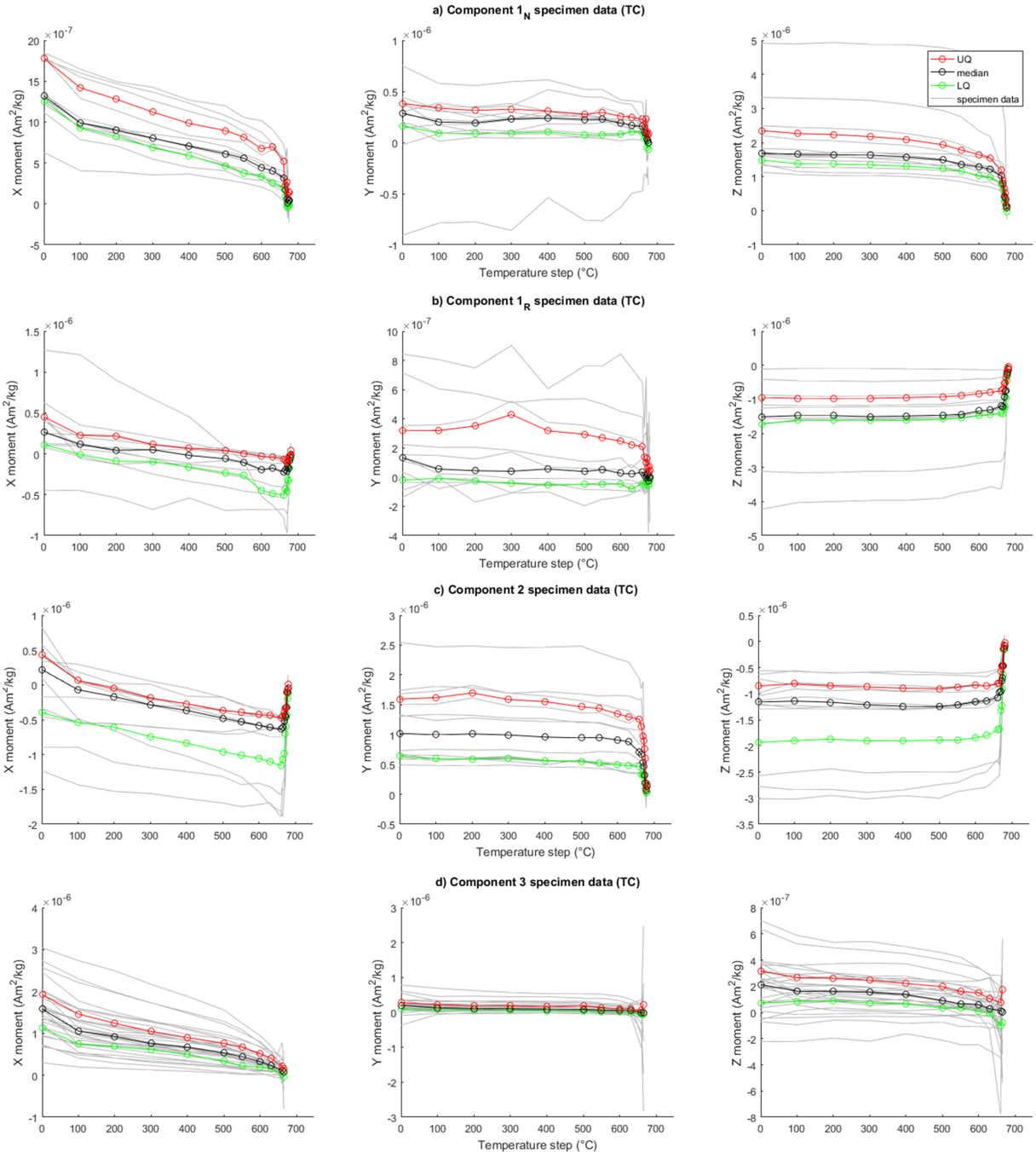

Figure A.3: Compiled median curves for representative specimens from the Yangjiaping section (Tonti-Filippini et al., 2021) used to define components (a) $C1_N$, (b) $C1_R$, (c) C2 and (d) C3 in Figs. 1.11(a, c, e and g). All data are shown in stratigraphic (tilt-corrected) coordinates and mass-normalised remanence (Am^2/kg).

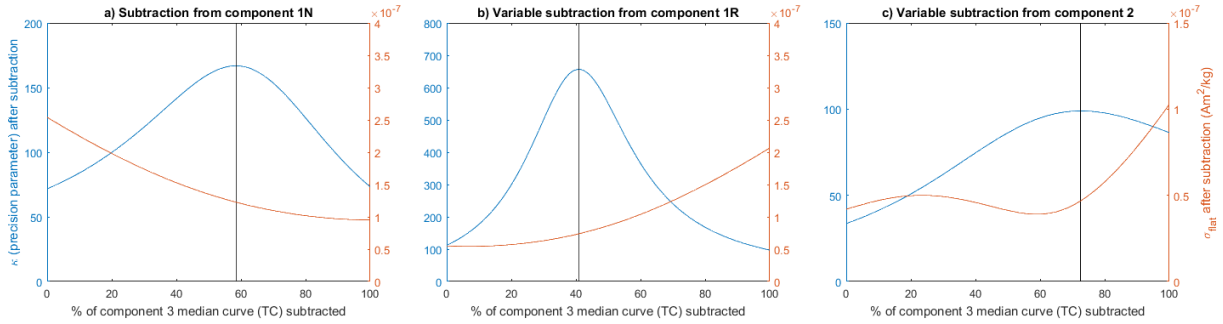

Figure A.4: Optimal solutions for the subtraction of the C3 overprint (Fig. 1.11g) from Yangjiaping components (a) $C1_N$, (b) $C1_R$ and (c) C2 in Fig. 1.11(a, c and e). The highest κ was used to determine best-fitting solutions with respective contributions of 58.5%, 41% and 72.5% and define the end-member curves in Fig. 1.11(b, d and f). σ_{flat} is the flatness of the output remanence curves across the first eight demagnetisation steps (0–600 °C), which was not used in this case as the κ-maximising algorithm functions well.

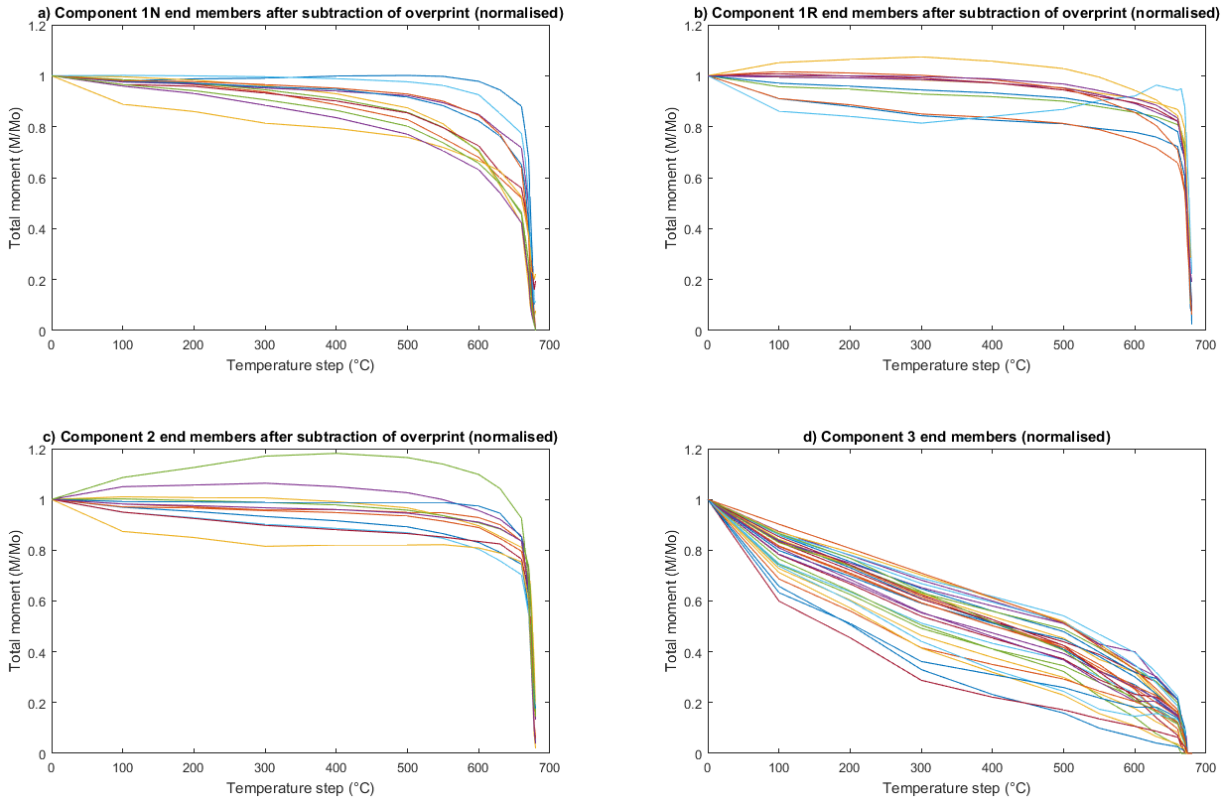

Figure A.5: Normalised and smoothed thermal remanence curves for selected Yangjiaping end member specimens after individual subtraction of the C3 overprint. (a) $C1_N$ end member curves were derived using the σ_{flat}-minimising algorithm. (b and c) $C1_R$ and C2 end member curves were derived using the κ-maximising algorithm. (d) No subtraction was applied to C3 end members (raw specimen curves).

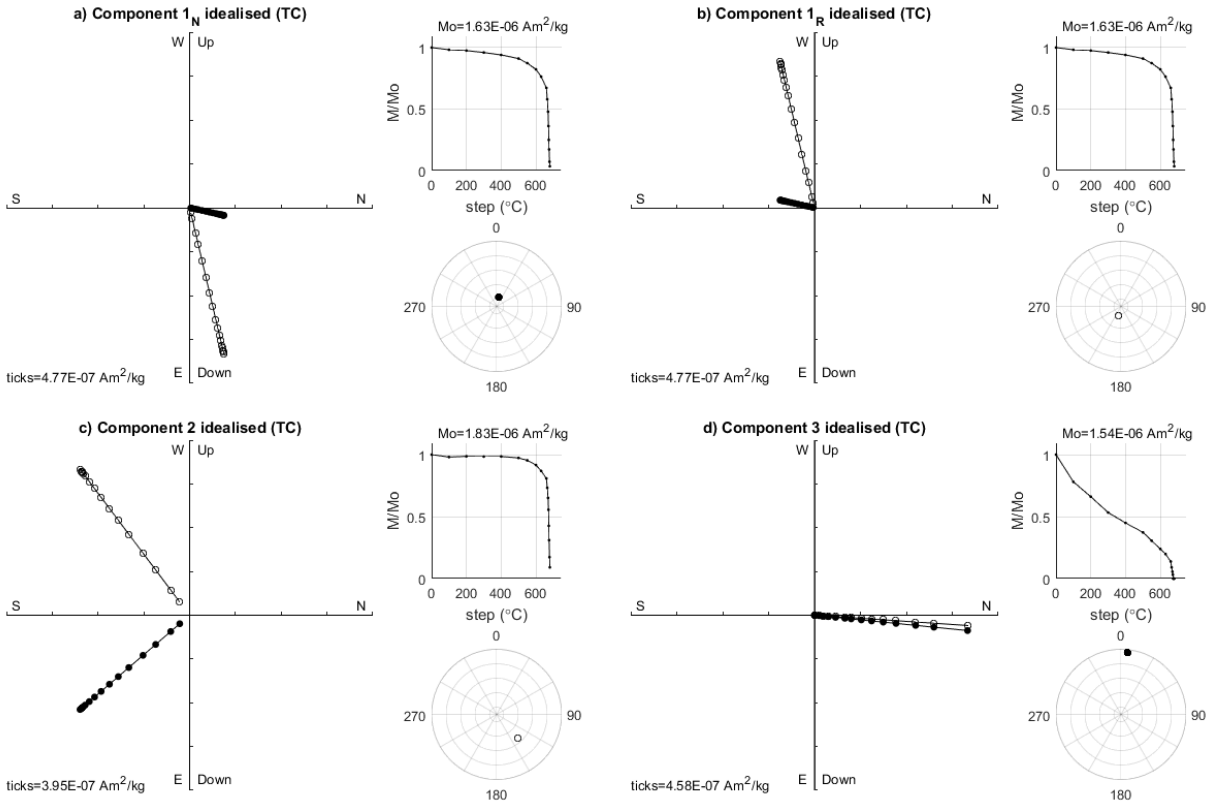

Figure A.6: Idealised end-member curves used for inverse modelling of component contributions to specimens from the Yangjiaping section (Tonti-Filippini et al., 2021). (a) Idealised component $C1_N$ was compiled by combining and smoothing median curves for component $C1_N$ and $C1_R$ after variable subtraction (Figs. 1.11b and d) and applying a direction (obtained from PCA) of $Ds = 13°$ and $Is = 77°$. (b) Similarly, idealised component $C1_R$ has an applied direction from PCA of $Ds = 193°$ and $Is = -77°$. (c) Idealised component C2 was created by applying a smoothing function to the median curve after variable subtraction (Fig. 1.11f) and applying a PCA-obtained direction of $Ds = 138°$ and $Is = -46°$. (d) Idealised component C3 was obtained after applying a smoothing function to the median curve in Fig. 1.11(g) and PCA directions of $Ds = 6°$ and $Is = 4°$.

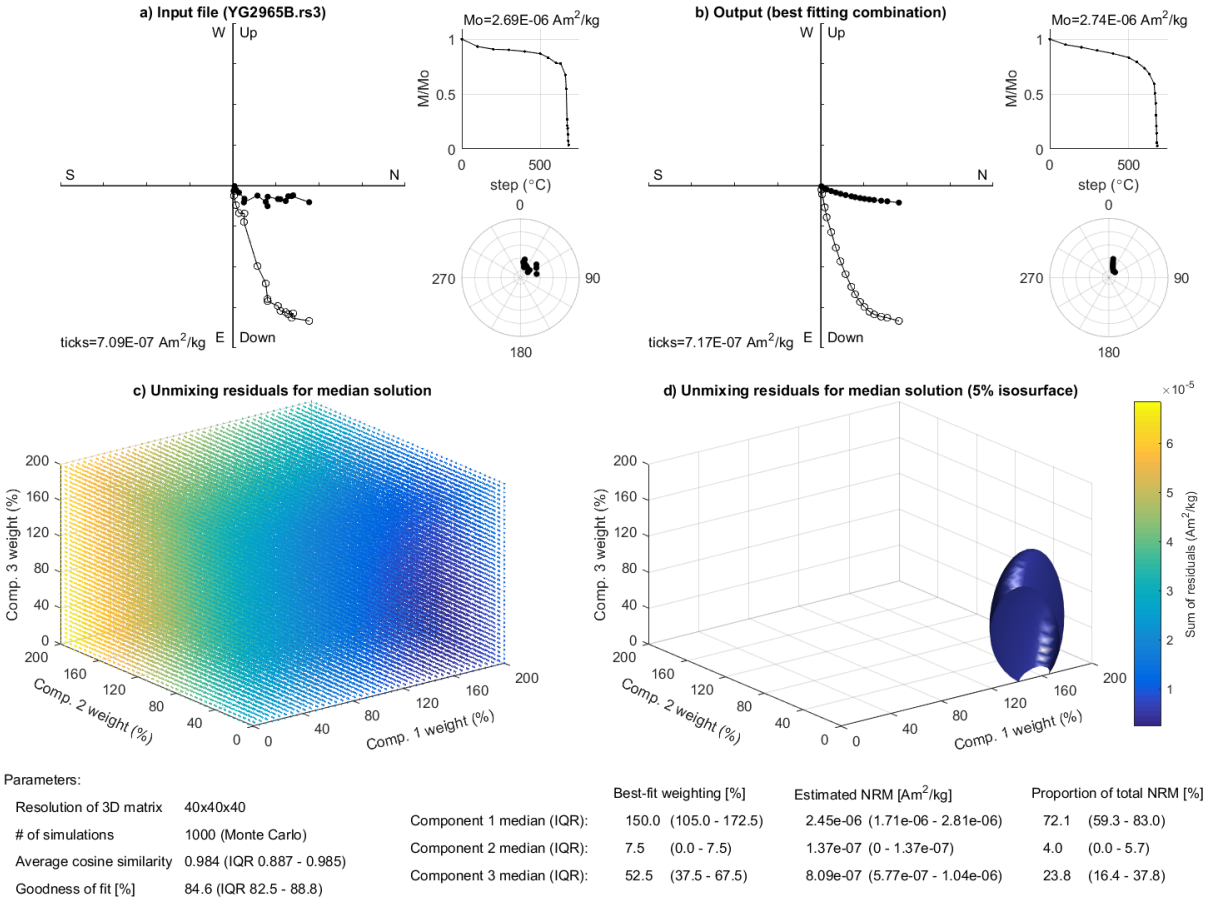

Parameters:

Resolution of 3D matrix	40x40x40
# of simulations	1000 (Monte Carlo)
Average cosine similarity	0.984 (IQR 0.887 - 0.985)
Goodness of fit [%]	84.6 (IQR 82.5 - 88.8)

	Best-fit weighting [%]		Estimated NRM [Am²/kg]		Proportion of total NRM [%]	
Component 1 median (IQR):	150.0	(105.0 - 172.5)	2.45e-06	(1.71e-06 - 2.81e-06)	72.1	(59.3 - 83.0)
Component 2 median (IQR):	7.5	(0.0 - 7.5)	1.37e-07	(0 - 1.37e-07)	4.0	(0.0 - 5.7)
Component 3 median (IQR):	52.5	(37.5 - 67.5)	8.09e-07	(5.77e-07 - 1.04e-06)	23.8	(16.4 - 37.8)

Figure A.7: Three-component unmixing result for Yangjiaping specimen YG2965B. Despite the apparent noise in the input remanence file (a), the unmixing function can accurately resolve input components C1-3 with a median GOF of 84.6% *and ACS of 0.984.*

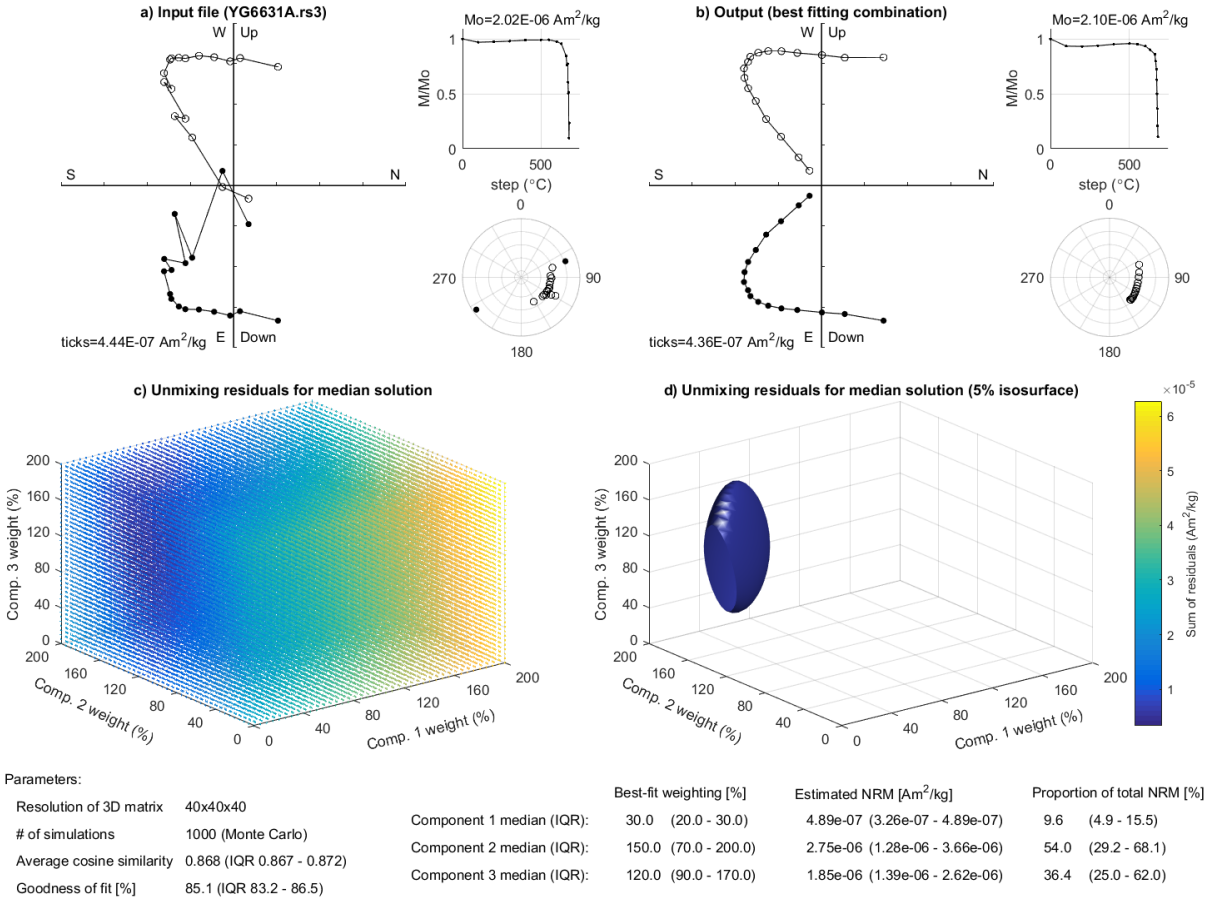

Parameters:

Resolution of 3D matrix	40x40x40
# of simulations	1000 (Monte Carlo)
Average cosine similarity	0.868 (IQR 0.867 - 0.872)
Goodness of fit [%]	85.1 (IQR 83.2 - 86.5)

	Best-fit weighting [%]	Estimated NRM [Am²/kg]	Proportion of total NRM [%]
Component 1 median (IQR):	30.0 (20.0 - 30.0)	4.89e-07 (3.26e-07 - 4.89e-07)	9.6 (4.9 - 15.5)
Component 2 median (IQR):	150.0 (70.0 - 200.0)	2.75e-06 (1.28e-06 - 3.66e-06)	54.0 (29.2 - 68.1)
Component 3 median (IQR):	120.0 (90.0 - 170.0)	1.85e-06 (1.39e-06 - 2.62e-06)	36.4 (25.0 - 62.0)

Figure A.8: Three-component unmixing result for Yangjiaping specimen YG6631A. The unmixing function can accurately resolve the input components C1-3 with a median GOF of 85.1% *and ACS of 0.868.*

Appendix B

Chapter 2 supplementary material

B.1 Additional figures and tables

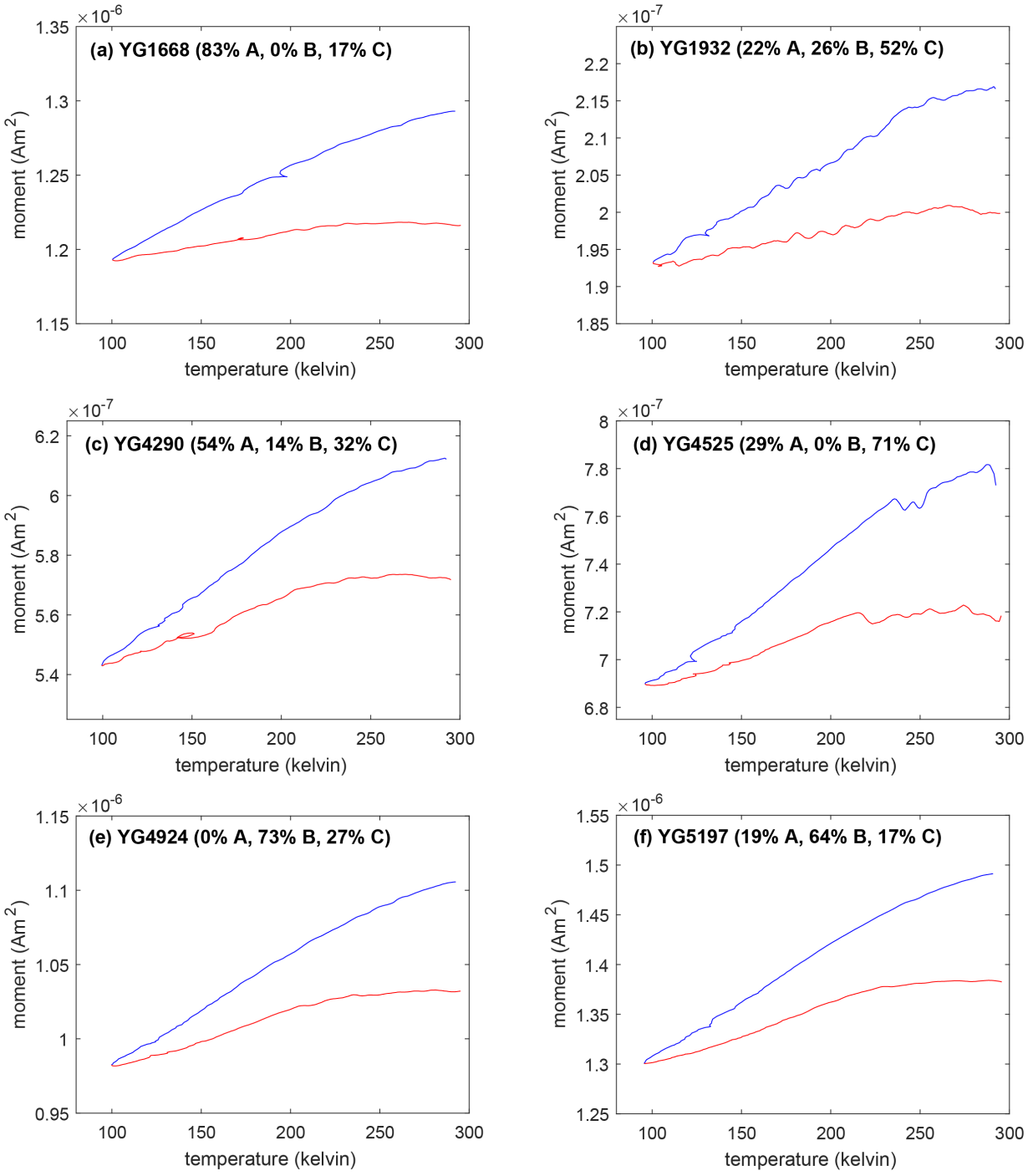

Figure B.1: Examples of low temperature remanence curves for component groups A, (a) and (c), B (e) and (f), and C, (b) and (d). Experiments were performed on crushed specimens in air between room temperature (293 K) and -173 °C (100 K). Blue lines are cooling curves and red lines are warming curves. All measured specimens show neither a Morin nor a Verwey transition.

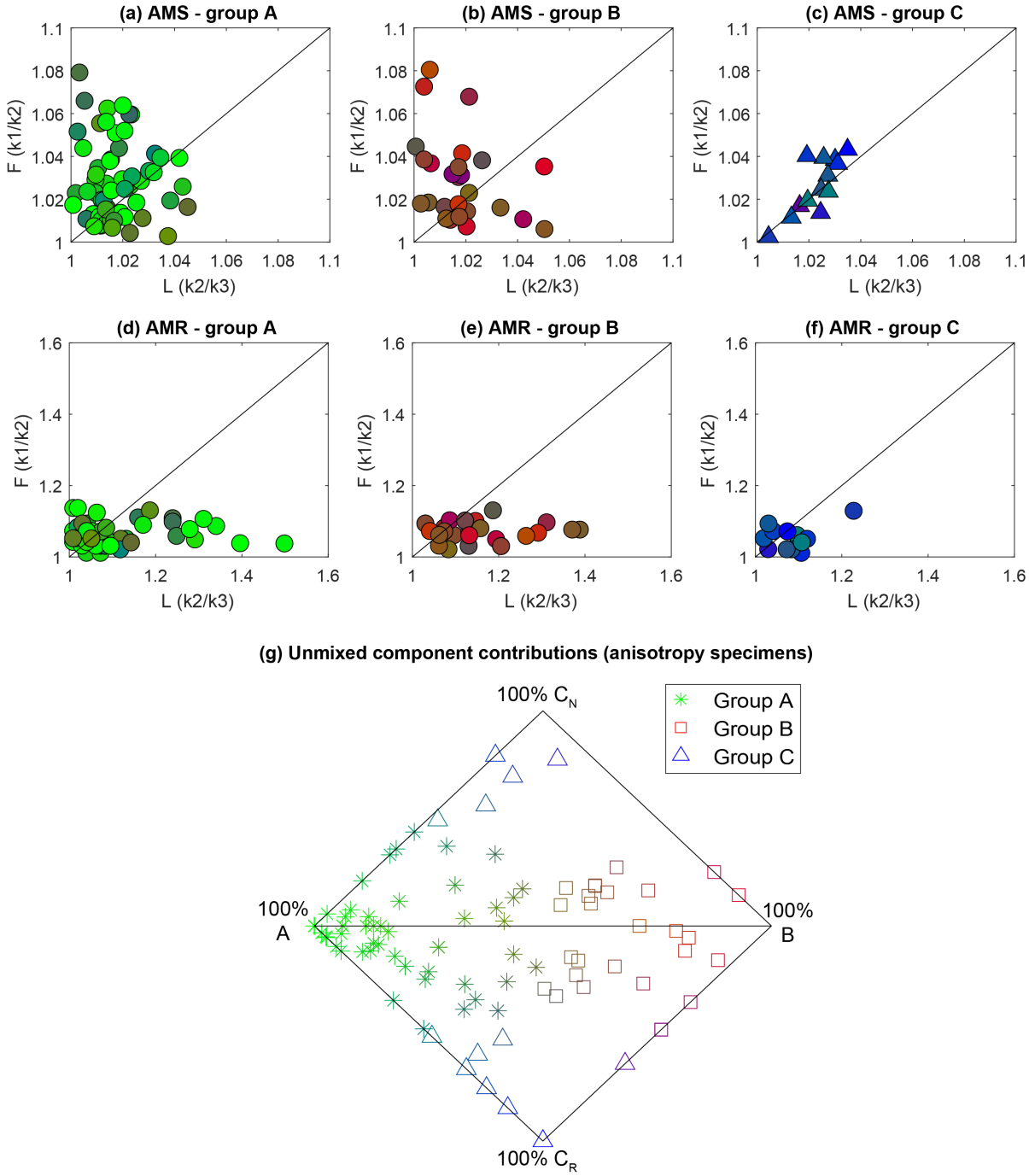

Figure B.2: Flinn (1962) diagrams by component group for AMS (a-c) and AMR (d-f), with points shaded by component contributions estimated from vector unmixing analyses (g). Note the significant difference in axes on Flinn diagrams between AMS and AMR.

Table B.1: Tonian poles for the SCB (820–800 Ma). ID' = pole derived with shallowing correction. ID = recalculated pole (see text). A_{95} = radius of 95% confidence circle for mean pole. dp and dm = semi-axes of the 95% confidence ellipse. f = flattening factor for shallowing correction (f value, as indicated). R following Meert et al. (2020).*

Formation	ID	age (Ma)	site lat.	site lon.	pole lat.	pole lon.	A_{95} (dp/dm)	f	criteria	R	†age ref./+pole ref.
Xiaofeng dykes	XF	821 ± 0.2	31.0	111.2	13.5	91.0	10.5/11.3	-	1100100	3	†Wang et al. (2016b)/+Li et al. (2004)
	XF*	802 ± 10			26.1	82.1	14.0/15.2	-			†Li et al. (2004)/+Jing et al. (2020)
Yanbian dykes	YB1	824 ± 6	26.9	101.5	45.1	130.4	19.0	-	1110001	4	†+Niu et al. (2016)
	YB2	806 ± 8	26.9	101.5	14.1	32.5	20.4	-	1011000	3	†+Niu et al. (2016)
Madiyi Fm.	MD	805 ± 1	27.5	109.6	35.3	67.9	4.7/5.5	1	1010010	3	†Park et al. (2021)/+Xian et al. (2020)
	MD'				35.0	75.0	5.2/5.8	0.8			+Park et al. (2021)/(recalculated)
Chengjiang Fm. (recalculated)	CJ1	800 ± 8.4	25.2	102.4	32.8	56.3	8.1/8.6	1	1011010	4	†+Jing et al. (2020)
	CJ1'				30.0	67.4	11.0/12.3	0.8			+Park et al. (2021)/(recalculated)
	CJ3	785 ± 12	25.2	102.4	22.6	33.2	9.5/14.8	1	1010000	2	†+Jing et al. (2020)
Xiajiang Gp.	XJ	816–810	27.9	108.8	50.7	100.0	12.3	1	1011011	5	+Park et al. (2021)/(recalculated)
	XJ'				47.5	102.0	12.5/13.2	0.8			†+Park et al. (2021)/(recalculated)
Laoshanya Fm.	LS-C*	807.5 ± 0.2	30.0	110.7	51.1	127.2	4.9/5.2	0.8	1110011	5	This study (tilt-corrected)

Table B.2: Ediacaran to Silurian (635 – 420 Ma) poles from the SCB considered in this study.

Formation (locality)	ID	age	site lat.	site lon.	pole lat.	pole lon.	A_{95} (dp/dm)	references
(Shiqian, Guizhou)	SQ	S	27.5	108.0	14.9	196.1	5.1	Huang et al. (2018, 2000)
(Xiushan, Sichuan)	XS	S	28.5	109.0	6.8	195.7	5.4	Huang et al. (2018); Opdyke et al. (1987)
Pagoda (Wangcang)	PG	O	32.4	106.3	-45.8	191.3	2.4/4.2	Han et al. (2015); Zhang et al. (2015a)
Baota (Shanxi)	BS	O	-	-	-29.5	227.0	6.3	Zhang et al. (2015a, 2012)
Hongshiya (Yunnan)	HF	O	25.6	102.6	-38.9	235.7	16.9	Fang et al. (1990); Huang et al. (2018)
Hongshiya (Yunnan)	HG	O	25.6	102.5	-48.1	229.4	4.4	Gao et al. (2018)
Duoposi (Wangcang)	DW	C	32.1	106.2	-39.5	185.1	4.4/8.3	Bai et al. (1998); Huang et al. (2018)
Duoposi (Guangyuan)	DG	C	32.4	106.3	-51.3	166.0	4.4/8.6	Huang et al. (2018); Yang et al. (2004)
Doushantuo (Jiulongwan)	DJ	Ed	30.8	111.1	23.9	187.0	1.8/3.0	Zhang et al. (2015a)
Doushantuo (Yangjiaping)	DY	Ed	30.0	110.7	0.6	196.9	4.5/9.0	Macouin et al. (2004)
Laoshanya (Yangjiaping)	LS-B	O?	30.0	110.7	-49.8	209.9	3.1/4.8	This study (tilt-corrected)

S = Silurian, O = Ordovician, C = Cambrian, Ed = Ediacaran

Table B.3: Site directions for component C from the Laoshanya Formation. Specimens were grouped into stratigraphic units of n = 8-12 for comparison with other studies. n/N = number of specimens/sites. Dg/Ig and Ds/Is = geographic (in situ) and stratigraphic (tilt-corrected) declination/inclination. κ and α_{95} are the precision parameter and 95% confidence circle (Fisher, 1953).

site	height (m)	n	D_g	I_g	D_s	I_s	κ	α_{95}
C1	02.2 - 25.8	12	337.2	-46.6	185.2	-74.3	62.6	5.5
C2	29.1 - 32.8	8	146.3	39.4	43.8	73.1	45.6	8.3
C3	36.4 - 38.8	8	154.2	31.3	76.4	80.8	25.8	11.1
C4	44.9 - 46.6	11	146.6	45.5	26.3	70.4	71.8	5.4
C5	46.6 - 47.8	11	146.1	49.9	17.8	67.3	54.9	6.2
C6	47.8 - 48.9	11	144.6	47.8	23.5	67.9	92.5	4.8
C7	49.4 - 52.1	10	152.3	39.4	35.7	77.3	51.8	6.8
C8	52.1 - 84.1	10	327.2	-33.5	244.7	-75.0	15.4	12.7
mean		(N=8)	149.4	41.7	32.5	74.2	112.6	5.2

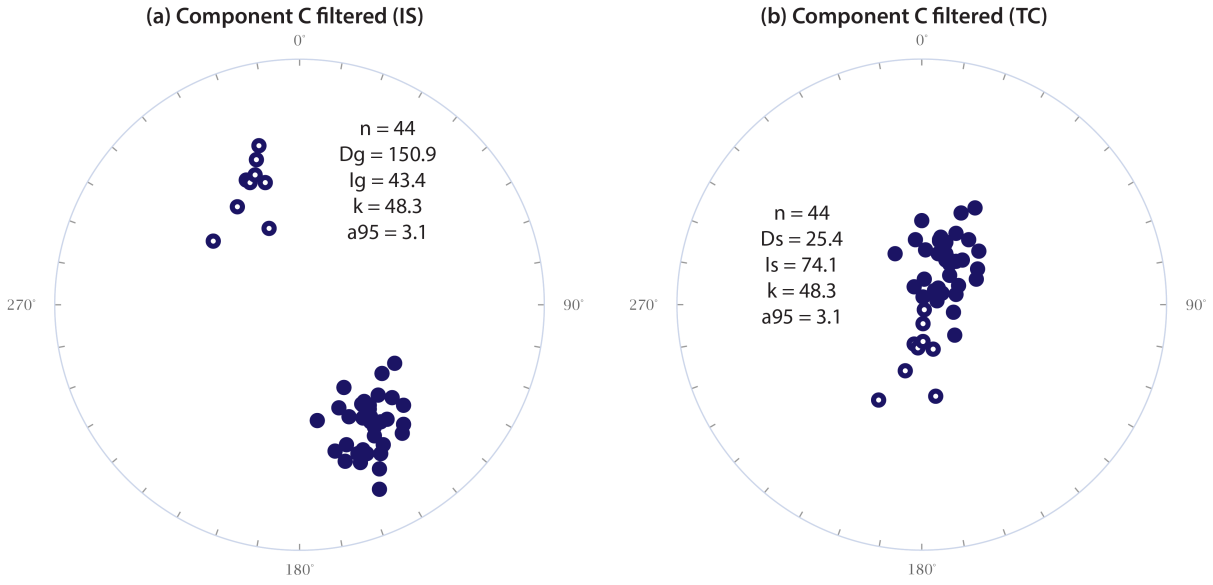

Figure B.3: Component C specimen directions after filtering for results which decay to the origin on a Zijderveld plot and have MAD $< 10°$ in (a) geographic (IS) and (b) stratigraphic (TC) coordinates. The directions pass a reversal test with a 'B' classification (McFadden and McElhinny, 1990).

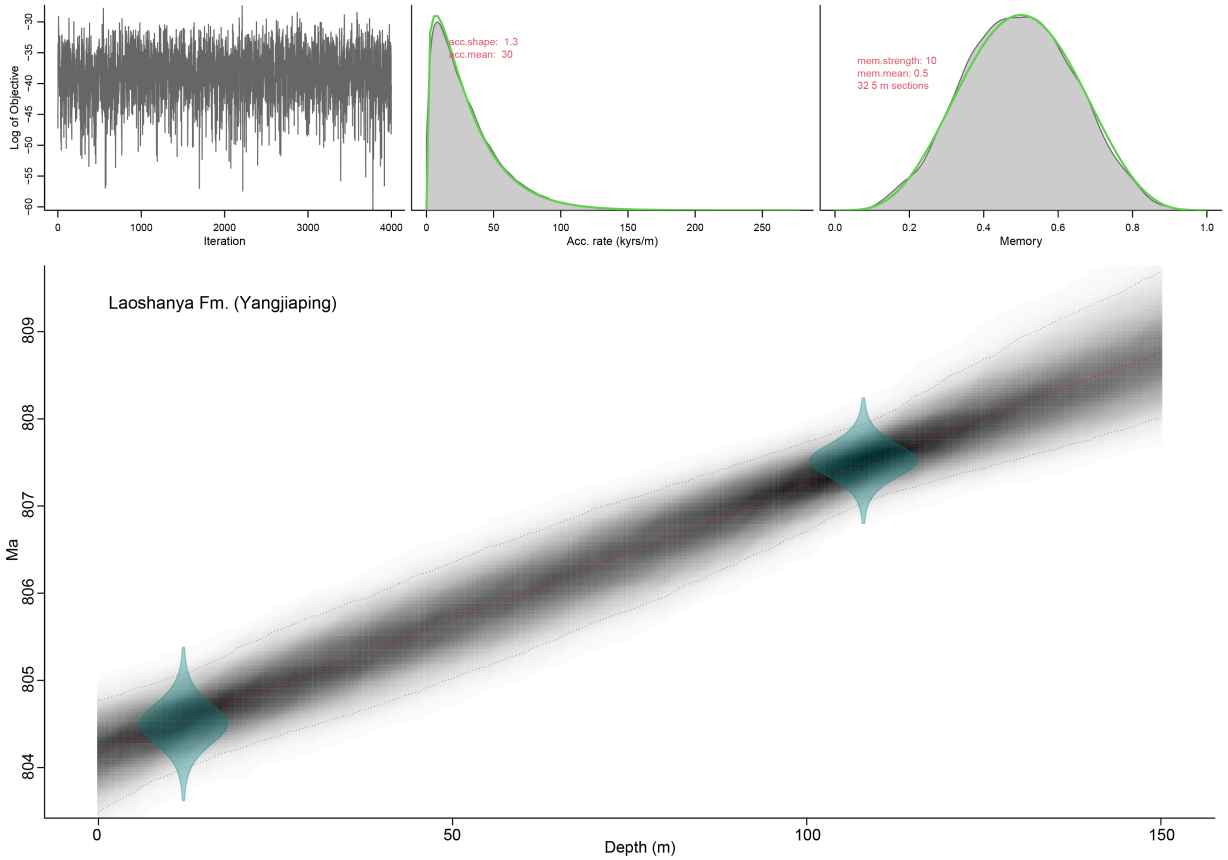

Figure B.4: Age-depth model for the Laoshanya Formation in Yangjiaping, based on CA-ID-TIMS dating of two intercalated tuff beds, calculated using the approach of Blaauw and Christeny (2011). With linear extrapolation, assuming a constant accumulation rate, the results suggest that the formation was deposited between 808.7 [median, 95% range = 809.6 – 808.0] and 804.2 [median, 95% range = 804.7 – 803.5] Ma.

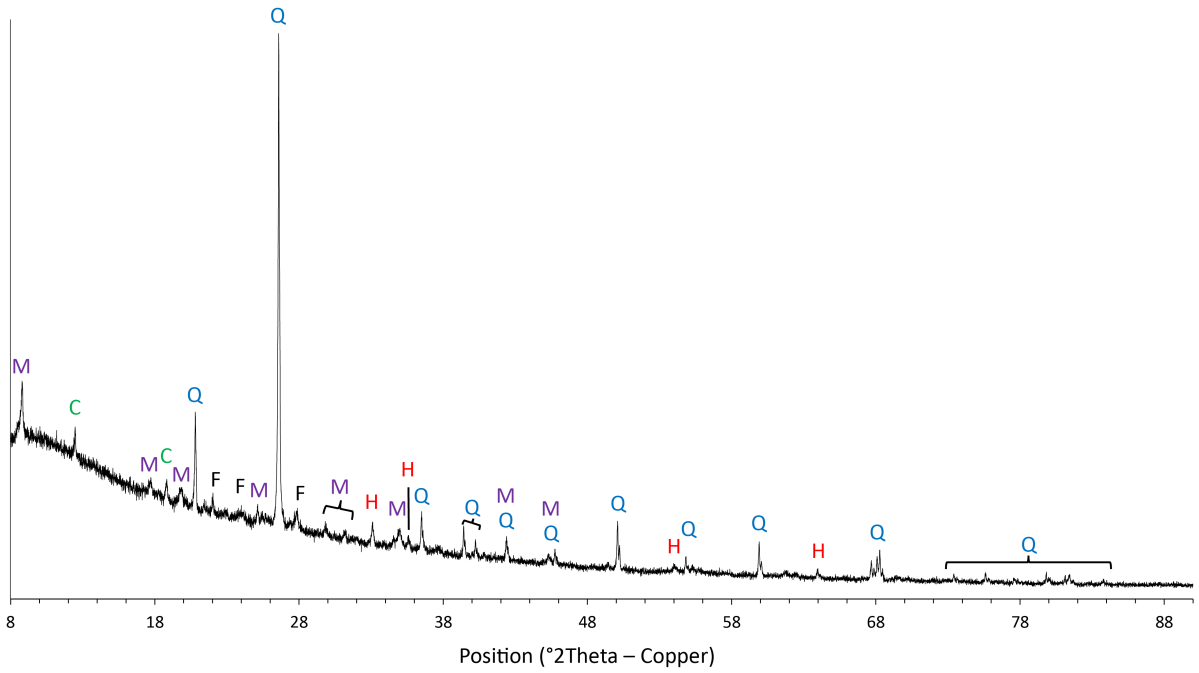

Figure B.5: Typical diffractogram of Laoshanya rock powder (sample YG1120) highlighting the location of diffraction peaks from the different minerals. Abbreviations for the phases are: Q: quartz; M: muscovite; F: feldspar; C: chlorite; H: hematite.

Table B.4: Shallowing correction calculations for 820–800 Ma SCB poles. In this table we test which flattening factor (f) brings the paleomagnetic inclinations from sedimentary (sed.) poles into closest agreement with those from igneous (ign.) poles. In this analysis we assume that all 820-800 Ma poles are approximately coeval and vertical axis rotations are permitted (as in Scenario 1). A factor of f=0.8 produces the lowest standard deviation (stdev) across all inclinations.

	f value:	1.00	0.95	0.90	0.85	0.80	0.75	0.70	0.65	0.60
poles		absolute inclination values (°)								
YB1	ign.	72.6	72.6	72.6	72.6	72.6	72.6	72.6	72.6	72.6
XF	ign.	76.6	76.6	76.6	76.6	76.6	76.6	76.6	76.6	76.6
XJ	sed.	77.0	77.6	78.3	78.9	79.5	80.2	80.8	81.5	82.1
MD	sed.	69.9	70.8	71.8	72.7	73.7	74.7	75.6	76.6	77.6
CJ1	sed.	69.2	70.2	71.1	72.1	73.1	74.1	75.1	76.1	77.2
LS-C*	sed.	74.1	74.9	75.6	76.4	77.2	77.9	78.7	79.5	80.3
	median	73.4	73.7	74.1	74.6	75.1	75.6	76.1	76.6	77.4
	stdev	3.3	3.1	2.9	2.8	2.7	2.8	2.9	3.1	3.3

B.2 Review of Tonian poles for the SCB (820–800 Ma)

Here we present a review of all known 820 – 800 Ma paleopoles for South China. Each pole is assessed using the updated 'R' quality criteria of Meert et al. (2020). A summary of the assessment is given in Table B.1.

Xiaofeng dykes (XF)

Li et al. (2004) reported a pole from the Xiaofeng dykes (XF), which were SHRIMP dated at 802 ± 10 Ma. Wang et al. (2016b) redated the dykes to 821.6 ± 0.2 Ma with laser ablation (LA-) MC-ICP-MS. However, Jing et al. (2020) noted that Wang et al. (2016b) dated material from felsic dykes which were cut by younger mafic dykes, while the paleomagnetic data were obtained mainly from mafic dykes, so the older age of Wang et al. (2016b) may not relate to the same rocks used for paleomagnetism. Jing et al. (2020) observed two groups of directions within the dykes, coming from opposite sides of a fault. They recalculated a pole after excluding one subgroup deemed to be locally rotated. Therefore, we prefer the younger age of 802 ± 10 Ma (Li et al., 2004) and the recalculated (XF*) pole of Jing et al. (2020). The pole, when reversed, lies close to Early Paleozoic poles.

Yanbian dykes (YB)

Niu et al. (2016) presented poles from two groups of the mafic Yanbian dykes, dated at 824 ± 6 Ma (YB1) and 806 ± 8 Ma (YB2) via secondary ion mass spectrometry (SIMS). A vertical axis rotation of 5° was subtracted, based on paleomagnetic data from nearby Pliocene rocks. Park et al. (2021) excluded both poles from their compilation, observing that no tilt correction was applied to most of the dykes (despite that several dip up to 43° from vertical) and that the dykes may have experienced vertical axis rotation prior to the Pliocene.

Madiyi Formation (MD)

Xian et al. (2020) reported a pole from Madiyi silty mudstones, initially dated with SIMS at 802 ± 6 Ma, but redated to 805 ± 1 Ma by CA-ID-TIMS (Park et al., 2021). The data in Xian et al. (2020) had no independent field tests to constrain the relative age of magnetization. A flattening factor of 0.6 was applied to correct for inclination shallowing, with no justification (E/I or anisotropy not measured/calculated). The original pole (uncorrected for inclination shallowing) lies close to Early Paleozoic poles when plotted in the southern hemisphere. We note that the antipodal directions passed a reversal test, but only when applied on a subset of directions.

Chengjiang Formation (CJ)

Jing et al. (2020) reported two poles (CJ1 and CJ3) from Chengjiang Formation red sandstones, dated by SHRIMP at 800 ± 8 Ma (CJ1) and 785 ± 12 Ma (CJ3). The Chengjiang Formation was correlated with the Wuqiangxi Formation, which overlies the Madiyi Formation (Jiang et al., 2012). Thermal demagnetization data passed a fold test at 99% confidence limits (Jing et al., 2020). Park et al. (2021) recalculated an inclination corrected pole by applying a flattening factor of 0.6 with no justification. The CJ1 pole of Jing et al. (2020) overlaps with younger Ordovician poles.

Xiajiang Group (XJ)

Park et al. (2021) reported several poles from fine-grained siliclastic sediments of the Xiajiang Group as well as high-precision U-Pb CA-ID-TIMS ages from interbedded tuffs. However, there was limited assessment of remanence carriers and no assessment of inclination shallowing. The pole reported by Park et al. (2021) is a study mean which averages data across several sites, with ages spanning more than 11 Myr (815.7 – 804.6 Ma), and there are significant directional differences between sites.

Laoshanya Formation (LS)

We define a new Tonian pole (LS-C) based on the tilt-corrected mean direction of group C specimens of the Laoshanya Formation. The pole is statistically robust and passes a reversal test when filtered for the highest quality directions (linear decay to origin, MAD $< 10°$, n = 44). The pole is unique from any younger poles. We were unable to obtain independent field (fold, contact or conglomerate) tests, but our observations described in the main text suggest that the paleomagnetic signal is primary. Therefore, we assign the pole an age of 807.5 ± 0.2 Ma.

Ediacaran to Silurian poles

In Table B.2, we list Ediacaran to Silurian poles for the SCB from Huang et al. (2018), as well as Ediacaran poles of Macouin et al. (2004) and Zhang et al. (2015a), and Ordovician poles from the Baota (Zhang et al., 2012) and Hongshiya (Gao et al., 2018) Formations. All poles are derived in tilt-corrected coordinates.

References

Abrajevitch, A. and Van der Voo, R. (2010). Incompatible Ediacaran paleomagnetic directions suggest an equatorial geomagnetic dipole hypothesis. *Earth and Planetary Science Letters*, 293(1-2):164–170.

Alken, P., Thébault, E., Beggan, C. D., Amit, H., Aubert, J., Baerenzung, J., Bondar, T. N., Brown, W. J., Califf, S., Chambodut, A., Chulliat, A., Cox, G. A., Finlay, C. C., Fournier, A., Gillet, N., Grayver, A., Hammer, M. D., Holschneider, M., Huder, L., Hulot, G., Jager, T., Kloss, C., Korte, M., Kuang, W., Kuvshinov, A., Langlais, B., Léger, J. M., Lesur, V., Livermore, P. W., Lowes, F. J., Macmillan, S., Magnes, W., Mandea, M., Marsal, S., Matzka, J., Metman, M. C., Minami, T., Morschhauser, A., Mound, J. E., Nair, M., Nakano, S., Olsen, N., Pavón-Carrasco, F. J., Petrov, V. G., Ropp, G., Rother, M., Sabaka, T. J., Sanchez, S., Saturnino, D., Schnepf, N. R., Shen, X., Stolle, C., Tangborn, A., Tøffner-Clausen, L., Toh, H., Torta, J. M., Varner, J., Vervelidou, F., Vigneron, P., Wardinski, I., Wicht, J., Woods, A., Yang, Y., Zeren, Z., and Zhou, B. (2021). International Geomagnetic Reference Field: the thirteenth generation. *Earth, Planets and Space*, 73(1).

Árkai, P. (2002). Phyllosilicates in very low-grade metamorphism: Transformation to micas. *Reviews in Mineralogy and Geochemistry*, 46(January):463–478.

Bai, L., Zhu, R., Wu, H., Guo, B., and Lü, J. (1998). New Cambrian paleomagnetic pole for Yangtze Block. *Science in China, Series D: Earth Sciences*, 41:70–71.

Basu, A. and Molinaroli, E. (1989). Provenance characteristics of detrital opaque Fe-Ti oxide minerals. *Journal of Sedimentary Petrology*, 59(6):922–934.

Blaauw, M. and Christeny, J. A. (2011). Flexible paleoclimate age-depth models using an autoregressive gamma process. *Bayesian Analysis*, 6(3):457–474.

Blodgett, R. H., Crabaugh, J. P., and McBride, E. F. (1993). The color of red beds - a geologic perspective. *Soil color. Proc. symposium, San Antonio, 1990*, (31):127–159.

Busch, B., Hilgers, C., Gronen, L., and Adelmann, D. (2017). Cementation and structural diagenesis of fluvio-aeolian Rotliegend sandstones, northern England. *Journal of the Geological Society*, 174(5):855–868.

Butler, R. F. (1992). *Paleomagnetism: Magnetic domains to geologic terranes*. Blackwell, Boston.

Cawood, P. A., Wang, W., Zhao, T., Xu, Y., Mulder, J. A., Pisarevsky, S. A., Zhang, L., Gan, C., He, H., Liu, H., Qi, L., Wang, Y., Yao, J., Zhao, G., Zhou, M. F., and Zi, J. W. (2020). Deconstructing South China and consequences for reconstructing Nuna and Rodinia. *Earth-Science Reviews*, 204:103169.

Cawood, P. A., Wang, Y., Xu, Y., and Zhao, G. (2013). Locating South China in Rodinia and Gondwana: A fragment of greater India lithosphere? *Geology*, 41(8):903–906.

Cawood, P. A., Zhao, G., Yao, J., Wang, W., Xu, Y., and Wang, Y. (2018). Reconstructing South China in Phanerozoic and Precambrian supercontinents. *Earth-Science Reviews*, 186:173–194.

Chang, L., Zhang, S., Li, H., Xian, H., Wu, H., and Yang, T. (2022). New paleomagnetic insights into the Neoproterozoic connection between South China and India and their position in Rodinia. *Geophysical Research Letters*, 49(10).

Charvet, J. (2013). The Neoproterozoic-Early Paleozoic tectonic evolution of the South China Block: An overview. *Journal of Asian Earth Sciences*, 74:198–209.

Chen, X., Fan, J. X., Chen, Q., Tang, L., and Hou, X. D. (2014). Toward a stepwise Kwangsian Orogeny. *Science China Earth Sciences*, 57(3):379–387.

Chen, Y., Meng, J., Liu, H., Wang, C., Tang, M., Liu, T., and Zhao, Y. (2022). Detrital zircons record the evolution of the Cathaysian Coastal Mountains along the South China margin. *Basin Research*, 34(2):688–701.

Cohen, K., Finney, S., Gibbard, P., and Fan, J.-X. (2022). The ICS International Chronostratigraphic Chart 2022/10. *Episodes*, 36(3):199–204.

Collinson, D. W. (1974). The role of pigment and specularite in the remanent magnetism of red sandstones. *Geophysical Journal of the Royal Astronomical Society*, 38(2):253–264.

Condon, D. J., Schoene, B., McLean, N. M., Bowring, S. A., and Parrish, R. R. (2015). Metrology and traceability of U-Pb isotope dilution geochronology (EARTHTIME Tracer Calibration Part I). *Geochimica et Cosmochimica Acta*, 164:464–480.

Cornell, R. M. and Schwertmann, U. (2003). *The Iron Oxides*. Wiley.

Dekkers, M. J. and Linssen, J. H. (1989). Rockmagnetic properties of fine-grained natural low-temperature haematite with reference to remanence acquisition mechanisms in red beds. *Geophysical Journal International*, 99(1):1–18.

Dinarès-Turell, J. and McClelland, E. (1991). A cautionary tale for palaeomagnetists: A spurious apparent single component remanence due to overlap of blocking-temperature spectra of two components. *Geophysical Research Letters*, 18(7):1297–1300.

Domeier, M. (2018). Early Paleozoic tectonics of Asia: Towards a full-plate model. *Geoscience Frontiers*, 9(3):789–862.

Driscoll, P. E. (2016). Simulating 2 Ga of geodynamo history. *Geophysical Research Letters*, 43(11):5680–5687.

Dunlop, D. J. (1974). Thermal enhancement of magnetic susceptibility. *Journal of Geophysics*, 40(1):439–451.

Dunlop, D. J. (1979). On the use of Zijderveld vector diagrams in multicomponent paleomagnetic studies. *Physics of the Earth and Planetary Interiors*, 20(1):12–24.

Edward, O., Paul, A. N., Bucher, H., Vérard, C., Adatte, T., Sonke, J. E., Schaltegger, U., and Vennemann, T. (2023). Timing and Provenance of Volcanic Fluxes Around the Permian-Triassic Boundary Mass Extinction in South China: U-Pb Zircon Geochronology, Volcanic Ash Geochemistry and Mercury Isotopes. *Geochemistry, Geophysics, Geosystems*, 24(6).

Egli, R. (2004). Characterization of individual rock magnetic components by analysis of remanence curves, 1. Unmixing natural sediments. *Studia Geophysica et Geodaetica*, 48(2):391–446.

Elmore, R. D., Muxworthy, A. R., and Aldana, M. (2012). Remagnetization and chemical alteration of sedimentary rocks. *Geological Society Special Publication*, 371(1):1–21.

Enkin, R. J. and Watson, G. S. (1996). Statistical analysis of palaeomagnetic inclination data. *Geophysical Journal International*, 126(2):495–504.

Evans, D. A. (2002). True polar wander and supercontinents. *Tectonophysics*, 362:303–320.

Evans, D. A. (2021). Meso-Neoproterozoic Rodinia supercycle. *Ancient Supercontinents and the Paleogeography of Earth*, pages 549–576.

Evans, D. A., Li, Z. X., and Murphy, J. B. (2016). Four-dimensional context of Earth's supercontinents. In Li, Z. X., Evans, D. A. D., and Murphy, J. B., editors, *Supercontinent Cycles Through Earth History*, volume 424, pages 1–14. The Geological Society of London.

Eyster, A., Weiss, B. P., Karlstrom, K., and Macdonald, F. A. (2020). Paleomagnetism of the Chuar Group and evaluation of the late Tonian Laurentian apparent polar wander path with implications for the makeup and breakup of Rodinia. *Bulletin of the Geological Society of America*, 132(3-4):710–738.

Fang, W., Voo, R. V. D., and Liang, Q. (1990). Ordovician Paleomagnetism of Eastern Yunnan, China. *Geophysical Research Letters*, 17(7):953–956.

Fisher, R. (1953). Dispersion on a sphere. *Proceedings of the Royal Society*, 217:295–305.

Flinn, D. (1962). On folding during three-dimensional progressive deformation. *Quarterly Journal of the Geological Society*, 118(1-4):385–428.

Fu, H., Zhang, S., Condon, D. J., and Xian, H. (2022). Secular change of true polar wander over the past billion years. *Science Advances*, 8(41):eabo2753.

Gao, L., Yang, Z., Han, Z., Tong, Y., Jing, X., and Zhang, S. H. (2018). Remagnetization of the Lower Ordovician Hongshiya Formation of the southwestern Yangtze Block. *Tectonophysics*, 738-739:83–91.

Gerstenberger, H. and Haase, G. (1997). A highly effective emitter substance for mass spectrometric Pb isotope ratio determinations. *Chemical Geology*, 136(3-4):309–312.

Gilder, S. A. and Courtillot, V. (1997). Timing of the North-South China collision from new middle to late Mesozoic paleomagnetic data from the North China Block. *Journal of Geophysical Research: Solid Earth*, 102(B8):17713–17727.

Gilder, S. A., Leloup, P. H., Courtillot, V., Chen, Y., Coe, R. S., Zhao, X., Xiao, W., Halim, N., Cogné, J.-P., and Zhu, R. (1999). Tectonic evolution of the Tancheng-Lujiang (Tan-Lu) fault via Middle Triassic to Early Cenozoic paleomagnetic data. *Journal of Geophysical Research: Solid Earth*, 104(B7):15365–15390.

Gilder, S. A., Tan, X., Bucher, H., Kuang, G., and Yin, J. (2008). Optimization of apparent polar wander paths: An example from the South China plate. *Physics of the Earth and Planetary Interiors*, 169(1-4):166–177.

Gong, Z., Dekkers, M. J., Heslop, D., and Mullender, T. A. (2009). End-member modelling of isothermal remanent magnetization (IRM) acquisition curves: A novel approach to diagnose remagnetization. *Geophysical Journal International*, 178(2):693–701.

Gubbins, D. and Herrero-Bervera, E., editors (2007). *Encyclopedia of Geomagnetism and Paleomagnetism*. Springer Netherlands, Dordrecht.

Haldar, S. and Tišljar, J. (2020). *Introduction to Mineralogy and Petrology*. Elsevier.

Halim, N., Cogné, J. P., Courtillot, V., and Chen, Y. (1996). Apparent synfolding magnetization as a result of overlap of pre- and post-folding magnetizations. *Geophysical Research Letters*, 23(24):3523–3526.

Halls, H. C. (1978). The use of converging remagnetization circles in palaeomagnetism. *Physics of the Earth and Planetary Interiors*, 16(1):1–11.

Halverson, G. P., Shen, C., Davies, J. H., and Wu, L. (2022). A Bayesian approach to inferring depositional ages applied to a late Tonian reference section in Svalbard. *Frontiers in Earth Science*, 10.

Han, Z., Yang, Z., Tong, Y., and Jing, X. (2015). New paleomagnetic results from Late Ordovician rocks of the Yangtze Block, South China, and their paleogeographic implications. *Journal of Geophysical Research: Solid Earth*, 120(7):4759–4772.

Heslop, D. and Dillon, M. (2007). Unmixing magnetic remanence curves without a priori knowledge. *Geophysical Journal International*, 170(2):556–566.

Hoffman, K. A. and Day, R. (1978). Separation of multi-component NRM: A general method. *Earth and Planetary Science Letters*, 40(3):433–438.

Hoffman, P. F., Kaufman, A. J., Halverson, G. P., and Schrag, D. P. (1998). A Neoproterozoic Snowball Earth. *Science*, 281(5381):1342–1346.

Hounslow, M. W., Domeier, M., and Biggin, A. J. (2018). Subduction flux modulates the geomagnetic polarity reversal rate. *Tectonophysics*, 742-743:34–49.

Huang, B., Yan, Y., Piper, J. D., Zhang, D., Yi, Z., Yu, S., and Zhou, T. (2018). Paleomagnetic constraints on the paleogeography of the East Asian blocks during Late Paleozoic and Early Mesozoic times. *Earth-Science Reviews*, 186(5):8–36.

Huang, K., Opdyke, N. D., and Zhu, R. (2000). Further paleomagnetic results from the Silurian of the Yangtze Block and their implications. *Earth and Planetary Science Letters*, 175(3-4):191–202.

Huang, W., Jackson, M. J., Dekkers, M. J., Solheid, P., Zhang, Y., Li, S., Guo, Z., and Ding, L. (2020). Remagnetization of Red Beds on the Tibetan Plateau: Mechanism and Diagnosis. *Journal of Geophysical Research: Solid Earth*, 125(8).

Jiang, X. S., Wang, J., Cui, X. Z., Zhuo, J. W., Xiong, G. Q., Lu, J. Z., and Liu, J. H. (2012). Zircon SHRIMP U-Pb geochronology of the Neoproterozoic Chengjiang Formation in central Yunnan Province (SW China) and its geological significance. *Science China Earth Sciences*, 55(11):1815–1826.

Jiao, W. J., Li, Y. X., and Yang, Z. Y. (2018). Paleomagnetism of a well-dated marine succession in South China: A possible Late Cambrian true polar wander (TPW). *Physics of the Earth and Planetary Interiors*, 277(June):38–54.

Jing, X., Evans, D. A., Yang, Z., Tong, Y., Xu, Y., and Wang, H. (2021). Inverted South China: A novel configuration for Rodinia and its breakup. *Geology*, 49(4):463–467.

Jing, X., Yang, Z., Evans, D. A., Tong, Y., Xu, Y., and Wang, H. (2020). A pan-latitudinal Rodinia in the Tonian true polar wander frame. *Earth and Planetary Science Letters*, 530:115880.

Jing, X., Yang, Z., Mitchell, R. N., Tong, Y., Zhu, M., and Wan, B. (2022). Ordovician–Silurian true polar wander as a mechanism for severe glaciation and mass extinction. *Nature Communications*, 13(1):1–12.

Jonkers, A. R. T., Jackson, A., and Murray, A. (2003). Four centuries of geomagnetic data from historical records. *Reviews of Geophysics*, 41(2):1–11.

Katz, B., Elmore, R. D., Cogoini, M., Engel, M. H., and Ferry, S. (2000). Associations between burial diagenesis of smectite, chemical remagnetization, and magnetite authigenesis in the Vocontian trough, SE France. *Journal of Geophysical Research: Solid Earth*, 105(B1):851–868.

Katz, B., Elmore, R. D., Cogoini, M., and Ferry, S. (1998). Widespread chemical remagnetization: orogenic fluids or burial diagenesis of clays? *Geology*, 26(7):603–606.

Kent, D. V., Zeng, X., Zhang, W. Y., and Opdyke, N. D. (1987). Widespread late Mesozoic to recent remagnetization of Paleozoic and lower Triassic sedimentary rocks from South China. *Tectonophysics*, 139(1-2):133–143.

Kirschvink, J. L. (1980). The least-squares line and plane and the analysis of palaeomagnetic data. *Geophysical Journal of the Royal Astronomical Society*, 62(3):699–718.

Kirschvink, J. L. (1992). Late Proterozoic low-latitude global glaciation: the snowball Earth. *The Proterozoic Biosphere*, 52:51–52.

Kirschvink, J. L., Ripperdan, R. L., and Evans, D. A. (1997). Evidence for a large-scale reorganization of Early Cambrian continental masses by inertial interchange true polar wander. *Science*, 277(5325):541–545.

Kletetschka, G. and Wasilewski, P. J. (2002). Grain size limit for SD hematite. *Physics of the Earth and Planetary Interiors*, 129(1-2):173–179.

Kodama, K. P. (2012). *Paleomagnetism of Sedimentary Rocks: Process and Interpretation*. John Wiley and Sons.

Kodama, K. P. (2013). Grand challenges in geomagnetism and paleomagnetism. *Frontiers in Earth Science*, 1:1–3.

Lan, Z., Li, X. H., Sano, Y., Takahata, N., Kagoshima, T., Zhang, S., Zhang, G., Liao, X., Tang, X., Gu, L., and Mao, Q. (2019). Two kinds of authigenic xenotime overgrowths in response to an Early Paleozoic tectonothermal event in South China. *Journal of Asian Earth Sciences*, 172(April 2018):423–442.

Lan, Z., Li, X. H., Zhu, M., Zhang, Q., and Li, Q. L. (2015). Revisiting the Liantuo Formation in Yangtze Block, South China: SIMS U-Pb zircon age constraints and regional and global significance. *Precambrian Research*, 263:123–141.

Li, C., Wang, X., He, C., Wu, X., Kong, Z., and Li, X. (2017). China National Digital Geological Map (Public Version at 1:200000 Scale) Spatial Database. *Geology in China*, 46:1–14.

Li, D., Yang, Z., Liu, Y., Yang, K., Wu, D., and Cai, P. (2022a). Timing and provenance transition of the Neoproterozoic Wuling Unconformity and Xihuangshan Unconformity of the Yangtze Block: Responses to peripheral orogenic Events. *Minerals*, 12(5):1–27.

Li, J., Dong, S., Zhang, Y., Zhao, G., Johnston, S. T., Cui, J., and Xin, Y. (2016). New insights into Phanerozoic tectonics of south China: Part 1, polyphase deformation in the Jiuling and Lianyunshan domains of the central Jiangnan Orogen. *Journal of Geophysical Research: Solid Earth*, 121(4):3048–3080.

Li, S., Cao, J., Feng, Z., Liu, X., Qin, Y., Hu, R., and Wang, C. (2022b). Neoproterozoic to Palaeozoic tectonic deformation history of the western Jiangnan Orogen, South China: Insights from new structural and geochronological data from northern Guangxi. *Geological Journal*, 57(1):292–316.

Li, Z. X., Bogdanova, S. V., Collins, A. S., Davidson, A., De Waele, B., Ernst, R. E., Fitzsimons, I. C., Fuck, R. A., Gladkochub, D. P., Jacobs, J., Karlstrom, K. E., Lu, S., Natapov, L. M., Pease, V., Pisarevsky, S. A., Thrane, K., and Vernikovsky, V. (2008). Assembly, configuration, and break-up history of Rodinia: A synthesis. *Precambrian Research*, 160(1-2):179–210.

Li, Z. X., Evans, D. A., and Halverson, G. P. (2013). Neoproterozoic glaciations in a revised global palaeogeography from the breakup of Rodinia to the assembly of Gondwanaland. *Sedimentary Geology*, 294:219–232.

Li, Z. X., Evans, D. A., and Zhang, S. (2004). A 90° spin on Rodinia: Possible causal links between the Neoproterozoic supercontinent, superplume, true polar wander and low-latitude glaciation. *Earth and Planetary Science Letters*, 220(3-4):409–421.

Li, Z. X., Li, X. H., Wartho, J. A., Clark, C., Li, W. X., Zhang, C. L., and Bao, C. (2010). Magmatic and metamorphic events during the early Paleozoic Wuyi-Yunkai orogeny, southeastern South China: New age constraints and pressure-temperature conditions. *Bulletin of the Geological Society of America*, 122(5-6):772–793.

Løvlie, R., Torsvik, T., Jelenska, M., and Levandowski, M. (1984). Evidence for detrital remanent magnetization carried by hematite in Devonian red beds from Spitsbergen; palaeomagnetic implications. *Geophysical Journal of the Royal Astronomical Society*, 79(2):573–588.

Macouin, M., Ader, M., Moreau, M. G., Poitou, C., Yang, Z., and Sun, Z. (2012). Deciphering the impact of diagenesis overprint on negative δ 13 C excursions using rock magnetism: Case study of Ediacaran carbonates, Yangjiaping section, South China. *Earth and Planetary Science Letters*, 351-352:281–294.

Macouin, M., Besse, J., Ader, M., Gilder, S. A., Yang, Z., Sun, Z., and Agrinier, P. (2004). Combined paleomagnetic and isotopic data from the Doushantuo carbonates,

South China: Implications for the "snowball Earth" hypothesis. *Earth and Planetary Science Letters*, 224(3-4):387–398.

Maloof, A. C., Halverson, G. P., Kirschvink, J. L., Schrag, D. P., Weiss, B. P., and Hoffman, P. F. (2006). Combined paleomagnetic, isotopic, and stratigraphic evidence for true polar wander from the Neoproterozoic Akademikerbreen Group, Svalbard, Norway. *Bulletin of the Geological Society of America*, 118(9-10):1099–1124.

Marshall, C. R. (2006). Explaining the Cambrian "Explosion" of Animals. *Annual Review of Earth and Planetary Sciences*, 34:355–384.

Maxbauer, D. P., Feinberg, J. M., and Fox, D. L. (2016a). Magnetic mineral assemblages in soils and paleosols as the basis for paleoprecipitation proxies: A review of magnetic methods and challenges. *Earth-Science Reviews*, 155:28–48.

Maxbauer, D. P., Feinberg, J. M., and Fox, D. L. (2016b). MAX UnMix: A web application for unmixing magnetic coercivity distributions. *Computers and Geosciences*, 95:140–145.

McBride, E. F. (1989). Quartz cement in sandstones: a review. *Earth-Science Reviews*, 26(1-3):69–112.

McElhinny, M. W. (1964). Statistical significance of the fold test in paleomagnetism. *Geophysical Journal of the Royal Astronomical Society*, 8:338–340.

McEnroe, S. A. and Brown, L. L. (2000). A closer look at remanence-dominated aeromagnetic anomalies: Rock magnetic properties and magnetic mineralogy of the Russell Belt microcline-sillimanite gneiss, northwest Adirondack Mountains, New York. *Journal of Geophysical Research: Solid Earth*, 105(B7):16437–16456.

McFadden, P. L. and McElhinny, M. W. (1990). Classification of the reversal test in palaeomagnetism. *Geophysical Journal International*, 103(3):725–729.

McLean, N. M., Condon, D. J., Schoene, B., and Bowring, S. A. (2015). Evaluating uncertainties in the calibration of isotopic reference materials and multi-element isotopic tracers (EARTHTIME Tracer Calibration Part II). *Geochimica et Cosmochimica Acta*, 164:481–501.

Meert, J. G., Levashova, N. M., Bazhenov, M. L., and Landing, E. (2016). Rapid changes of magnetic Field polarity in the late Ediacaran: Linking the Cambrian evolutionary radiation and increased UV-B radiation. *Gondwana Research*, 34:149–157.

Meert, J. G., Pivarunas, A. F., Evans, D. A., Pisarevsky, S. A., Pesonen, L. J., Li, Z. X., Elming, S. Å., Miller, S. R., Zhang, S., and Salminen, J. M. (2020). The magnificent seven: A proposal for modest revision of the Van der Voo (1990) quality index. *Tectonophysics*, 790:228549.

Meng, J., Coe, R. S., Wang, C., Gilder, S. A., Zhao, X., Liu, H., Li, Y., Ma, P., Shi, K., and Li, S. (2017). Reduced convergence within the Tibetan Plateau by 26 Ma? *Geophysical Research Letters*, 44(13):6624–6632.

Meng, J., Gilder, S. A., Li, Y., Chen, Y., Zhang, C., Zhou, Z., Liu, T., Zhao, Y., Wang, Z., and Wang, C. (2022). Remagnetization age and mechanism of Cretaceous sediments in relation to dyke intrusion, Hainan Island: Tectonic implications for South China and the Red River Fault. *Journal of Geophysical Research: Solid Earth*, 127(1):1–19.

Merrill, R. T. and McElhinny, M. W. (1983). *The Earth's Magnetic Field: Its History, Origin and Planetary Perspective*. Academic Press, London.

Morris, S. C. (1985). The Ediacaran biota and early metazoan evolution. *Geological Magazine*, 122(1):77–81.

Mukherjee, I., Large, R. R., Corkrey, R., and Danyushevsky, L. V. (2018). The Boring Billion, a slingshot for Complex Life on Earth. *Scientific Reports*, 8(1):1–7.

Néel, L. (1949). Influence des fluctuations thermiques sur l'aimantation de grains ferromagnétiques très fins. *Comptes Rendus Hebdomadaires Des Seances De L Academie Des Sciences*, 228(8):664–666.

Niu, J., Li, Z. X., and Zhu, W. (2016). Palaeomagnetism and geochronology of mid-Neoproterozoic Yanbian dykes, South China: Implications for a c. 820-800 Ma true polar wander event and the reconstruction of Rodinia. *Geological Society Special Publication*, 424(1):192–211.

Ogg, J. G. (2012). Geomagnetic Polarity Time Scale. *The Geologic Time Scale 2012*, 1-2:85–113.

Oliver, J. (1986). Fluids expelled tectonically from orogenic belts: their role in hydrocarbon migration and other geologic phenomena. *Geology*, 14(2):99–102.

Opdyke, N. D. and DiVenere, V. J. (2004). The magnetic polarity stratigraphy of the Mauch Chunk Formation, Pennsylvania. *Proceedings of the National Academy of Sciences*, 101(37):13423–13427.

Opdyke, N. D., Huang, K., Xu, G., Zhang, W., and Kent, D. (1987). Paleomagnetic results from the Silurian of the Yangtze paraplatform. *Tectonophysics*, 139(1-2):123–132.

O'Reilly, W. (1984). Magnetic properties of other mineral systems. In *Rock and Mineral Magnetism*, pages 172–193. Springer US, Boston.

Özdemir, Ö. and Dunlop, D. J. (2002). Thermoremanence and stable memory of single-domain hematites. *Geophysical Research Letters*, 29(18):10–13.

Özdemir, Ö. and Dunlop, D. J. (2005). Thermoremanent magnetization of multidomain hematite. *Journal of Geophysical Research*, 110(B09104):1–8.

Özdemir, Ö. and Dunlop, D. J. (2014). Hysteresis and coercivity of hematite. *Journal of Geophysical Research: Solid Earth*, 119(4):2582–2594.

Özdemir, Ö., Dunlop, D. J., and Berquó, T. S. (2008). Morin transition in hematite: Size dependence and thermal hysteresis. *Geochemistry, Geophysics, Geosystems*, 9(10).

Park, Y., Swanson-Hysell, N. L., Xian, H., Zhang, S., Condon, D. J., Fu, H., and Macdonald, F. A. (2021). A Consistently High-Latitude South China From 820 to 780 Ma: Implications for Exclusion From Rodinia and the Feasibility of Large-Scale True Polar Wander. *Journal of Geophysical Research: Solid Earth*, 126(6):1–29.

Parry, W. T., Chan, M. A., and Beitler, B. (2004). Chemical bleaching indicates episodes of fluid flow in deformation bands in sandstone. *American Association of Petroleum Geologists Bulletin*, 88(2):175–191.

Pochon, A., Beaudoin, G., Branquet, Y., Boulvais, P., Gloaguen, E., and Gapais, D. (2017). Metal mobility during hydrothermal breakdown of Fe-Ti oxides: Insights from Sb-Au mineralizing event (Variscan Armorican Massif, France). *Ore Geology Reviews*, 91:66–99.

Posth, N. R., Köhler, I., D. Swanner, E., Schröder, C., Wellmann, E., Binder, B., Konhauser, K. O., Neumann, U., Berthold, C., Nowak, M., and Kappler, A. (2013). Simulating Precambrian banded iron formation diagenesis. *Chemical Geology*, 362:66–73.

Ratner, B. (2009). The correlation coefficient: Its values range between +1/-1, or do they? *Journal of Targeting, Measurement and Analysis for Marketing*, 17(2):139–142.

Raub, T. D., Kirschvink, J. L., and Evans, D. A. (2015). True Polar Wander: Linking Deep and Shallow Geodynamics to Hydro- and Biospheric Hypotheses. *Treatise on Geophysics: Second Edition*, 5(1969):511–530.

Roberts, A. P. (2015). Magnetic mineral diagenesis. *Earth-Science Reviews*, 151:1–47.

Roberts, A. P., Cui, Y., and Verosub, K. L. (1995). Wasp-waisted hysteresis loops: Mineral magnetic characteristics and discrimination of components in mixed magnetic systems. *Journal of Geophysical Research*, 100(B9):17909–17924.

Roberts, N. M. (2013). The boring billion? - Lid tectonics, continental growth and environmental change associated with the Columbia supercontinent. *Geoscience Frontiers*, 4(6):681–691.

Rochette, P., Mathé, P. E., Esteban, L., Rakoto, H., Bouchez, J. L., Liu, Q., and Torrent, J. (2005). Non-saturation of the defect moment of goethite and fine-grained hematite up to 57 Teslas. *Geophysical Research Letters*, 32(22):1–4.

Saint-Bezar, B., Hebert, R. L., Aubourg, C., Robion, P., Swennen, R., and Frizon De Lamotte, D. (2002). Magnetic fabric and petrographic investigation of hematite-bearing sandstones within ramp-related folds: Examples from the South Atlas Front (Morocco). *Journal of Structural Geology*, 24(9):1507–1520.

Schaltegger, U., Ovtcharova, M., Gaynor, S. P., Schoene, B., Wotzlaw, J. F., Davies, J. F., Farina, F., Greber, N. D., Szymanowski, D., and Chelle-Michou, C. (2021). Long-term repeatability and interlaboratory reproducibility of high-precision ID-TIMS U-Pb geochronology. *Journal of Analytical Atomic Spectrometry*, 36(7):1466–1477.

Schaltegger, U., Schmitt, A. K., and Horstwood, A. (2015). U-Th-Pb zircon geochronology by ID-TIMS, SIMS, and laser. *Chemical Geology*, 402(8):89–110.

Schmitz, B., Bergström, S. M., and Xiaofeng, W. (2010). The middle Darriwilian (Ordovician) δ13C excursion (MDICE) discovered in the Yangtze Platform succession in China: Implications of its first recorded occurrences outside Baltoscandia. *Journal of the Geological Society*, 167(2):249–259.

Schoene, B., Crowley, J. L., Condon, D. J., Schmitz, M. D., and Bowring, S. A. (2006). Reassessing the uranium decay constants for geochronology using ID-TIMS U-Pb data. *Geochimica et Cosmochimica Acta*, 70(2):426–445.

Sierra-Rojas, M. I. and Molina-Garza, R. S. (2018). Detrital and early chemical remanent magnetization in redbeds and their rock magnetic signature: Zicapa Formation, southern Mexico. *Geophysical Journal International*, 213(3):1701–1719.

Song, G., Wang, X., Shi, X., and Jiang, G. (2017). New U-Pb age constraints on the upper Banxi Group and synchrony of the Sturtian glaciation in South China. *Geoscience Frontiers*, 8(5):1161–1173.

Sun, H.-Q., Huang, J.-Z., Guo, L.-Q., and Chen, J. (2012). Subdivision and isotopic age of Lengjiaxi Group in Hunan Province. *Geology and Mineral Resources of South China*, 28(1):20–26.

Swanson-Hysell, N. L., Fairchild, L. M., and Slotznick, S. P. (2019). Primary and Secondary Red Bed Magnetization Constrained by Fluvial Intraclasts. *Journal of Geophysical Research: Solid Earth*, 124(5):4276–4289.

Swanson-Hysell, N. L., Maloof, A. C., Kirschvink, J. L., Evans, D. A., Halverson, G. P., and Hurtgen, M. T. (2012). Constraints on neoproterozoic paleogeography and paleozoic orogenesis from paleomagnetic records of the bitter springs formation, amadeus basin, central Australia. *American Journal of Science*, 312(8):817–884.

Tan, X., Kodama, K. P., Gilder, S. A., Courtillot, V., and Cogné, J. P. (2007). Palaeomagnetic evidence and tectonic origin of clockwise rotations in the Yangtze fold belt, South China Block. *Geophysical Journal International*, 168(1):48–58.

Tarantola, A. (2004). *Inverse Problem Theory and Methods for Model Parameter Estimation*. SIAM: Society for Industrial and Applied Mathematics, 1st edition.

Tauxe, L. (1993). Sedimentary records of relative paleointensity of the geomagnetic field: Theory and practice. *Reviews of Geophysics*, 31(3):319.

Tauxe, L. and Kent, D. V. (2004). A simplified statistical model for the geomagnetic field and the detection of shallow bias in paleomagnetic inclinations: Was the ancient magnetic field dipolar? *Geophysical Monograph Series*, 145:101–115.

Tauxe, L., Kent, D. V., and Opdyke, N. D. (1980). Magnetic components contributing to the NRM of Middle Siwalik red beds. *Earth and Planetary Science Letters*, 47(2):279–284.

Ting, V. K. (1929). The Orogenic Movements in China. *Bulletin of the Geological Society of China*, 8(2):151–170.

Tonti-Filippini, J. A. D. and Gilder, S. A. (2023). Vector unmixing of multicomponent palaeomagnetic data. *Geophysical Journal International*, 233(3):1632–1654.

Tonti-Filippini, J. A. D., Robert, B., Muller, É., Wack, M., Zhao, X., and Gilder, S. A. (2021). The Neoproterozoic geomagnetic field: New insights from a high-resolution paleomagnetic study in South China. In *EGU General Assembly 2021*.

Torsvik, T. H. (2003). The Rodinia jigsaw puzzle. *Science*, 300(5624):1379–1381.

Torsvik, T. H., Domeier, M., and Cocks, L. R. M. (2021). Phanerozoic paleogeography and Pangea. In *Ancient Supercontinents and the Paleogeography of Earth*, chapter 18, pages 577–603. Elsevier.

Torsvik, T. H., Van der Voo, R., Preeden, U., Mac Niocaill, C., Steinberger, B., Doubrovine, P. V., van Hinsbergen, D. J., Domeier, M., Gaina, C., Tohver, E., Meert, J. G., McCausland, P. J., and Cocks, L. R. M. (2012). Phanerozoic Polar Wander, Palaeogeography and Dynamics. *Earth-Science Reviews*, 114(3-4):325–368.

Van der Voo, R. (1990). The reliability of paleomagnetic data. *Tectonophysics*, 184(1):1–9.

Van der Voo, R. and Torsvik, T. H. (2012). The history of remagnetization of sedimentary rocks: Deceptions, developments and discoveries. *Geological Society Special Publication*, 371(1):23–53.

Volk, M. W. R. (2016). *Influence of pressure, temperature and composition on magnetic recording in meteorites*. PhD thesis, LMU Munich.

Wack, M. R. (2023). Improved anisotropy of magnetic remanence results from vectorial readings using novel refinement method. *Geophysical Journal International*, 233(2):1113–1123.

Wack, M. R. and Gilder, S. A. (2012). The SushiBar: An automated system for paleomagnetic investigations. *Geochemistry, Geophysics, Geosystems*, 13(12):1–24.

Walker, T. R. (1976). Diagenetic origin of continental red beds. In *The Continental Permain in Central, West, and South Europe*, pages 240–282. Springer Netherlands.

Walker, T. R., Larson, E. E., and Hoblitt, R. P. (1981). Nature and origin of hematite in the Moenkopi Formation (Triassic), Colorado Plateau: A contribution to the origin of magnetism in red beds. *Journal of Geophysical Research*, 86(B1):317–333.

Walter, B. F., Gerdes, A., Kleinhanns, I. C., Dunkl, I., von Eynatten, H., Kreissl, S., and Markl, G. (2018). The connection between hydrothermal fluids, mineralization, tectonics and magmatism in a continental rift setting: Fluorite Sm-Nd and hematite and carbonates U-Pb geochronology from the Rhinegraben in SW Germany. *Geochimica et Cosmochimica Acta*, 240:11–42.

Wang, H., Yuan, L., Wang, L., Zhou, Z., and An, J. (2016a). Very Low-Grade Metamorphism of Clastic Rocks from the Meso-Neoproterozoic and the Paleozoic along the Profile Yueyang-Linxiang in Northeastern Hunan Province and Its Geological Implications. *Acta Geologica Sinica - English Edition*, 90(5):1743–1753.

Wang, H., Zhou, Z., Wang, L., and Yuan, L. (2014). Anchimetamorphism and diagenesis of the Meso-Neoproterozoic and the Lower Paleozoic along profile Yangjiaping in North Hunan Province, China. *Yanshi Xuebao/Acta Petrologica Sinica*, 30(10):3013–3020.

Wang, J., Li, X., Duan, T., Liu, D., Song, B., Li, Z., and Gao, Y. (2003). Zircon SHRIMP U-Pb dating for the Cangshuipu volcanic rocks and its implications for the lower boundary age of the Nanhua strata in South China. *Chinese Science Bulletin*, 48(16):1663–1669.

Wang, J. and Li, Z. X. (2003). History of neoproterozoic rift basins in South China: Implications for Rodinia break-up. *Precambrian Research*, 122(1-4):141–158.

Wang, J., Zhou, X., Deng, Q., Fu, X., Duan, T., and Guo, X. (2015). Sedimentary successions and the onset of the Neoproterozoic Jiangnan sub-basin in the Nanhua rift, South China. *International Journal of Earth Sciences*, 104(3):521–539.

Wang, W., Zhou, M. F., Zhao, J. H., Pandit, M. K., Zheng, J. P., and Liu, Z. R. (2016b). Neoproterozoic active continental margin in the southeastern Yangtze Block of South China: Evidence from the ca. 830–810 Ma sedimentary strata. *Sedimentary Geology*, 342:254–267.

Wang, Y., Fan, W., Zhao, G., Ji, S., and Peng, T. (2007). Zircon U-Pb geochronology of gneissic rocks in the Yunkai massif and its implications on the Caledonian event in the South China Block. *Gondwana Research*, 12(4):404–416.

Watson, G. S. and Enkin, R. J. (1993). The fold test in paleomagnetism as a parameter estimation problem. *Geophysical Research Letters*, 20(19):2135–2137.

Widmann, P., Davies, J. H., and Schaltegger, U. (2019). Calibrating chemical abrasion: Its effects on zircon crystal structure, chemical composition and U–Pb age. *Chemical Geology*, 511:1–10.

Xian, H., Zhang, S., Li, H., Yang, T., and Wu, H. (2020). Geochronological and palaeomagnetic investigation of the Madiyi Formation, lower Banxi Group, South China: Implications for Rodinia reconstruction. *Precambrian Research*, 336:105494.

Xie, S.-k., Wang, Z.-j., Wang, J., and Zhuo, J.-w. (2012). LA-ICP-MS zircon U-Pb dating of the bentonites from the uppermost part of the Ordovician Wufeng Formation in the Haoping section, Taoyuan, Hunan. *Sedimentary and Tethyan Geology*, 4:597.

Xu, X., Li, Y., Tang, S., Xue, D., and Zhang, Z. (2015). Neoproterozoic to Early Paleozoic polyorogenic deformation in the southeastern margin of the Yangtze Block: Constraints from structural analysis and 40Ar/39Ar geochronology. *Journal of Asian Earth Sciences*, 98:141–151.

Xu, Y. J., Cawood, P. A., and Du, Y. S. (2016). Intraplate orogenesis in response to Gondwana assembly: Kwangsian Orogeny, South China. *American Journal of Science*, 316(4):329–362.

Yan, D. P., Zhou, M. F., Song, H. L., Wang, X. W., and Malpas, J. (2003). Origin and tectonic significance of a Mesozoic multi-layer over-thrust system within Yangtze Block (South China). *Tectonophysics*, 361(3-4):239–254.

Yang, J., Luo, P., Ling, Y., Yang, S., Bai, D., Wei, F., Cao, S., and Peng, N. (2021). Superimposed features and deformation mechanism of Early Mesozoic folds in the Sangzhi-Shimen area, northern Hunan. *Bulletin of Geological Science and Technology*, 40(6):43–54.

Yang, S. X. and Blum, N. (1999). A fossil hydrothermal system or a source-bed in the Madiyi Formation near the Xiangxi Au-Sb-W deposit, NW Hunan, PR China? *Chemical Geology*, 155(1-2):151–169.

Yang, Z., Sun, Z., Yang, T., and Pei, J. (2004). A long connection (750-380 Ma) between South China and Australia: Paleomagnetic constraints. *Earth and Planetary Science Letters*, 220(3-4):423–434.

Yao, J., Cawood, P. A., Shu, L., and Zhao, G. (2019). Jiangnan Orogen, South China: A 970-820 Ma Rodinia margin accretionary belt. *Earth-Science Reviews*, 196.

Yin, C., Gao, L., Xing, Y., Wang, Z., and Tang, F. (2004). Advances in the study on the Nanhua System of the Neoproterozoic and its stratotype in South China (in Chinese

with English abstract). In *Professional Papers of Stratigraphy and Palaeontology*, pages 1–10. Geological Publishing House, Beijing.

Yin, C., Liu, D., Gao, L., Wang, Z., Xing, Y., Jian, P., and Shi, Y. (2003). Lower boundary age of the Nanhua System and the Gucheng glacial stage: Evidence from SHRIMP II dating. *Chinese Science Bulletin*, 48(16):1657–1662.

Zhang, H. (1998). Preliminary Proterozoic apparent polar wander paths for the South China Block and their tectonic implications. *Canadian Journal of Earth Sciences*, 35(3):302–320.

Zhang, Q. R. and Piper, J. D. (1997). Palaeomagnetic study of Neoproterozoic glacial rocks of the Yangzi Block: Palaeolatitude and configuration of South China in the late Proterozoic Supercontinent. *Precambrian Research*, 85(3-4):173–199.

Zhang, S., Chang, L., Zhao, H., Ding, J., Xian, H., Li, H., Wu, H., and Yang, T. (2021). The Precambrian drift history and paleogeography of the Chinese cratons. In *Ancient Supercontinents and the Paleogeography of Earth*, pages 333–376. Elsevier.

Zhang, S., Jiang, G. Q., Dong, J., Han, Y. G., and Wu, H. C. (2008). New SHRIMP U-Pb age from the Wuqiangxi Formation of Banxi Group: Implications for rifting and stratigraphic erosion associated with the early Cryogenian (Sturtian) glaciation in South China. *Science in China, Series D: Earth Sciences*, 51(11):1537–1544.

Zhang, S., Li, H., Jiang, G., Evans, D. A., Dong, J., Wu, H., Yang, T., Liu, P., and Xiao, Q. (2015a). New paleomagnetic results from the Ediacaran Doushantuo Formation in South China and their paleogeographic implications. *Precambrian Research*, 259:130–142.

Zhang, S., Li, H., Zhang, X., Wu, H., Yang, T., Liu, Y., and Cao, Q. (2012). New Ordovician paleomagnetic results from South China Block and their paleogeographic implications. *The 34th IGC abstract*.

Zhang, X., Wang, Y., and Chen, X. (2000). Diagenesis and Porosity of the Cambrian-Ordovician Carbonate Shoal Facies at Yangjiaping, Shimen, Hunan. *Acta Geologica Sinica - English Edition*, 74(1):29–45.

Zhang, Y., Wang, Y., Zhang, Y., and Zhang, A. (2015b). Neoproterozoic assembly of the Yangtze and Cathaysia blocks: Evidence from the Cangshuipu Group and associated rocks along the Central Jiangnan Orogen, South China. *Precambrian Research*, 269:18–30.

Zhao, G., Wang, Y., Huang, B., Dong, Y., Li, S., Zhang, G., and Yu, S. (2018). Geological reconstructions of the East Asian blocks: From the breakup of Rodinia to the assembly of Pangea. *Earth-Science Reviews*, 186(October):262–286.

Zheng, B., Zhou, R., Mou, C., Wang, X., Xiao, Z., and Chen, Y. (2020). Nature of the Late Ordovician-Early Silurian Xiaohe section, Hunan-Hubei area, South China: implications for the Kwangsian Orogeny. *International Geology Review*, 62(10):1262–1272.

Zijderveld, J. (1967). A.C. demagnetization of rocks: Analysis of results. In Runcorn, S., Creer, K., and Collinson, D., editors, *Methods in Palaeomagnetism*, pages 254–286. Elsevier, Amsterdam.